Soft Lithography

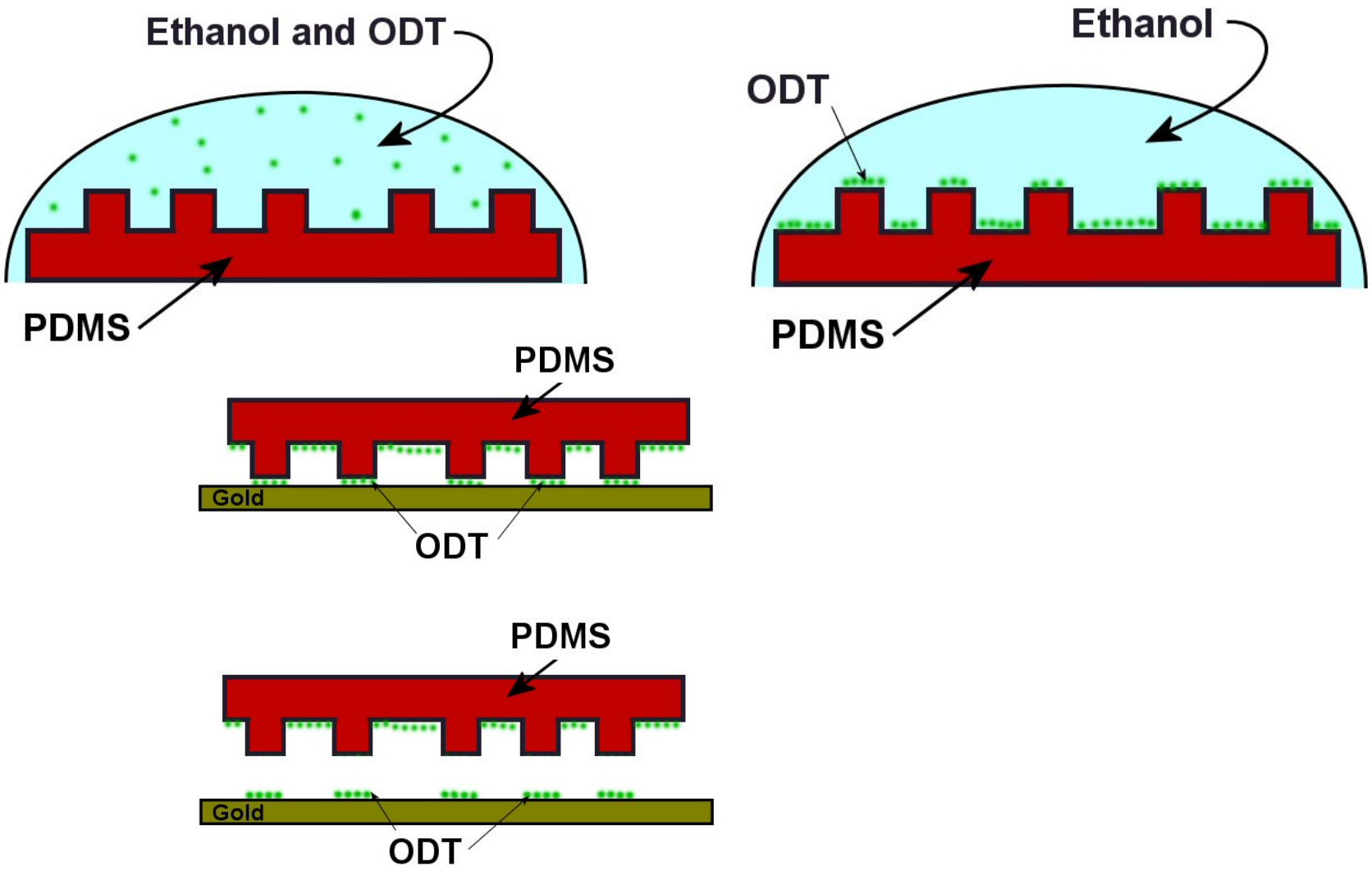

Table 1 Comparison between photolithography and soft lithography

	Photolithography	Soft lithography
Definition of patterns	Rigid photomask (patterned Cr supported on a quartz plate)	Elastomeric stamp or mold (a PDMS block patterned with relief features)
Materials that can be patterned directly	Photoresists (polymers with photo-sensitive additives)	Photoresists[a,e]
	SAMs on Au and SiO_2	SAMs on Au, Ag, Cu, GaAs, Al, Pd, and SiO_2[a] Unsensitized polymers[b–e] (epoxy, PU, PMMA, ABS, CA, PS, PE, PVC) Precursor polymers[c,d] (to carbons and ceramics) Polymer beads[d] Conducting polymers[d] Colloidal materials[a,d] Sol-gel materials[c,d] Organic and inorganic salts[d] Biological macromolecules[d]
Surfaces and structures that can be patterned	Planar surfaces 2-D structures	Both planar and nonplanar Both 2-D and 3-D structures
Current limits to resolution	~250 nm (projection) ~100 nm (laboratory)	~30 nm[a,b], ~60 nm[e], ~1 μm[d,e] (laboratory)
Minimum feature size	~100 nm (?)	10 (?) - 100 nm

[a–e]Made by (a) μCP, (b) REM, (c) μTM, (d) MIMIC, (e) SAMIM. PU:polyurethane; PMMA: poly(methyl methacrylate); ABS: poly(acrylonitrile-butadiene-styrene); CA: cellulose acetate; PS: polystyrene; PE: polyethylene; and PVC: poly(vinyl chloride)

Micro-contact Printing

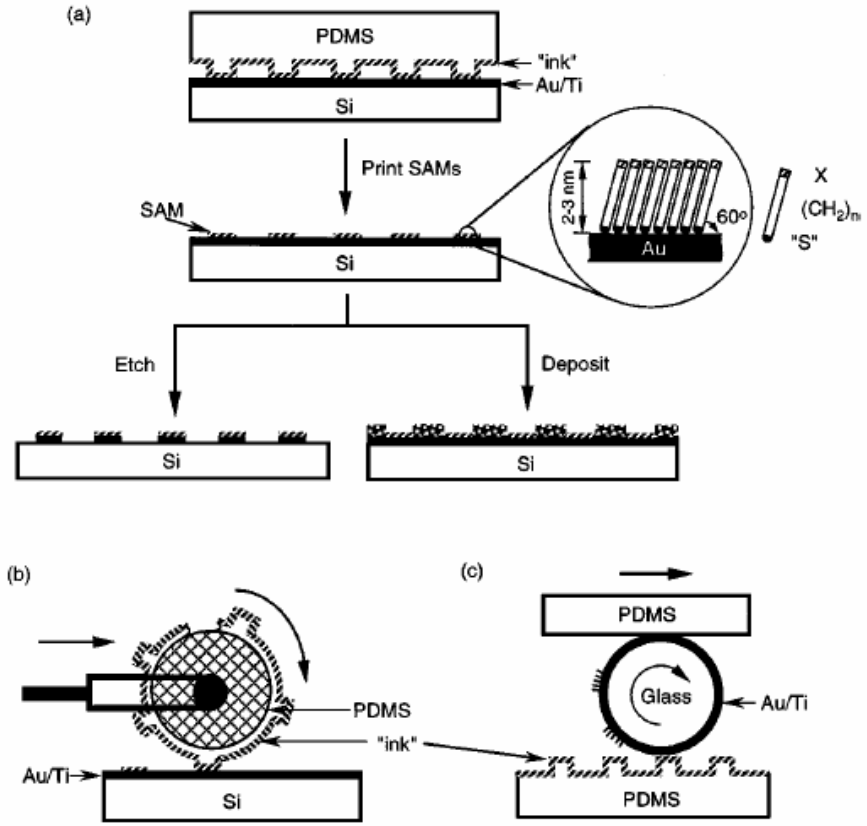

Figure 2 Schematic procedures for μCP of hexadecanethiol (HDT) on the surface of gold: (*a*) printing on a planar surface with a planar stamp (21), (*b*) printing on a planar surface over large areas with a rolling stamp (128), and (*c*) printing on a nonplanar surface with a planar stamp (174).

Micro-contact Printing

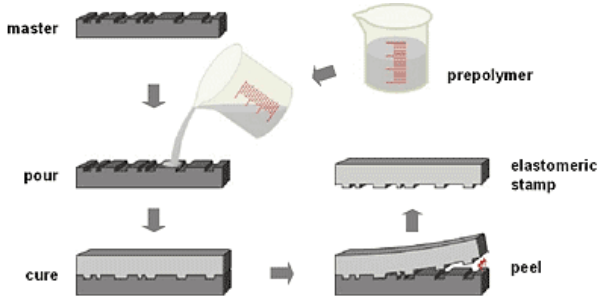

Fig.2 The stamp replication process: A master with a negative of the desired pattern is cast with a pre-polymer. After curing the polymer, the elastomeric stamp is peeled off the master and ready for microcontact printing.

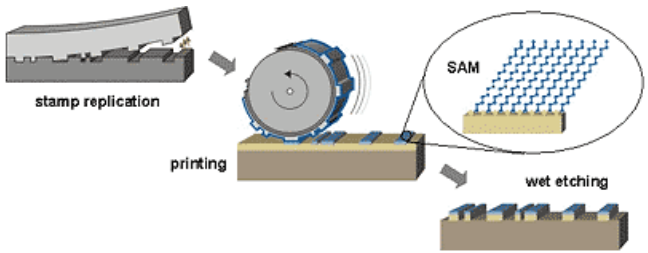

Fig.1 The microcontact printing (μCP) process: An elastomeric stamp is replicated from a master. After inking of the stamp with a suitable ink, it is fixated on a printing machine with help of which it is brought into conformal contact with a substrate. There the ink forms a self-assembled monolayer (SAM) which can be used as a resist in a subsequent wet etching step.

Micro-contact Printing

http://mrsec.wisc.edu/Edetc/nanolab/print/text.html

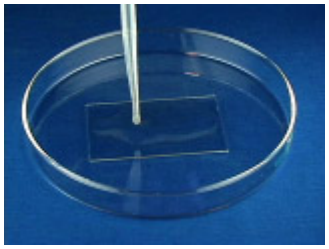

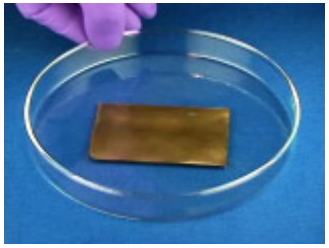

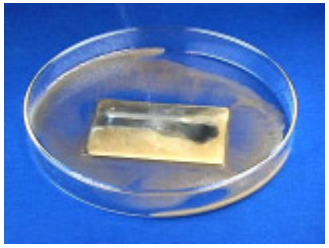

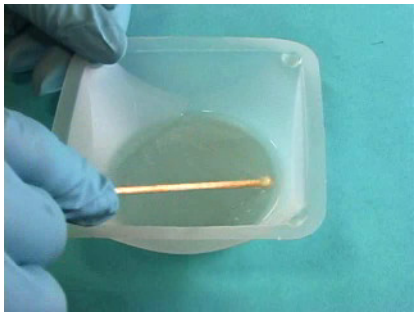

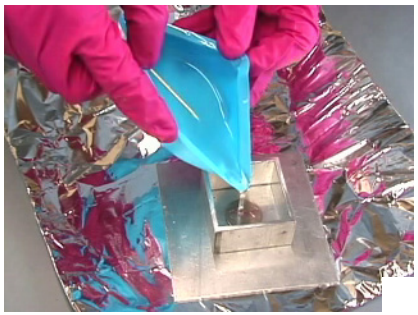

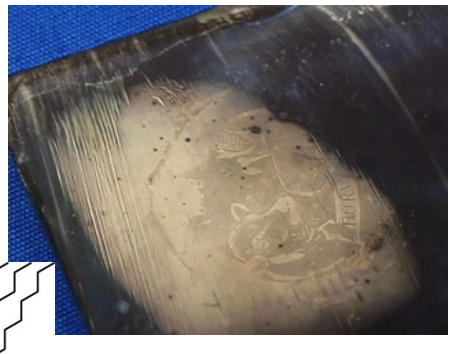

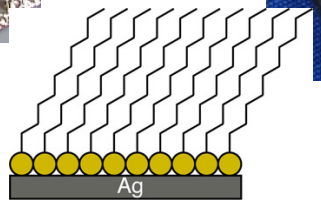

Micro-contact Printing

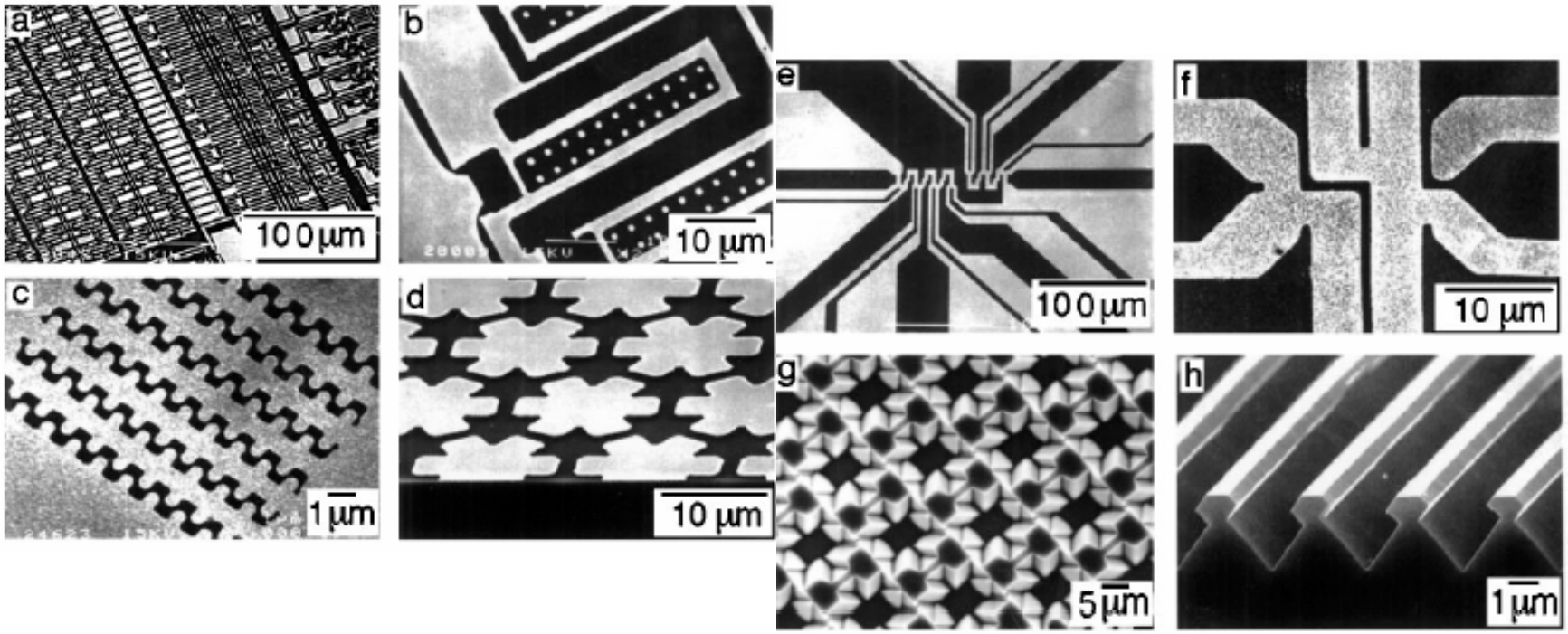

Self-Assemble Monolayer (SAM)

Chem. Rev. **2005**, *105*, 1103–1169

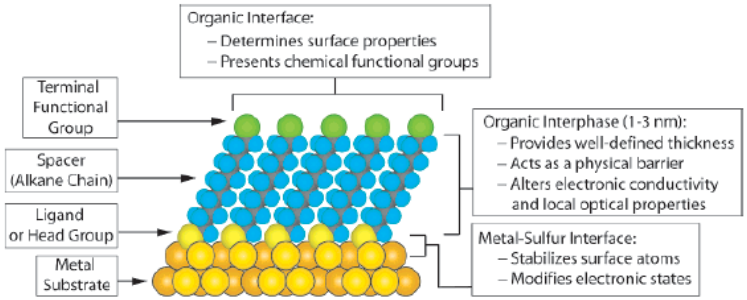

Ligand	Substrates	Morphology of Substrate: Thin Films or Bulk Material	Morphology of Substrate: Nanoparticles or Other Nanostructures
ROH	Fe_xO_y		35
	Si-H	36	
	Si	37	
RCOO-/RCOOH	α-Al_2O_3	38,39	
	Fe_xO_y		40
	Ni		41,42
	Ti/TiO_2	43	
RCOO–OOCR	Si(111):H	44	
	Si(100):H		
Ene-diol	Fe_2O_3		45
RNH_2	FeS_2	46	
	Mica	47	
	Stainless Steel 316L	48	
	$YBa_2Cu_3O_{7-\delta}$	49	
	CdSe		50
RC≡N	Ag	51	
	Au		
R-N≡N$^+$(BF_4^-)	GaAs(100)	52	
	Pd	52	
	Si(111):H	52	
RSH	Ag	26	53,54
	$Ag_{90}Ni_{10}$	55	
	AgS		56
	Au	26	57
	AuAg		58
	AuCu		58
	Au_xPd_{1-x}		58
	CdTe		59
	CdSe		60
	CdS		61,62
	Cu	26	58
	FePt		63-66
	GaAs	67	
	Ge	68	
	Hg	69-71	
	HgTe		72
	InP	73	
	Ir		74
	Ni	75	
	PbS		76-78
	Pd	30	74,79
	PdAg		58
	Pt	32	80
	Ru		81
	Stainless Steel 316L	48	
	$YBa_2Cu_3O_{7-\delta}$	82	
	Zn	83	
	ZnSe	84	
	ZnS		85
RSAc	Au	86	
R–S	Au		87
RSR'	Au	88	

Ligand	Substrates	Morphology of Substrate: Thin Films or Bulk Material	Morphology of Substrate: Nanoparticles or Other Nanostructures
RSSR'	Ag	89	90
	Au	20	90-92
	CdS		61
	Pd	30	
	Au	93	
RCSSH	Au	94	
	CdSe		95
$RS_2O_3^-Na^+$	Au	96	98
	Cu	97	
RSeH	Ag	99	
	Au	100,101	
	CdS		60
	CdSe		102
RSeSeR'	Au	101	
R_3P	Au		103
	FeS_2	46	
	CdS		104
	CdSe		104
	CdTe		104
$R_3P=O$	Co		105,106
	CdS		104
	CdSe		104
	CdTe		104
$RPO_3^{2-}/RP(O)(OH)_2$	Al	107	
	Al-OH	108	
	$Ca_{10}(PO_4,CO_3)_6(OH)_2$	109	
	GaAs	110	
	GaN	110	
	Indium tin oxide (ITO)	111	
	Mica	112	
	TiO_2	113,114	
	ZrO_2	114,115	
	CdSe		116-118
	CdTe		118,119
RPO_4^{2-}	Al_2O_3	120	
	Nb_2O_5	120	
	Ta_2O_3	121	
	TiO_2	120,122	
RN≡C	Pt	123	124
$RHC=CH_2$	Si	37	
RC≡CH	Si(111):H	125	
$RSiX_3$ X = H, Cl, OCH_2CH_3	HfO_2	126	
	ITO	127	
	PtO	128	
	TiO_2	113,126,129	
	ZrO_2	126,129	

S-Au 25-30 Kcal/mole
Si-O 190 kcal/mole

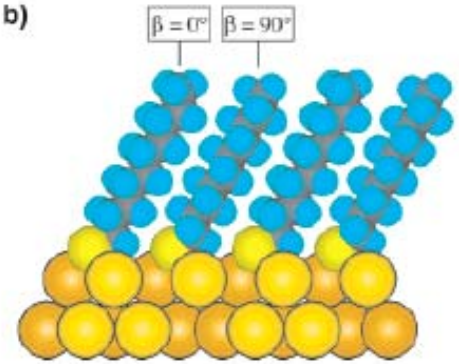

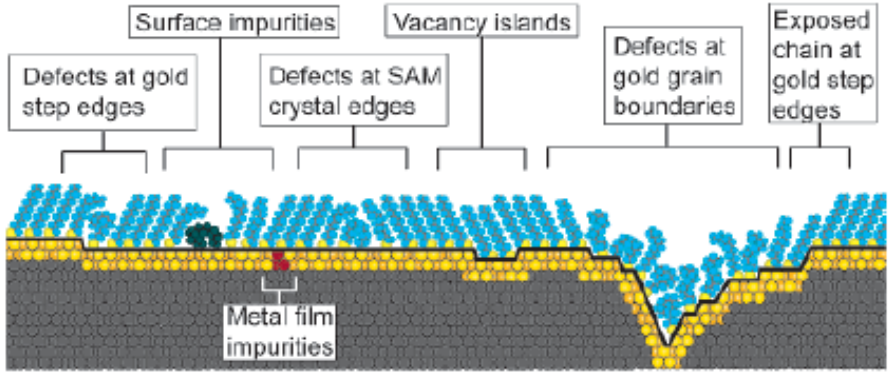

Figure 7. Schematic illustration of some of the intrinsic and extrinsic defects found in SAMs formed on polycrystalline substrates. The dark line at the metal−sulfur interface is a visual guide for the reader and indicates the changing topography of the substrate itself.

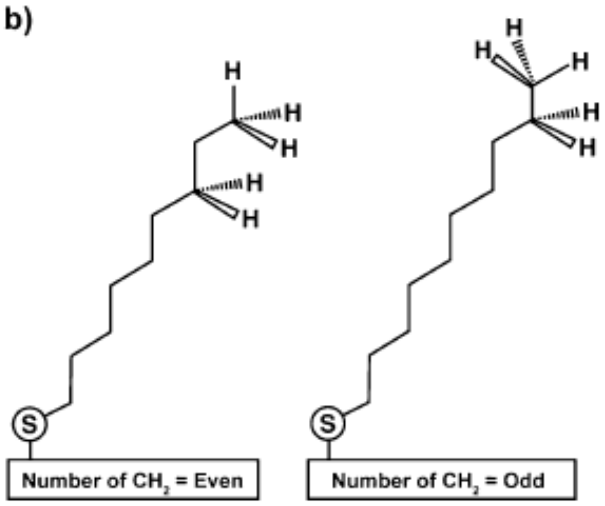

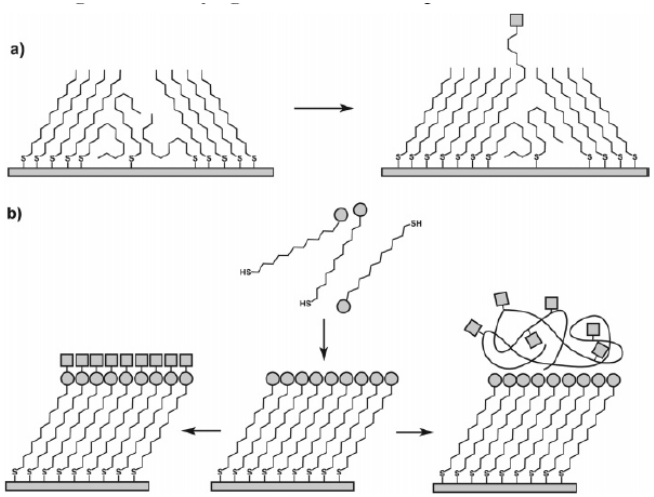

[c] (a) Insertion of a functional adsorbate at a defect site in a preformed SAM. (b) Transformation of a SAM with exposed functional groups (circles) by either chemical reaction or adsorption of another material.

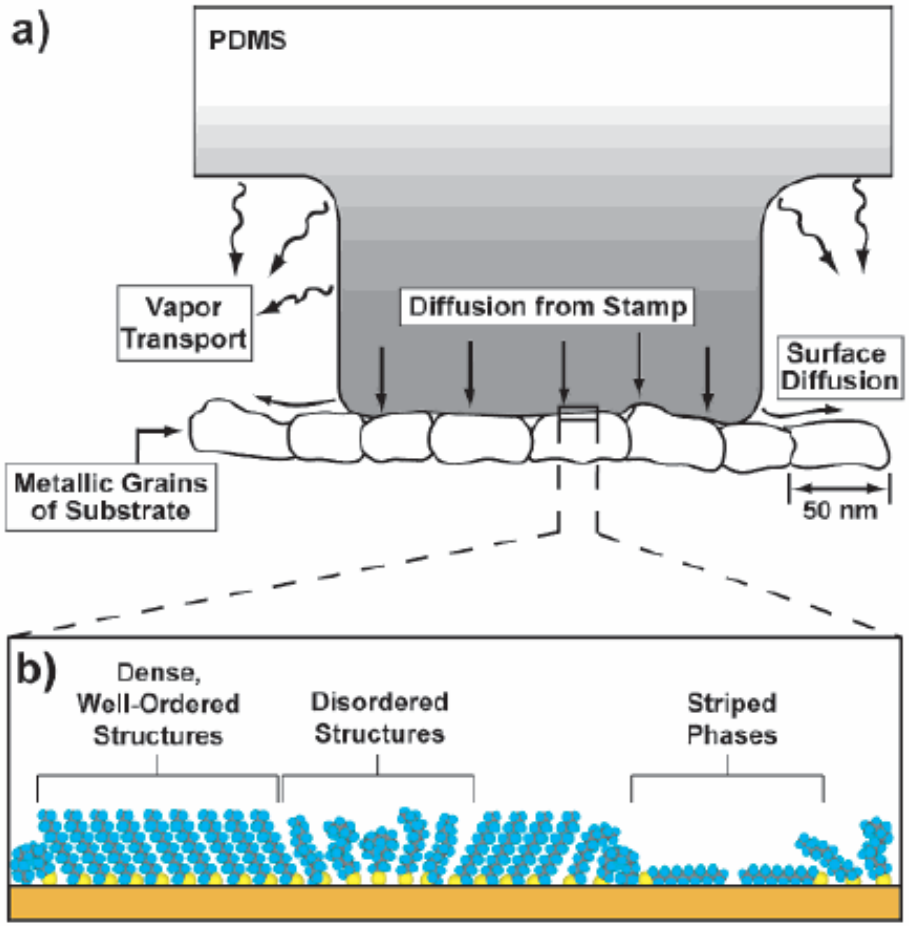

Figure 12. (a) Schematic illustration depicting the application of a PDMS stamp containing thiols to a polycrystalline metal film. The primary mechanisms of mass transport from the stamp to the surface are shown. The grayscale gradient approximates the concentration of thiols adsorbed in the stamp itself. (b) Magnified schematic view that illustrates the variety of structural arrangements found in SAMs prepared by μCP when the stamp is wetted with a 1−10 mM solution and applied to the substrate for 1−10 s.

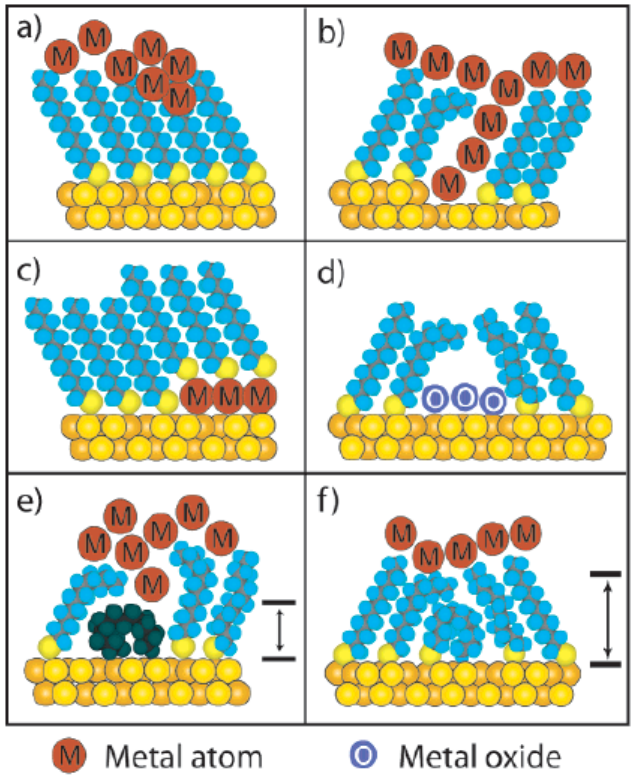

Figure 17. Schematic illustration of the types of defects in SAMs that can influence the rate of electron transfer in two-terminal (or three-terminal) devices. (a) Chemical reaction with the organic component of SAMs during evaporation of metal films. (b) Formation of metallic filaments during evaporation or operation of the device. (c) Deposition of adlayers of metal on the surface of the substrate supporting the SAM. (d) Formation of oxide impurities on the surface. (e) Organic (or organometallic) impurities in the SAM. (f) Thin regions in the SAM resulting from conformational and structural defects. In e and f the dimension normal to the surface that is denoted by the black arrows indicates the approximate shortest distance between the two metal surfaces; note that these distances are less than the nominal thickness of the ordered SAM.

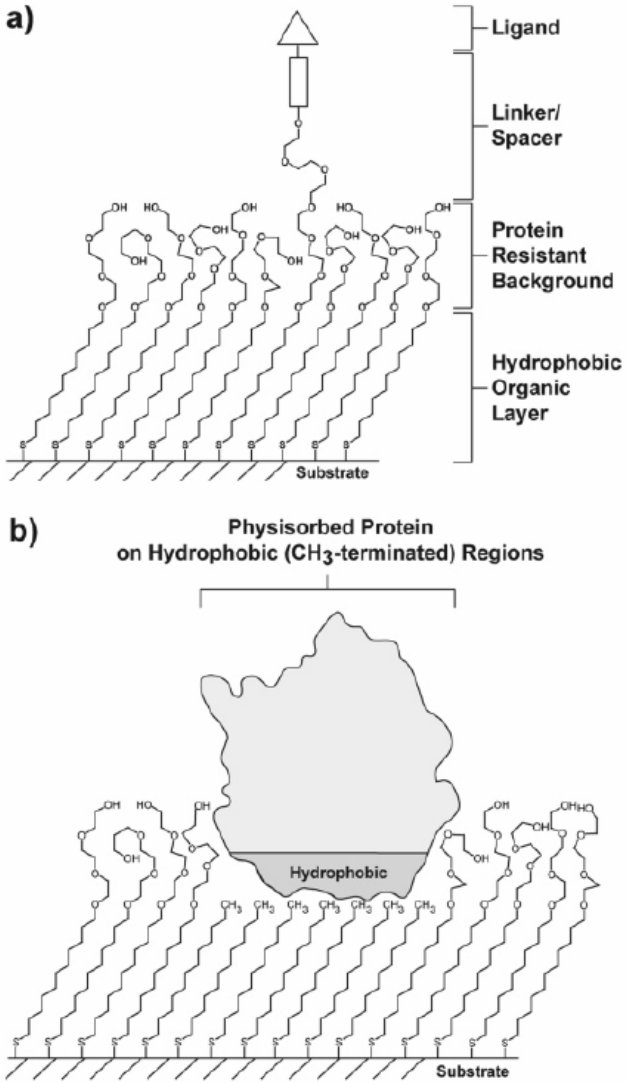

Figure 21. Schematic illustrations of (a) a mixed SAM and (b) a patterned SAM. Both types are used for applications in biology and biochemistry.

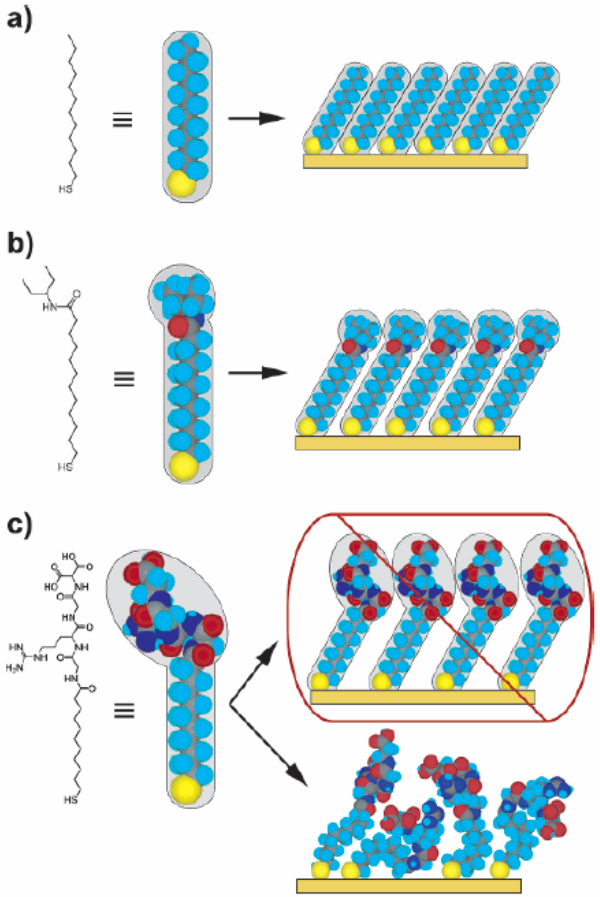

Figure 22. Schematic diagram illustrating the effects that large terminal groups have on the packing density and organization of SAMs. (a) Small terminal groups such as $-CH_3$, $-CN$, etc., do not distort the secondary organization of the organic layer and have no effect on the sulfur arrangement. (b) Slightly larger groups (like the branched amide shown here) begin to distort the organization of the organic layer, but the strongly favorable energetics of metal−sulfur binding drive a highly dense arrangement of adsorbates. (c) Large terminal groups (peptides, proteins, antibodies) sterically are unable to adopt a secondary organization similar to that for alkanethiols with small terminal groups. The resulting structures probably are more disordered and less dense than those formed with the types of molecules in a and b.

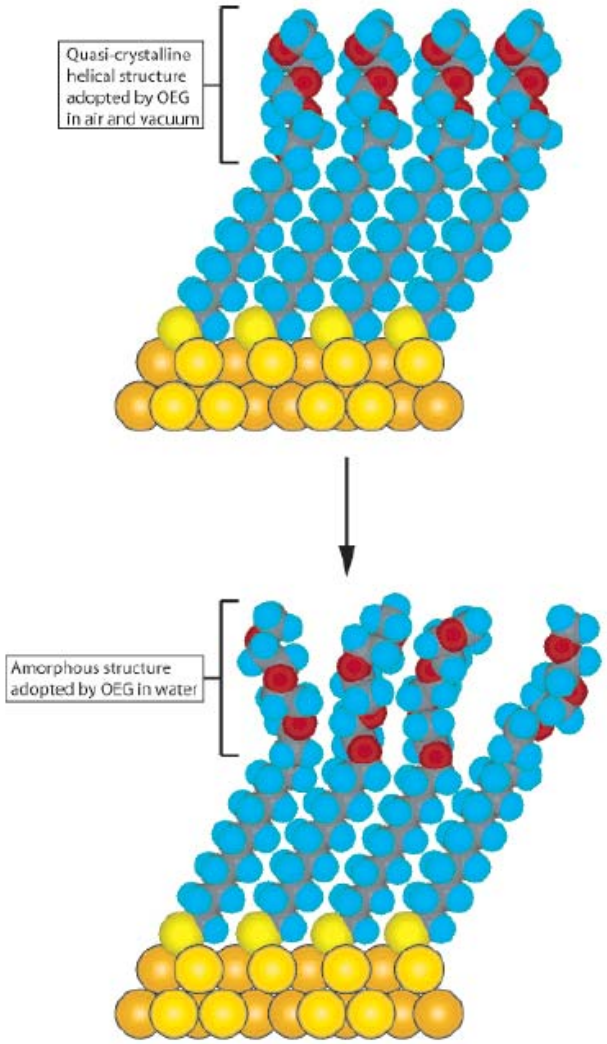

Figure 23. Schematic illustration of the order−disorder transition evidenced by SAMs of alkanethiolates terminated with triethylene glycol. The EG_3 group loses conformational ordering upon solvation in water.

Control of crystal nucleation by patterned self-assembled monolayers

NATURE | VOL 398 | 8 APRIL 1999

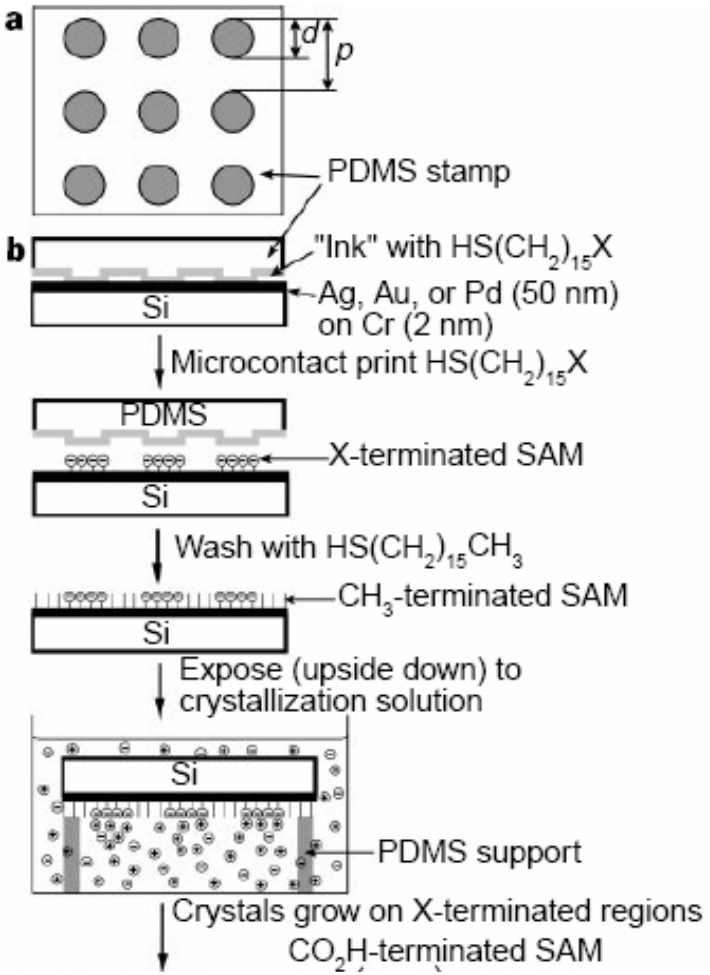

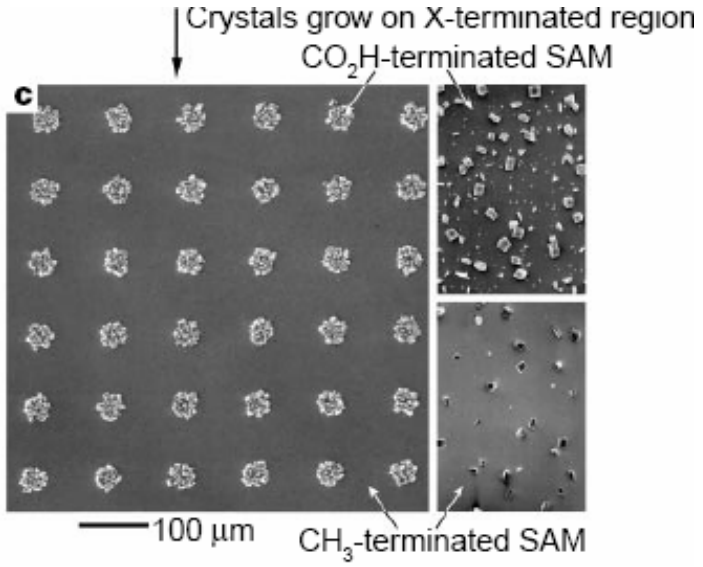

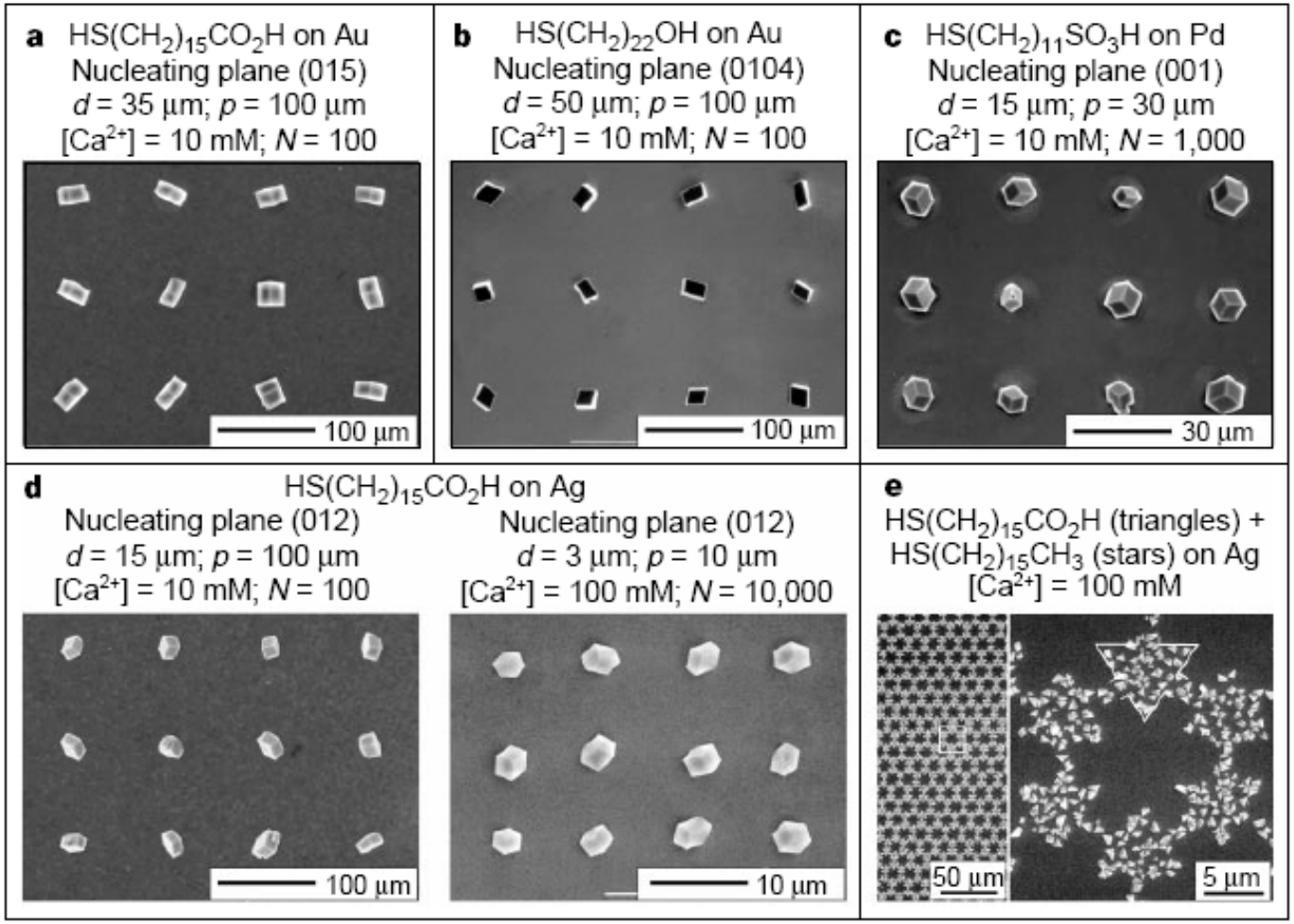
a
HS(CH2)15CO2H on Au
Nucleating plane (015)
d = 35 μm; p = 100 μm
[Ca2+] = 10 mM; N = 100
100 μm
b
HS(CH2)22OH on Au
Nucleating plane (0104)
d = 50 μm; p = 100 μm
[Ca2+] = 10 mM; N = 100
100 μm
c
HS(CH2)11SO3H on Pd
Nucleating plane (001)
d = 15 μm; p = 30 μm
[Ca2+] = 10 mM; N = 1,000
30 μm
d
HS(CH2)15CO2H on Ag
Nucleating plane (012)
d = 15 μm; p = 100 μm
[Ca2+] = 10 mM; N = 100
100 μm
Nucleating plane (012)
d = 3 μm; p = 10 μm
[Ca2+] = 100 mM; N = 10,000
10 μm
e
HS(CH2)15CO2H (triangles) +
HS(CH2)15CH3 (stars) on Ag
[Ca2+] = 100 mM
50 μm
5 μm

Patterning of organic single crystals

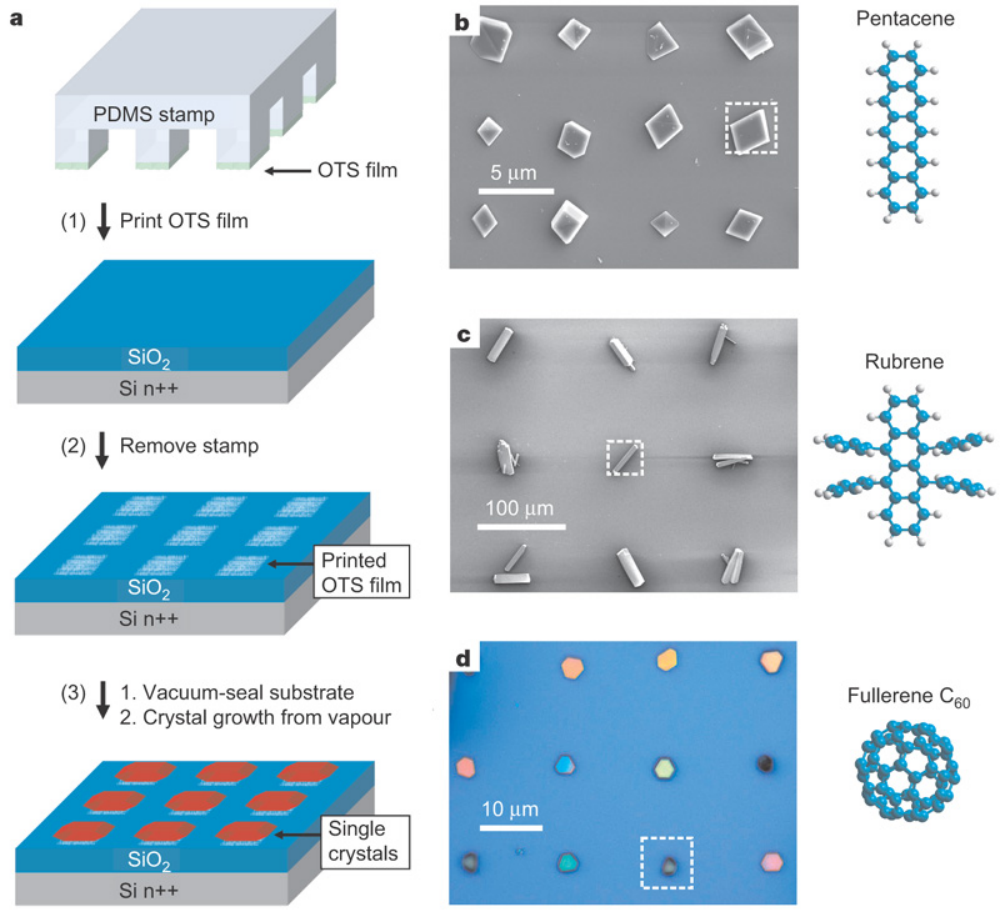

Nature 444, 913-917(14 December 2006)

Large On-Off Ratios and Negative Differential Resistance in a Molecular Electronic Device

J. Chen,[1] M. A. Reed,[1]* A. M. Rawlett,[2] J. M. Tour[2]*

19 NOVEMBER 1999 VOL 286 SCIENCE

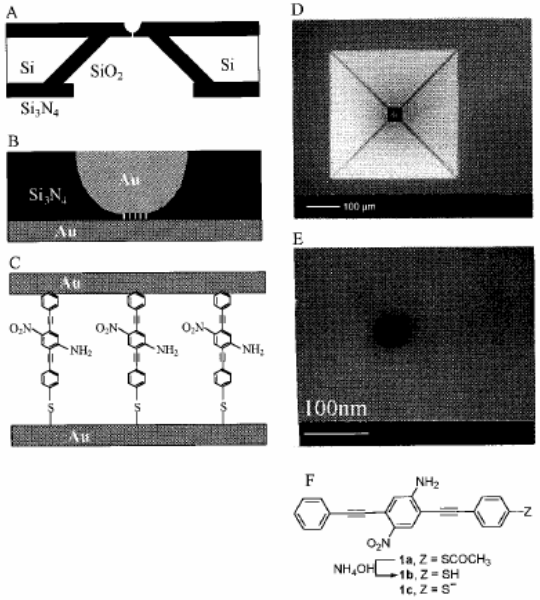

Fig. 1. Schematics of device fabrication. **(A)** Cross section of a silicon wafer with a nanopore etched through a suspended silicon nitride membrane. **(B)** Au-SAM-Au junction in the pore area. **(C)** Blowup of (B) with **1c** sandwiched in the junction. **(D)** Scanning electron micrograph (SEM) of pyramid Si structure after unisotropic Si etching [that is, the bottom view of (A)]. **(E)** SEM of an etched nanopore through the silicon nitride membrane. **(F)** The active molecular compound **1c** and its precursors the free thiol **1b** and the thiol-protected system **1a**.

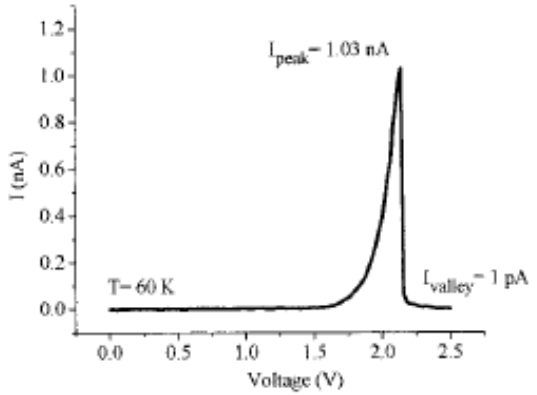

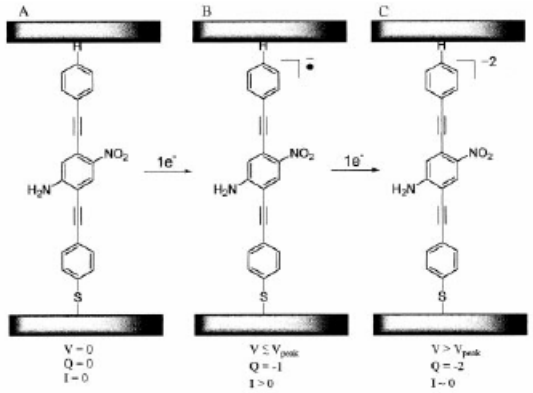

Fig. 4. Potential mechanism for the NDR effect. As voltage is applied, the molecules in the SAM **(A)** undergo a one-electron reduction to form the radical anion **(B)** that provides a conductive state. Further increase of the voltage causes another one-electron reduction to form the dianion insulating state **(C)**. Q is the charge.

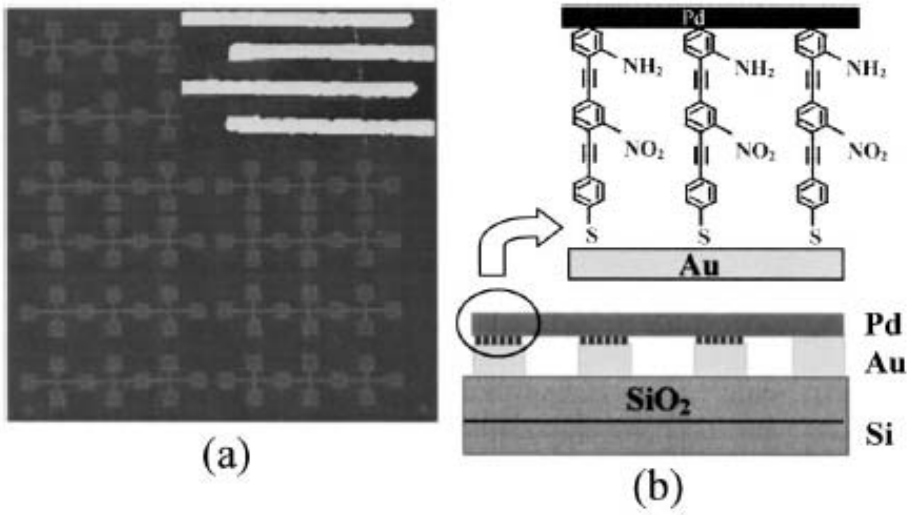

FIG. 1. (a) Optical micrograph of the nanoelectrode array. Inset: AFM image of four Au nanoelectrodes with a Pd nanowire lying across. (b) Schematic diagram of the Pd/molecular wires/Au junctions on a Si/SiO_2 substrate.

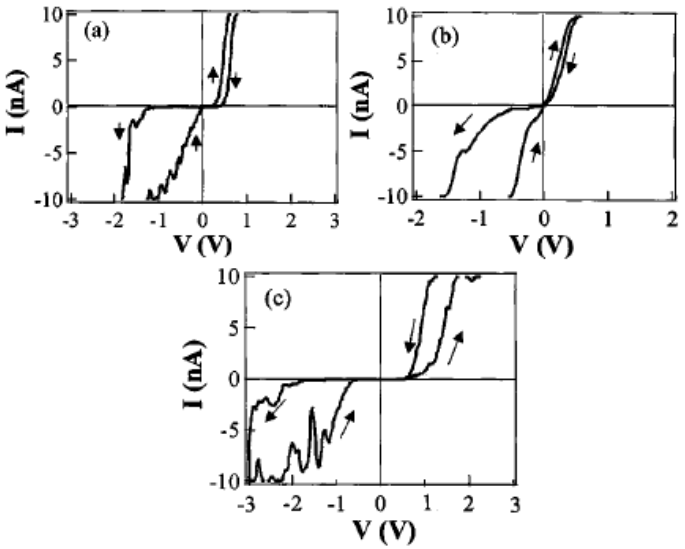

FIG. 3. Typical $I-V$ curves of molecular devices. (a), (b), and (c) correspond to molecules **a**, **b**, and **c** shown in Fig. 2, respectively.

Geometric Control of Cell Life and Death

SCIENCE • VOL. 276 • 30 MAY 1997

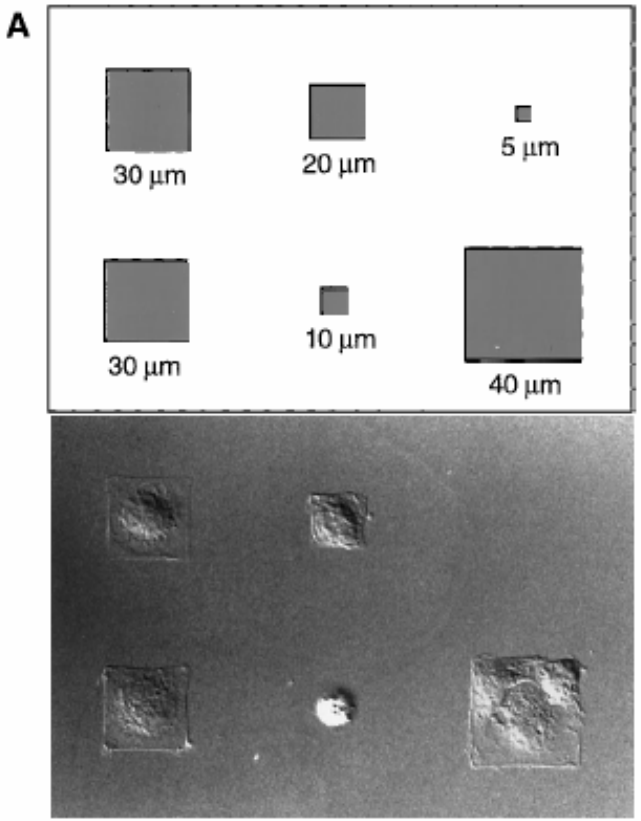

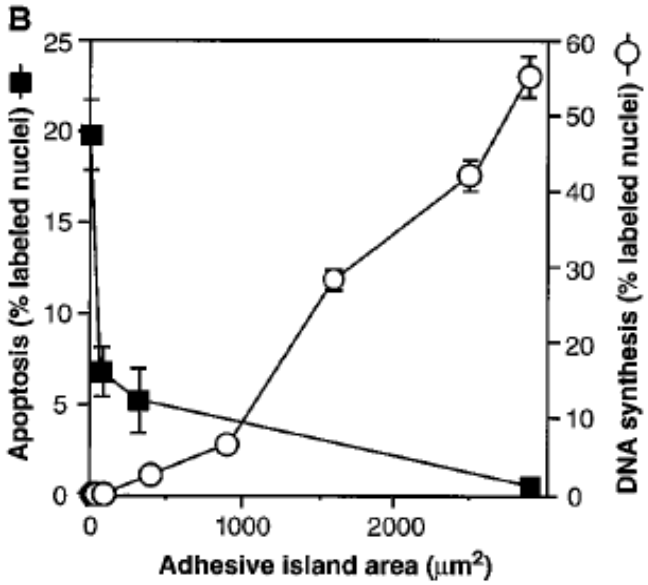

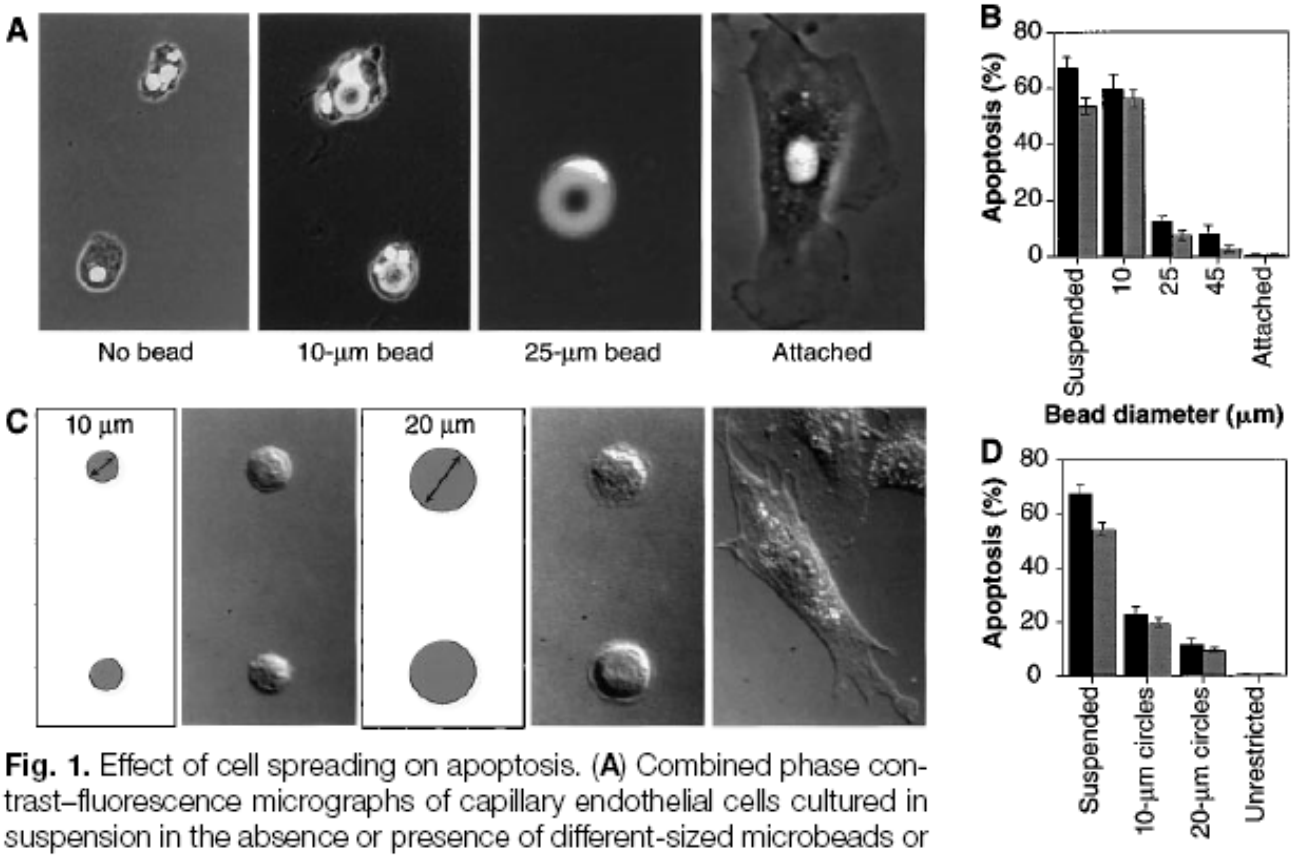

Fig. 1. Effect of cell spreading on apoptosis. (**A**) Combined phase contrast–fluorescence micrographs of capillary endothelial cells cultured in suspension in the absence or presence of different-sized microbeads or attached to a planar culture dish coated with FN for 24 hours (*28*). In the highly spread cell on the 25-μm bead, only the flattened 4′,6′-diamidino-2-phenylindole (DAPI)–stained nucleus is clearly visible. (**B**) Apoptosis in cells attached to different-sized beads, in suspension, or attached to a dish. The apoptotic index was quantitated by measuring the percentage of cells exhibiting positive TUNEL staining (black bars) (Boehringer Mannheim), which detects DNA fragmentation; similar results were obtained by analyzing changes in nuclear condensation and fragmentation in cells stained with DAPI at 24 hours (gray bars). Apoptotic indices were determined only within single cells bound to single beads. Error bars indicate SEM. (**C**) Differential interference-contrast micrographs of cells plated on substrates micropatterned with 10- or 20-μm-diameter circles coated with FN (left), by a microcontact printing method (*29*) or on a similarly coated unpatterned substrate (right). (**D**) Apoptotic index of cells attached to different-sized adhesive islands coated with a constant density of FN for 24 hours; similar results were obtained with human and bovine capillary endothelial cells (*28*). Bars same as in (B).

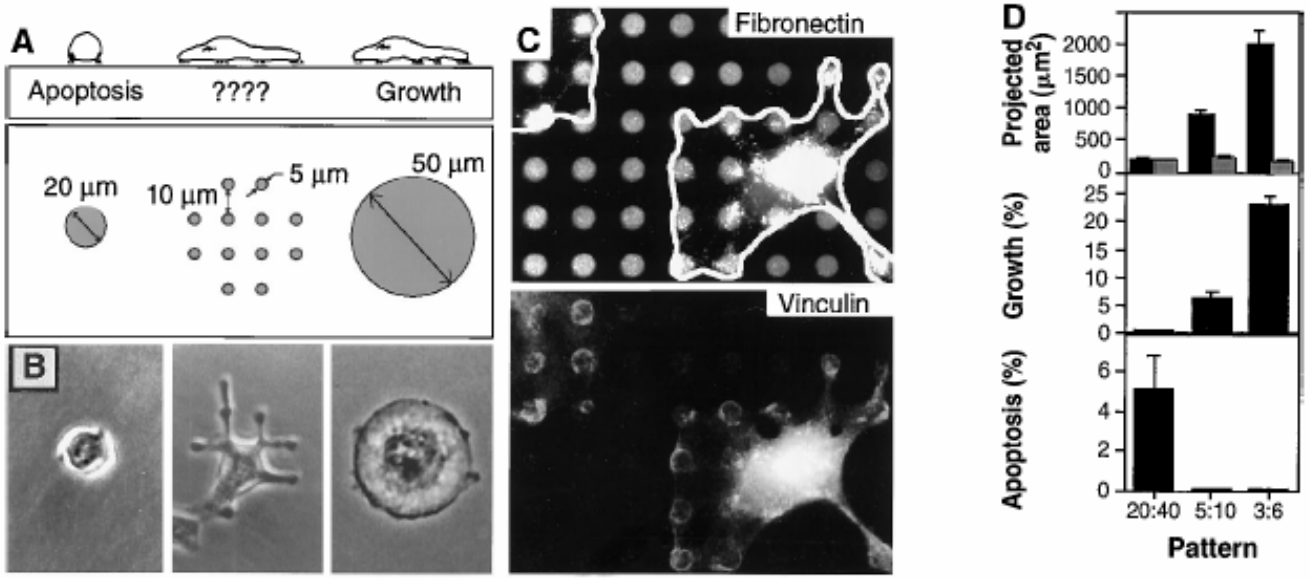

Fig. 3. Cell-ECM contact area versus cell spreading as a regulator of cell fate. (**A**) Diagram of substrates used to vary cell shape independently of the cell-ECM contact area. Substrates were patterned with small, closely spaced circular islands (center) so that cell spreading could be promoted as in cells on larger, single round islands, but the ECM contact area would be low as in cells on the small islands. (**B**) Phase-contrast micrographs of cells spread on single 20- or 50-μm-diameter circles or multiple 5-μm circles patterned as shown in (A). (**C**) Immunofluorescence micrographs of cells on a micropatterned substrate stained for FN (top) and vinculin (bottom). White outline indicates cell borders; note circular rings of vinculin staining, which coincide precisely with edges of the FN-coated adhesive islands. (**D**) Plots of projected cell area (black bars) and total ECM contact area (gray bars) per cell (top), growth index (middle), and apoptotic index (bottom) when cells were cultured on single 20-μm circles or on multiple circles 5 or 3 μm in diameter separated by 40, 10, and 6 μm, respectively.

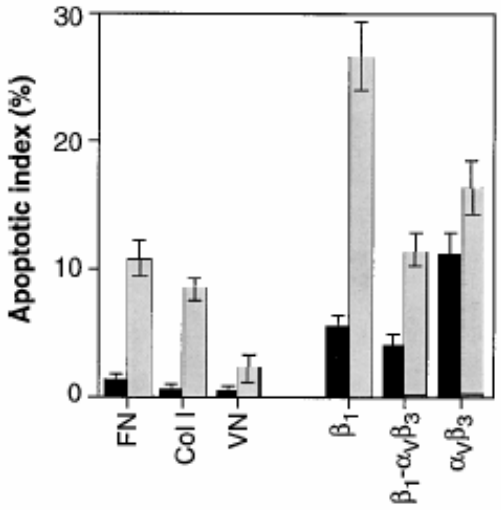

Fig. 4. Role of different integrin ligands in cell shape–regulated apoptosis. Apoptotic indices (percentage positive TUNEL staining) for cells cultured for 24 hours on unpatterned substrates (black bars) or on 20-μm circles (gray bars) coated with FN, type I collagen (Col I), vitronectin (VN), anti-β_1, anti-$\alpha_V\beta_3$, or antibodies to both integrin β_1 and integrin $\alpha_V\beta_3$ (*29*).

hexadecanethiol [$HS(CH_2)_{15}CH_3$] was printed onto gold-coated substrates with a flexible stamp containing a relief of the desired pattern. The substrate was immersed immediately in 2 mM tri(ethylene glycol)-terminated alkanethiol [$HS(CH_2)_{11}(OCH_2CH_2)_3OH$ in ethanol], which coated the remaining bare regions of gold. When these substrates were immersed in a solution of FN, vitronectin, or type I collagen (50 μg/ml in phos-

Electrochemical Desorption of Self-Assembled Monolayers Noninvasively Releases Patterned Cells from Geometrical Confinements

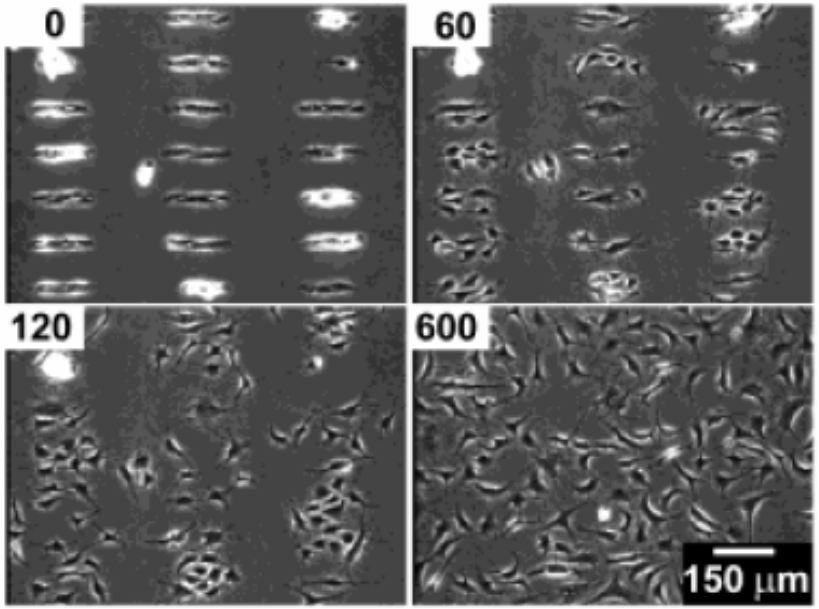

Figure 1. BCE cells were allowed to attach to a surface patterned with $C_{11}EG_3$ and C_{18}. Application of a cathodic voltage pulse (−1.2 V for 30 s in this case) released the cells from the microislands. The numbers indicate the time elapsed (in minutes) after the voltage pulse.

■ **J. AM. CHEM. SOC. 2003**, *125*, 2366−2367

Directing cell migration with asymmetric micropatterns

http://www.pnas.org/cgi/reprint/102/4/9

PNAS | January 25, 2005 | vol. 102 | no. 4 | 975

Xingyu Jiang*, Derek A. Bruzewicz*, Amy P. Wong*, Matthieu Piel†, and George M. Whitesides*‡

*Department of Chemistry and Chemical Biology, Harvard University, 12 Oxford Street, Cambridge, MA 02138; and †Department of Molecular and Cellu Biology, Harvard University, 16 Divinity Avenue, Cambridge, MA 02138

Contributed by George M. Whitesides, December 2, 2004

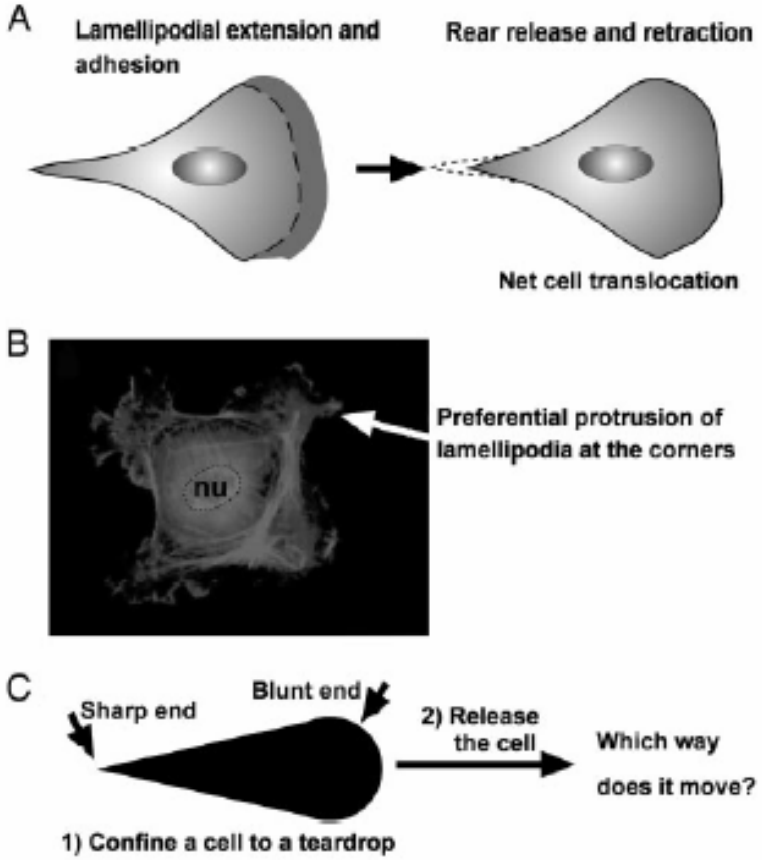

Fig. 1. A problem on cell motility. (*A*) A cartoon illustration of the migration of a typical mammalian cell on a flat surface. This teardrop shape is found in many types of cells. (*B*) Cells confined to squares preferentially extend their lamellipodia from the corners. nu, nucleus. (*C*) If a cell is confined to a shape of teardrop, will the cell preferentially extend its lamellipodia from the sharp end or from the blunt end? If released from confinement, in which direction will it likely move?

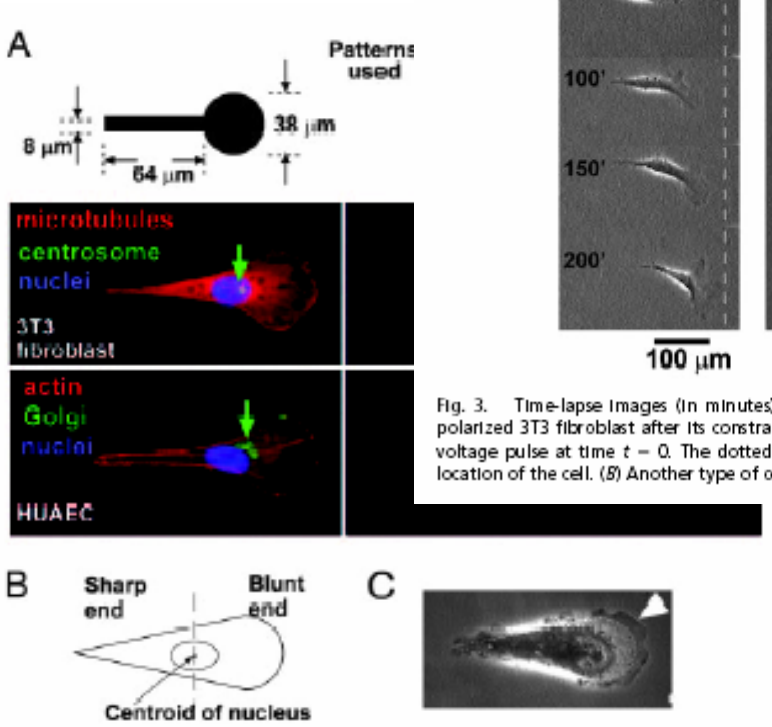

Fig. 2. Asymmetric patterns polarize immobilized cells. (*A*) The Golgi and the centrosome are located closer to the half of a cell with the blunt end. We used phallodin, antigolgin, DAPI, antitubulin, and antipericentrin to identify actin (red), the Golgi (green), the nucleus (blue), microtubules (red), and the centrosome (green), respectively. The green arrows indicate the location of centrosomes in 3T3 cells and Golgi in human umbilical artery endothelial cells (HUAEC). (*B*) We divided the cell into a half with the sharp end and a half with the blunt end by a vertical line drawn at the centroid of the nucleus; >80% ($n = 30$) of the centrosomes and Golgi were localized in the region of the wide end. (*C*) The lamellipodia of immobilized 3T3 cells tended to extend more from the blunt end as well (arrowhead). The dotted line indicates the edges of the adhesive pattern.

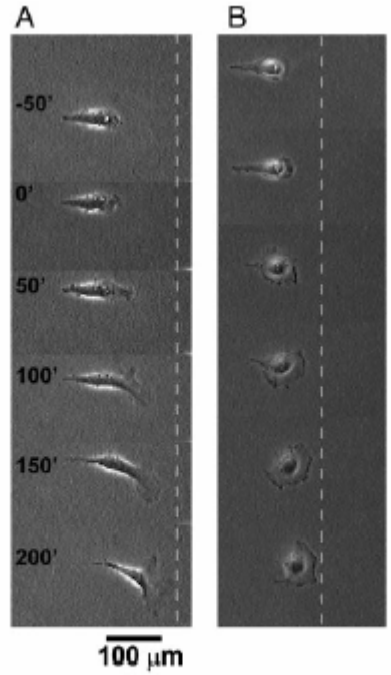

Fig. 3. Time-lapse images (in minutes) show the motility of an initially polarized 3T3 fibroblast after its constraint is released. (*A*) We applied the voltage pulse at time $t = 0$. The dotted line serves as a reference for the location of the cell. (*B*) Another type of cell, COS-7, shows similar behavior.

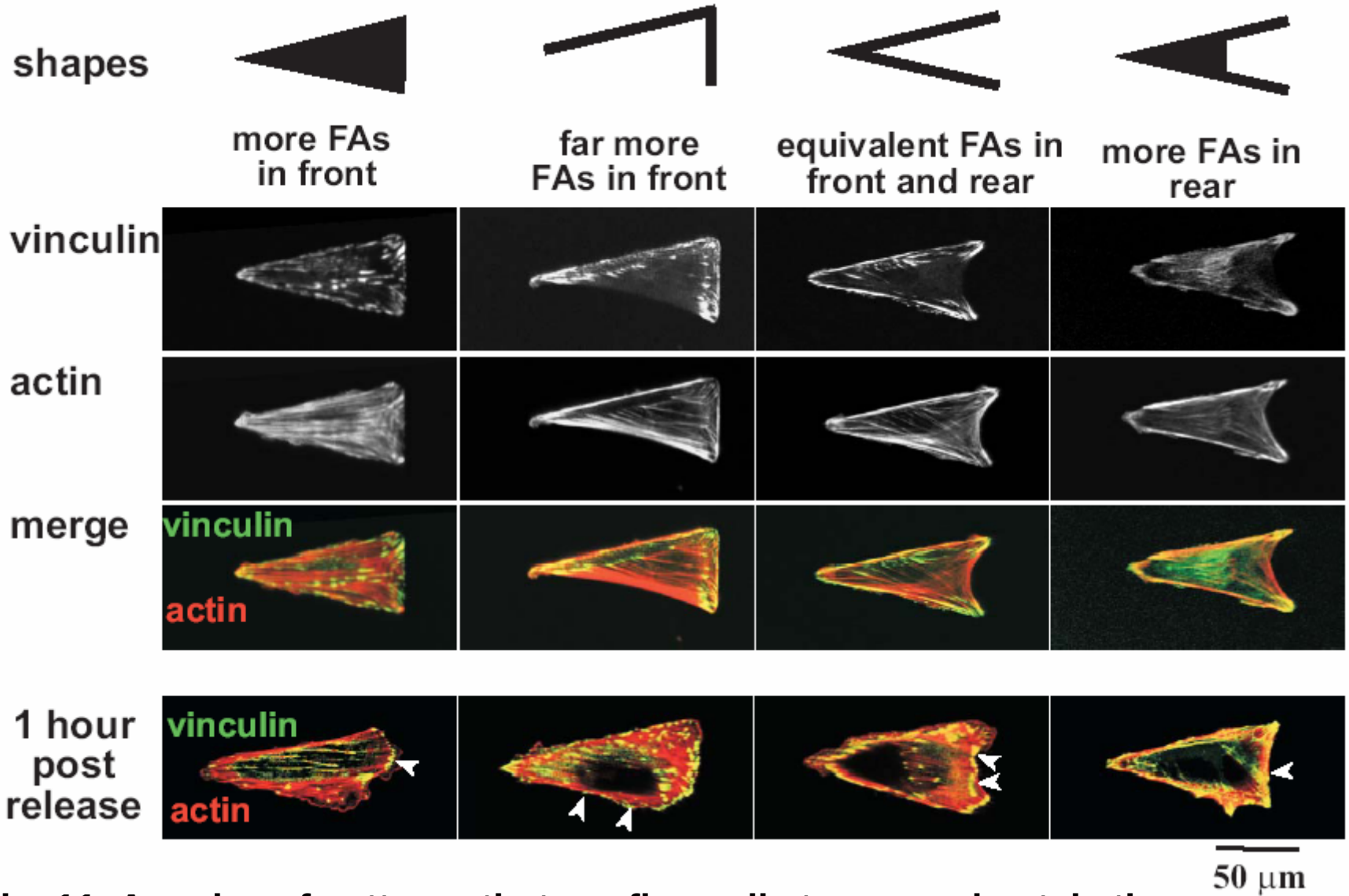

Fig. 11. A series of patterns that confine cells to approximately the same projected geometry (visualized by the actin cytoskeleton) but distribute the focal adhesions (FAs; visualized by immunostaining for vinculin) differently. The bottom row shows that new focal adhesions formed 1 h after release in areas that were inert to attachment of cells prior to release (arrowheads).

Soft-Lithography

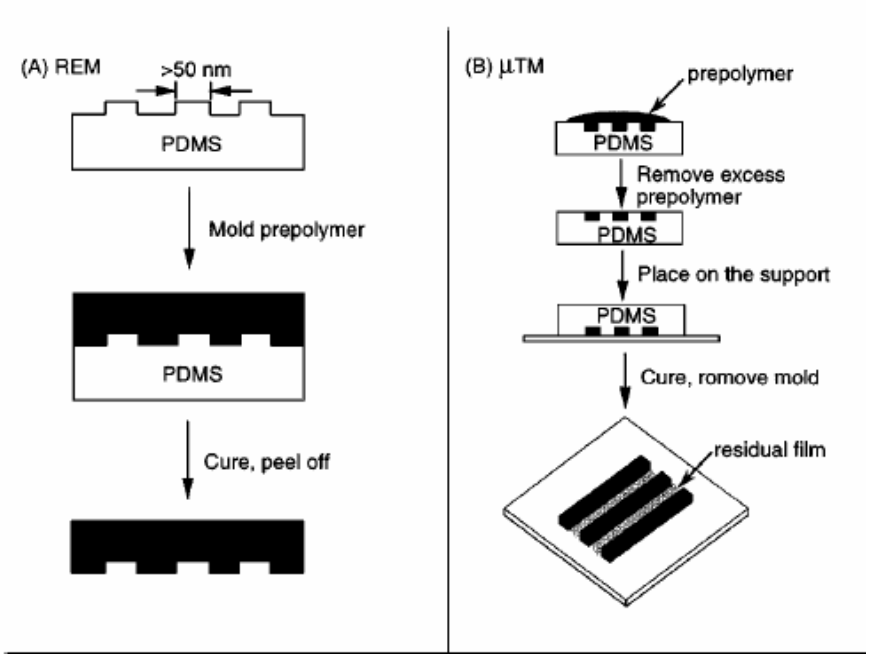

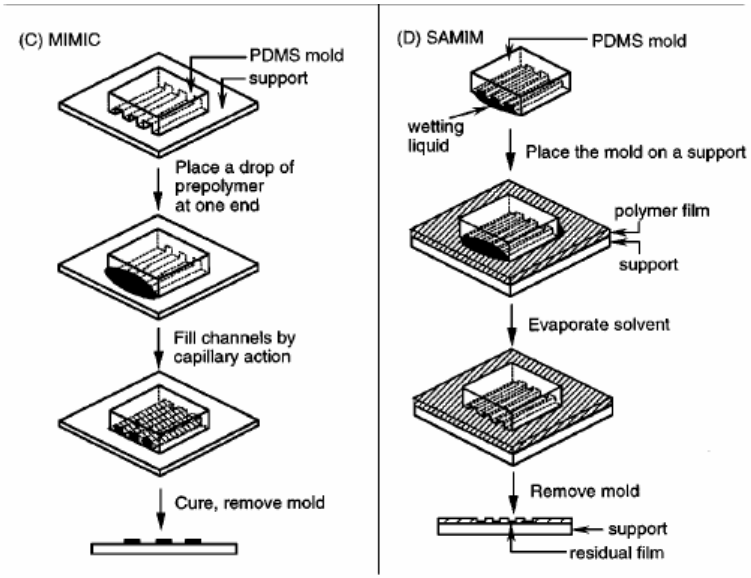

Figure 5 Schematic illustration of procedures for (*a*) replica molding (REM), (*b*) microtransfer molding (μTM), (*c*) micromolding in capillaries (MIMIC), and (*d*) solvent-assisted micromolding (SAMIM).

Electrophoresis 2002, 23, 3461–3473

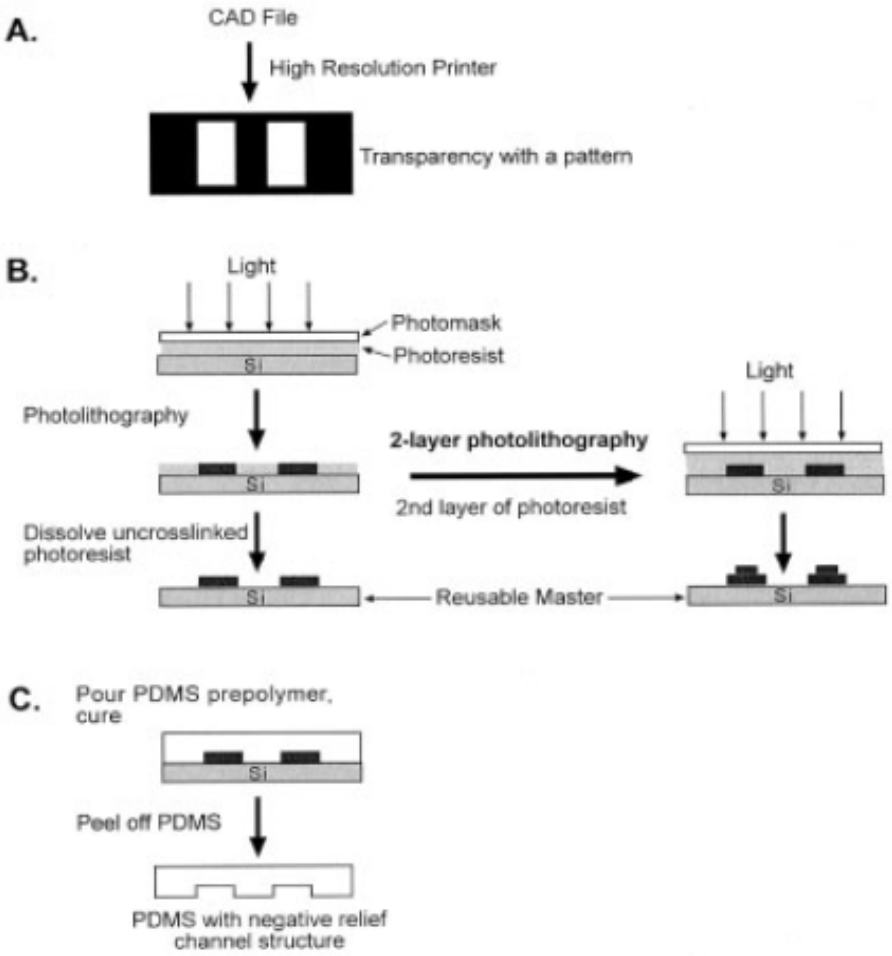

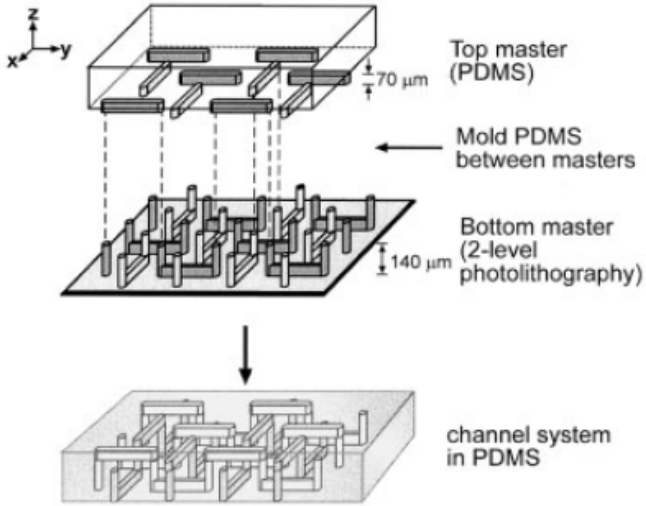

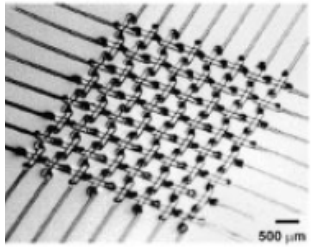

D.

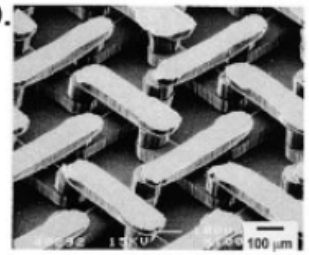

Replication Result

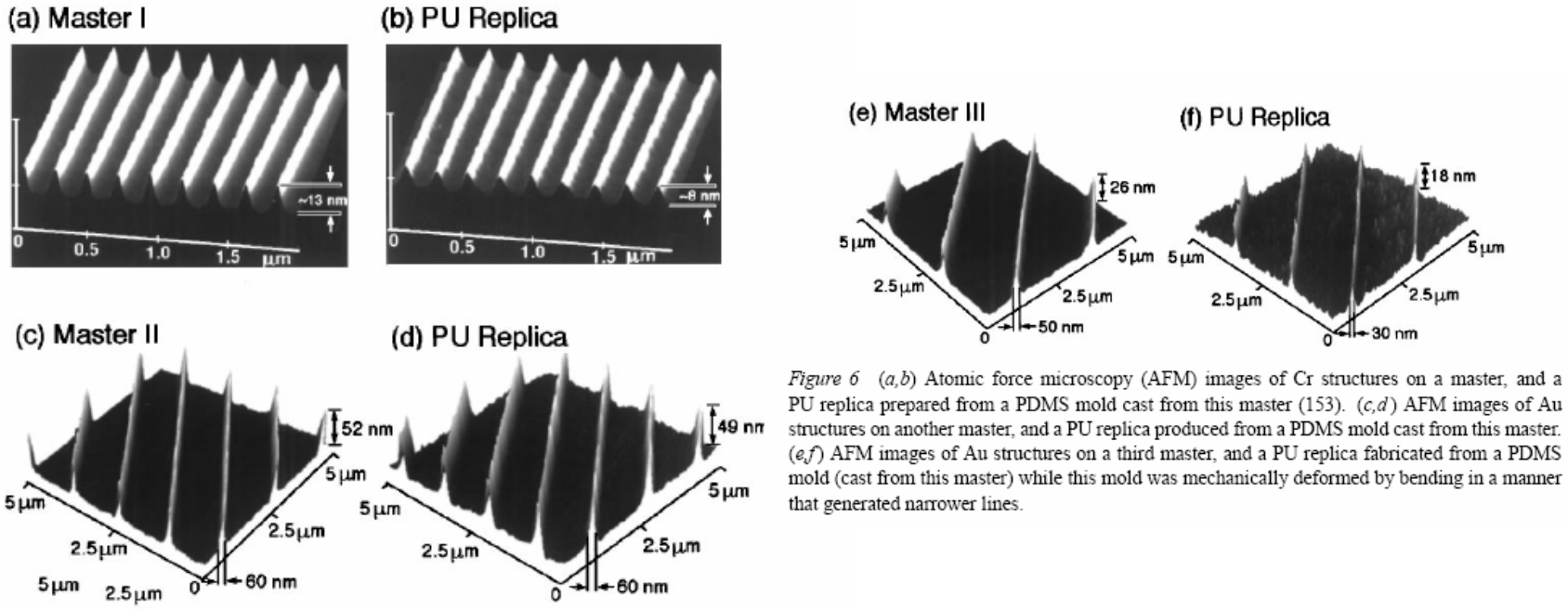

Figure 6 (*a,b*) Atomic force microscopy (AFM) images of Cr structures on a master, and a PU replica prepared from a PDMS mold cast from this master (153). (*c,d*) AFM images of Au structures on another master, and a PU replica produced from a PDMS mold cast from this master. (*e,f*) AFM images of Au structures on a third master, and a PU replica fabricated from a PDMS mold (cast from this master) while this mold was mechanically deformed by bending in a manner that generated narrower lines.

Gold Surface Modification

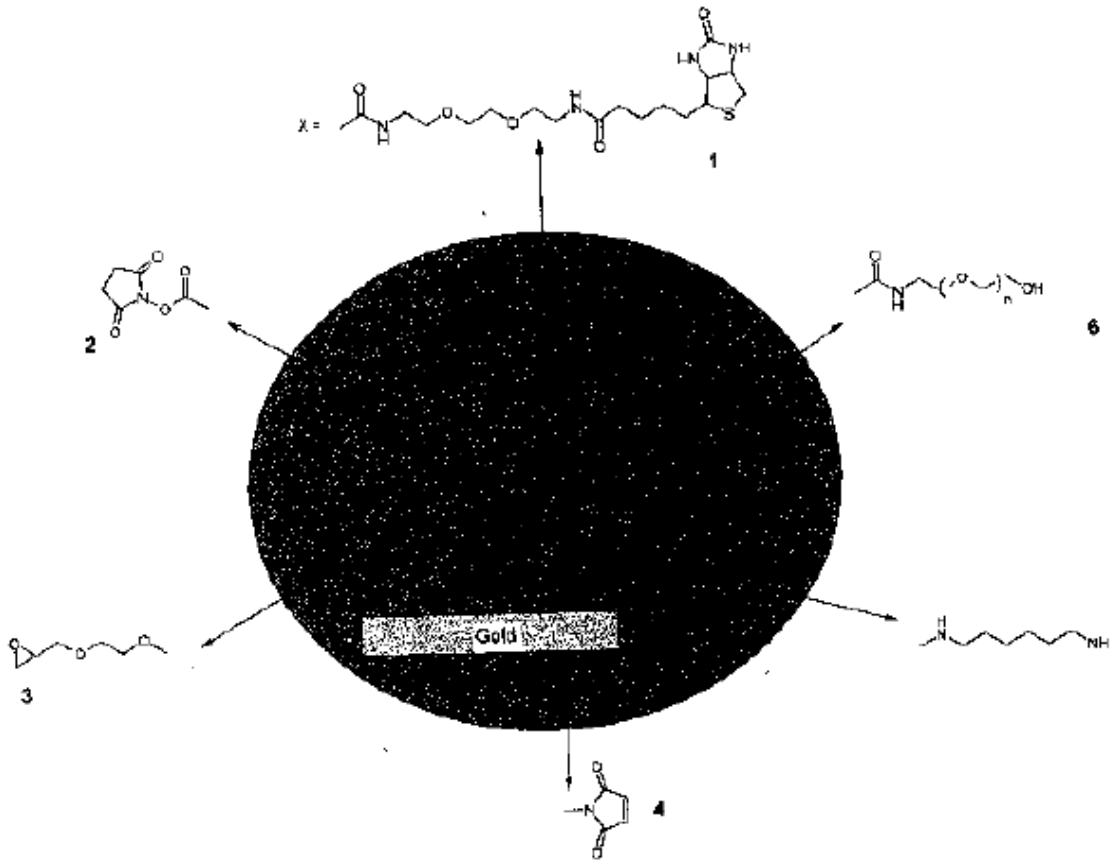

Scheme 2.3 Schematic respresentation of long-chain alkanethiol monolayers (e.g. 16 mercapto-hexadecanoic acid) on gold with different terminal functional groups.

1, biotin; 2, NHS-ester (NHS, N-hydroxysuccin-imide); 3, epoxy-ethylene glycol;
4, maleimide; 5, diaminohexane; 6 oligo (ethylene glycol).

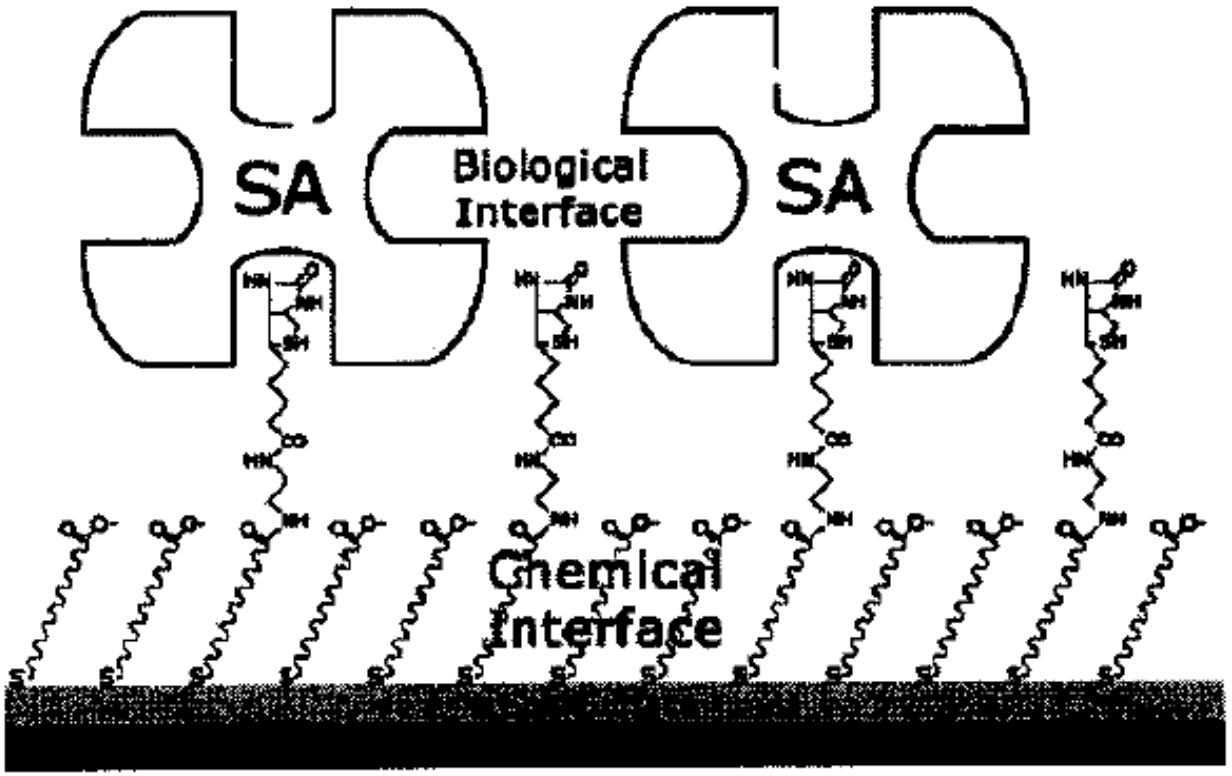

Figure 2.3 Schematic respresentation of a steptavidin sensor surface assembled on a reaction-controlled biotinylated SAM [28].

Biotin

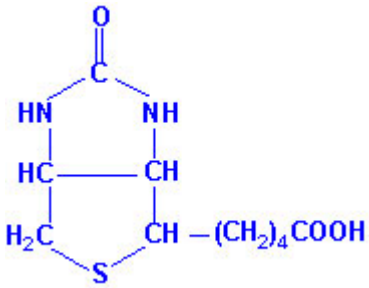

Avidin has a very strong affinity for biotin with a KD (dissociation constant) of approximately 10^{-15} M^{-1}

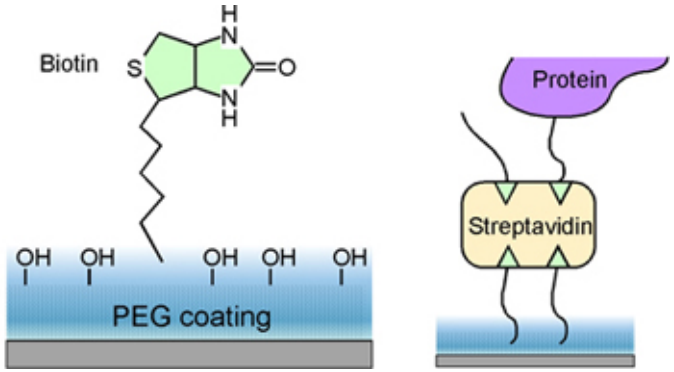

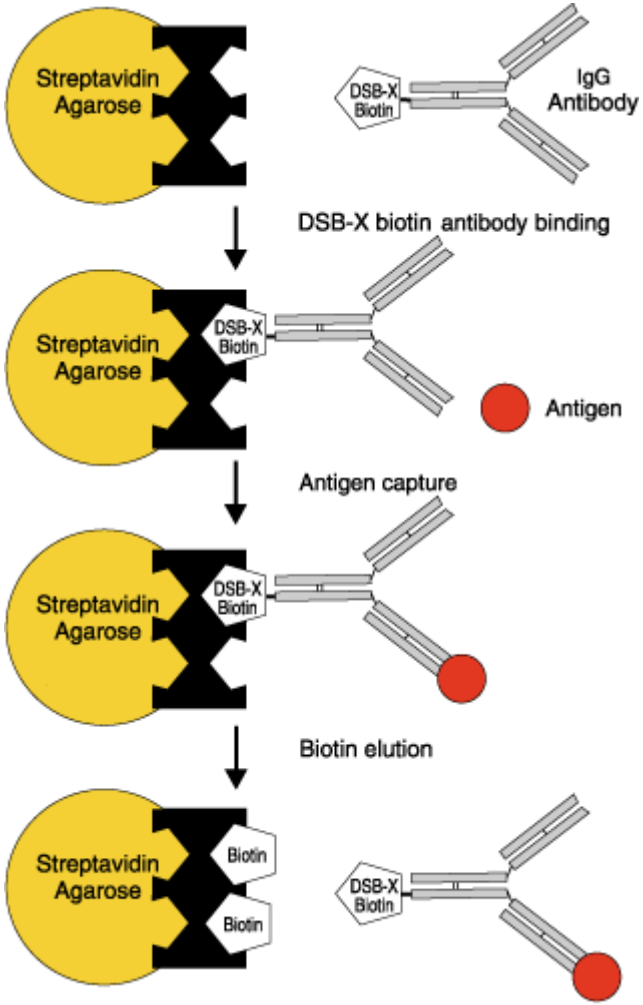
Streptavidin Agarose
DSB-X Biotin
IgG Antibody
DSB-X biotin antibody binding
Antigen
Antigen capture
Biotin elution
Biotin
Biotin

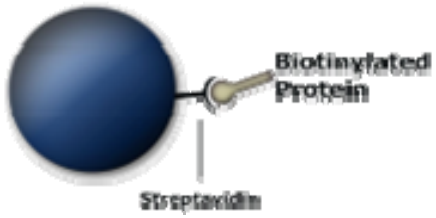
Biotinylated Protein
Streptavidin

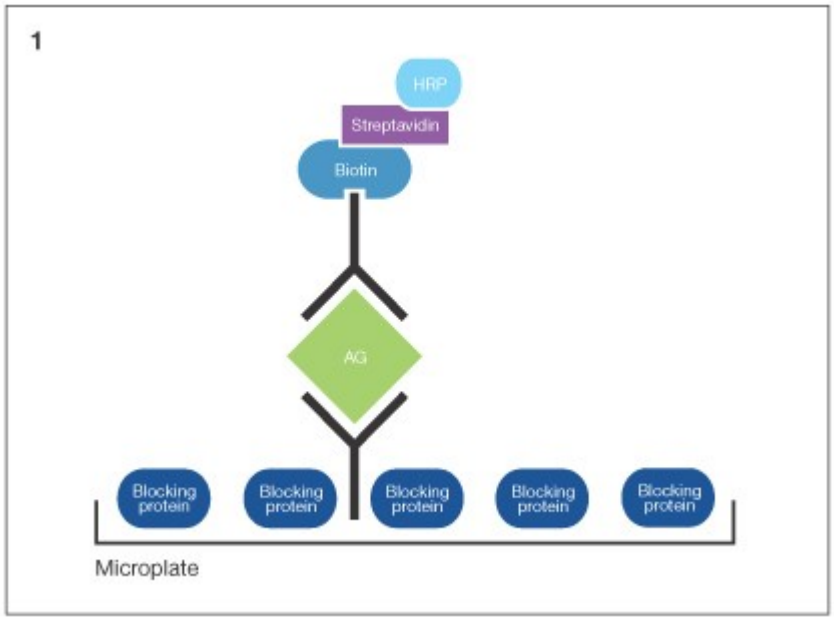
1
HRP
Streptavidin
Biotin
AG
Blocking protein
Blocking protein
Blocking protein
Blocking protein
Blocking protein
Microplate

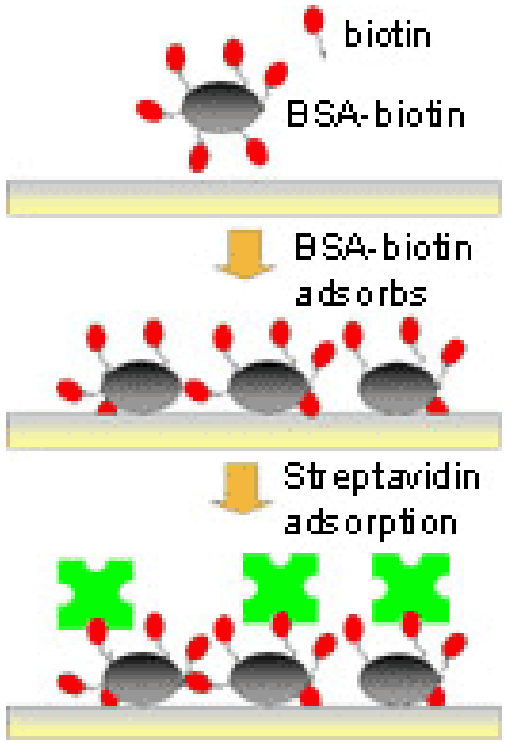
biotin
BSA-biotin
BSA-biotin adsorbs
Streptavidin adsorption

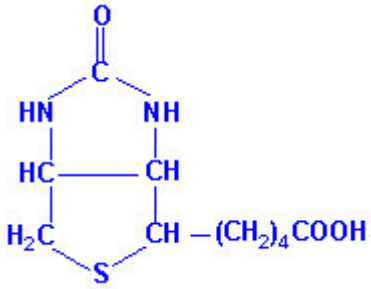

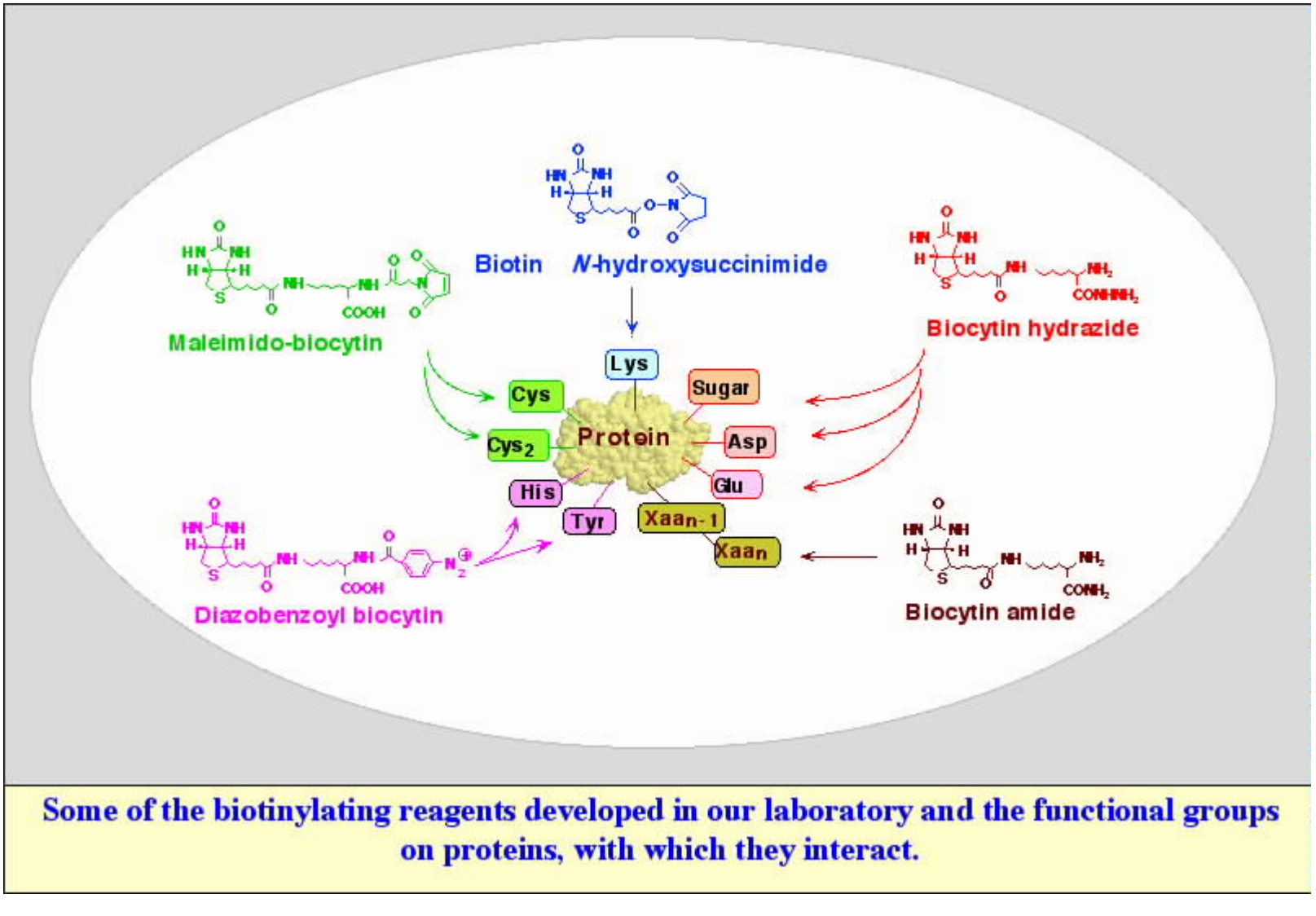

Some of the biotinylating reagents developed in our laboratory and the functional groups on proteins, with which they interact.

Protein Labeling

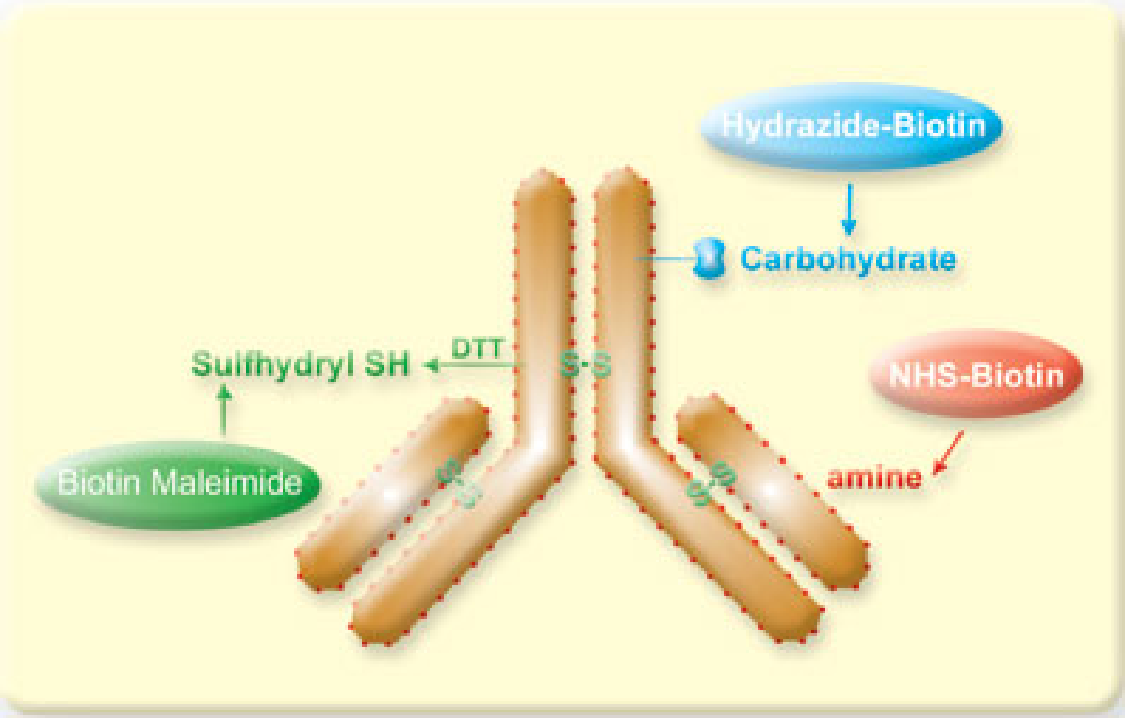

Amine Reactive Labeling

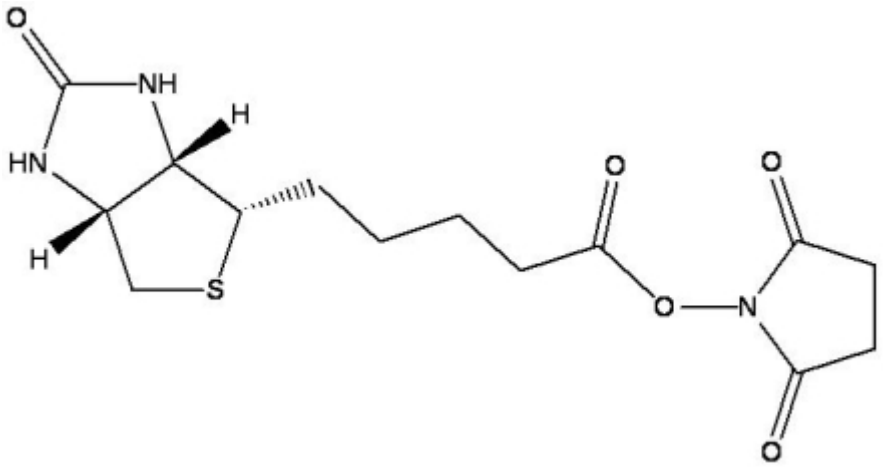

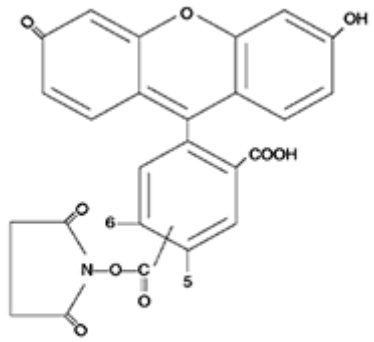

NHS-Fluorescein
MW 473.4

Sulfhydryl Labeling

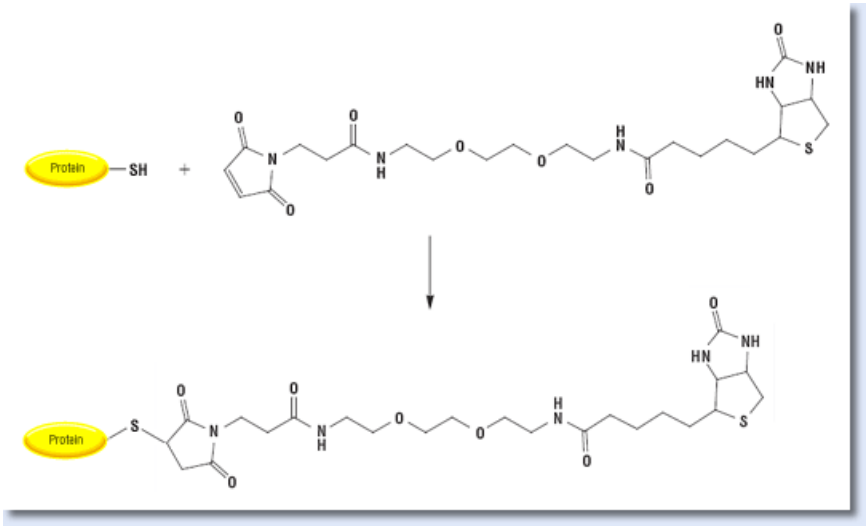

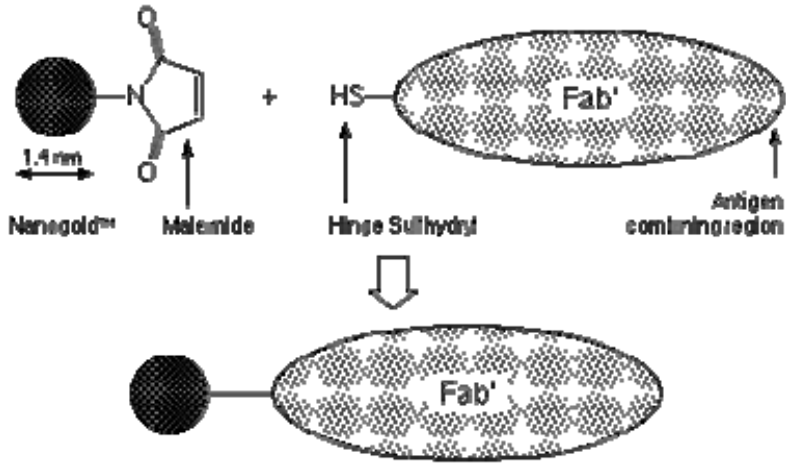

Biotin modification

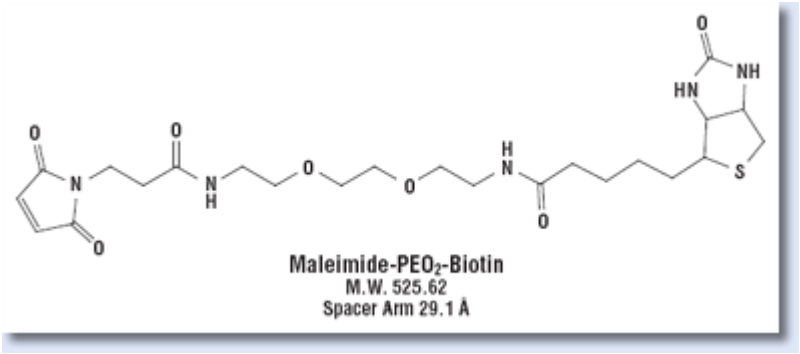

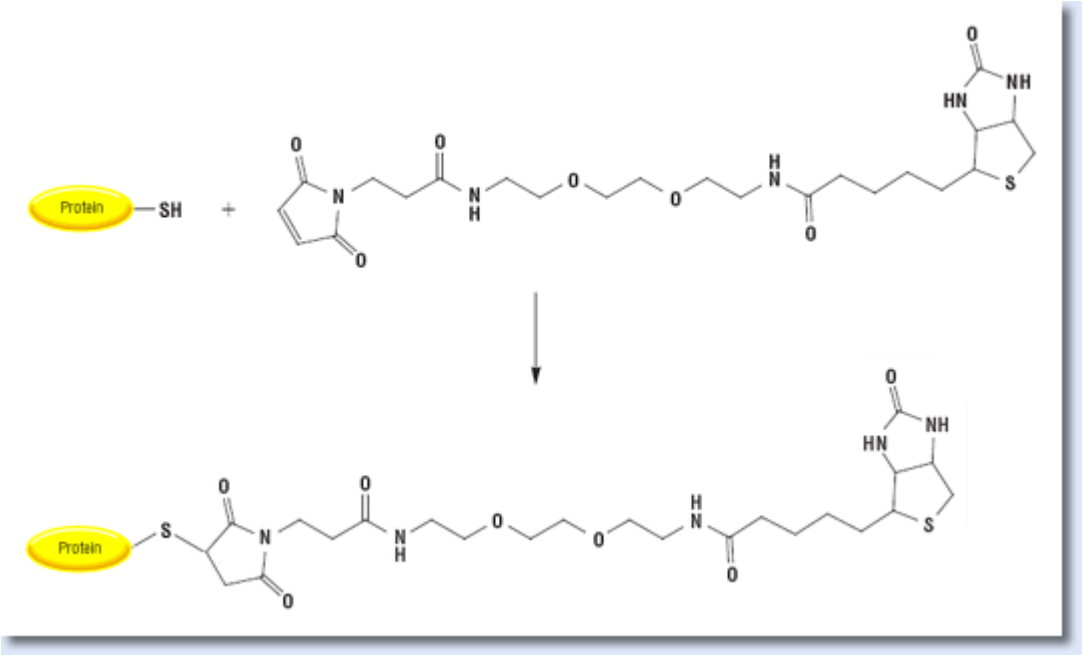

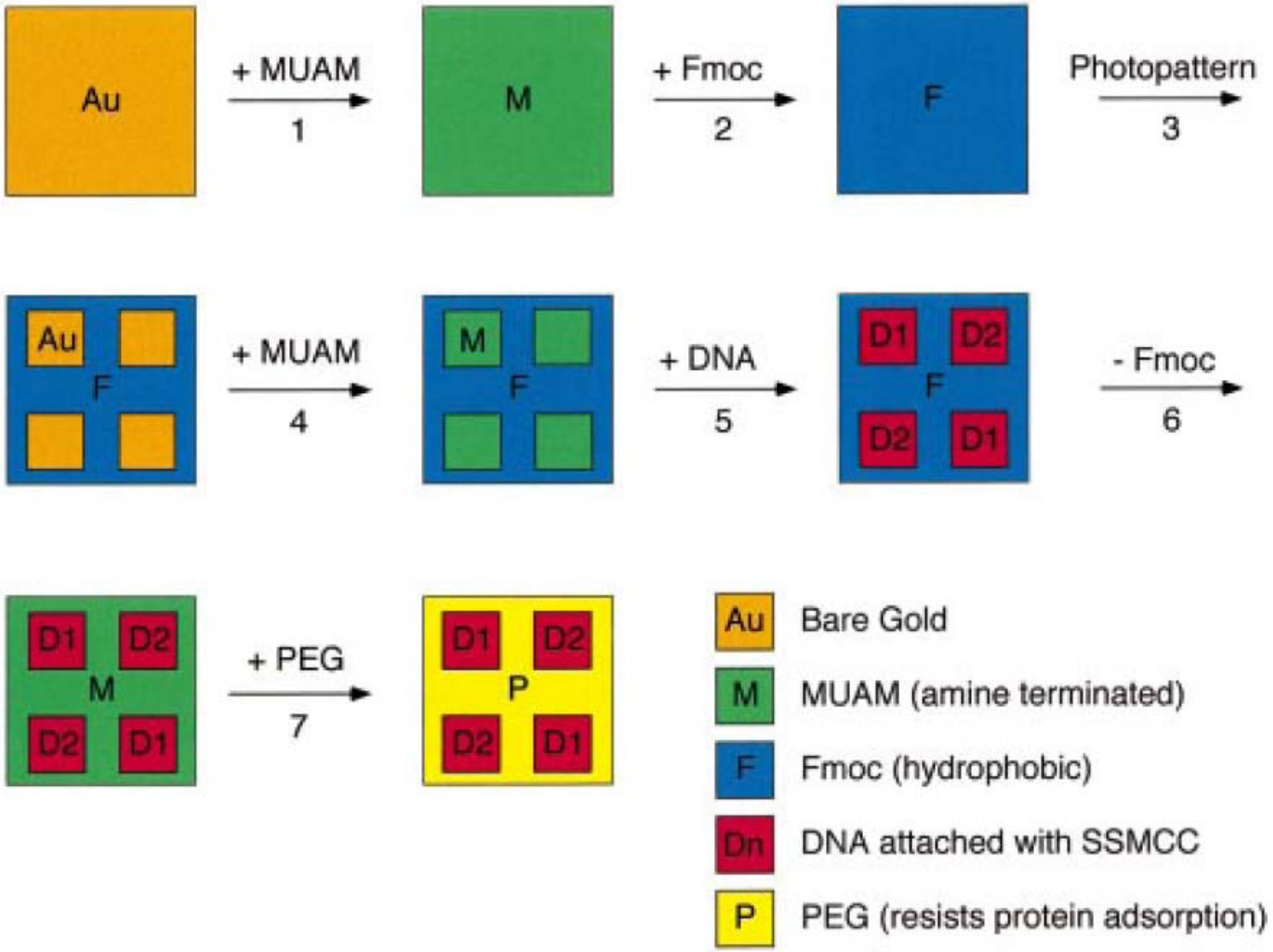

Figure 1. Fabrication scheme for the construction of multi-element DNA arrays. A clean gold surface is reacted with the amine-terminated alkanethiol MUAM, and subsequently reacted with Fmoc-NHS to create a hydrophobic surface. This surface is then exposed to UV radiation through a quartz mask and rinsed with solvent to remove the MUAM+Fmoc from specific areas of the surface, leaving bare gold pads. These bare gold areas on the sample surface are filled in with MUAM, resulting in an array of MUAM pads surrounded by a hydrophobic Fmoc background. Solutions of DNA are then delivered by pipet onto the specific array locations and are covalently bound to the surface via the bifunctional linker SSMCC. In the final two steps, the Fmoc-terminal groups on the array background are removed and replaced by PEG groups which prohibit the nonspecific binding of analyte proteins to the background.

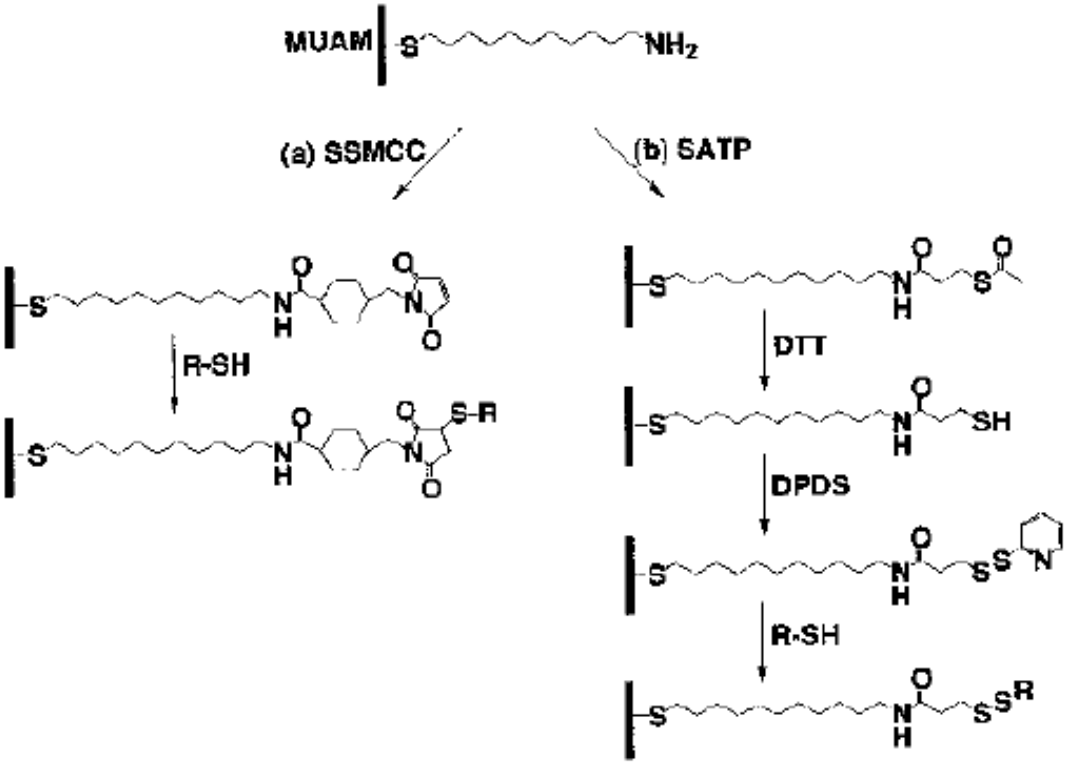

Figure 5.3 Surface attachment chemistry for the immobilization of thiol-modified DNA and cysteine-containing peptides: (a) The linker SSMCC is reacted with a well-packed self-assembled monolayer of 11-mercaptoundecylamine (MUAM) to create a maleimide-modified surface. The maleimide surface is then used to covalently attach thiol-modified DNA or cysteine-containing peptides. (b) In the second approach, SATP is reacted with MUAM to create a protected thiol surface. Upon deprotection with a basic solution containing DTT, the free sulfhydryl is reacted with dipyridyl disulfide to create a pyridyl disulfide surface. Thiol–disulfide exchange reactions are used to couple thiol-containing biomolecules to the surface.

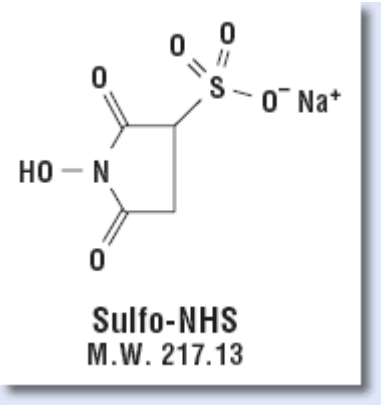

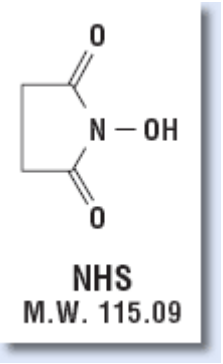

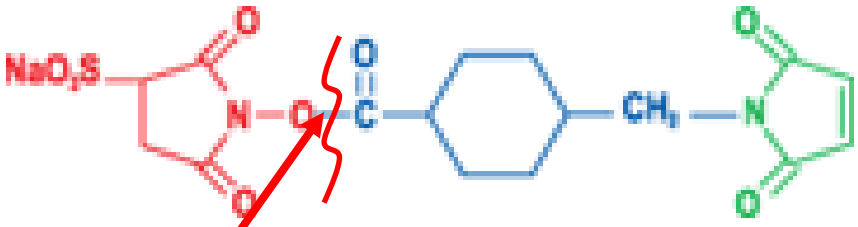

SulfoSuccinimidyl-4-(N-Maleimidomethyl)Cyclohexane-1-Carboxylate
SSMCC

The most popular NH_2- and SH- crosslinker

N-hydroxysuccinimide

NH_2 => amide

$R_1NH_2 + NHS\text{-}R_2 = >R_1NHC{=}OR_2$

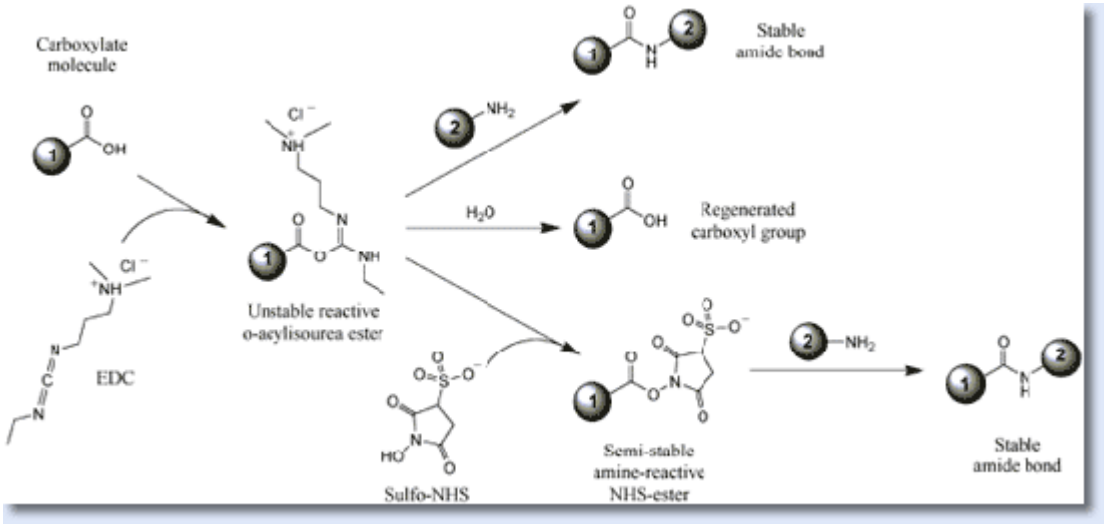

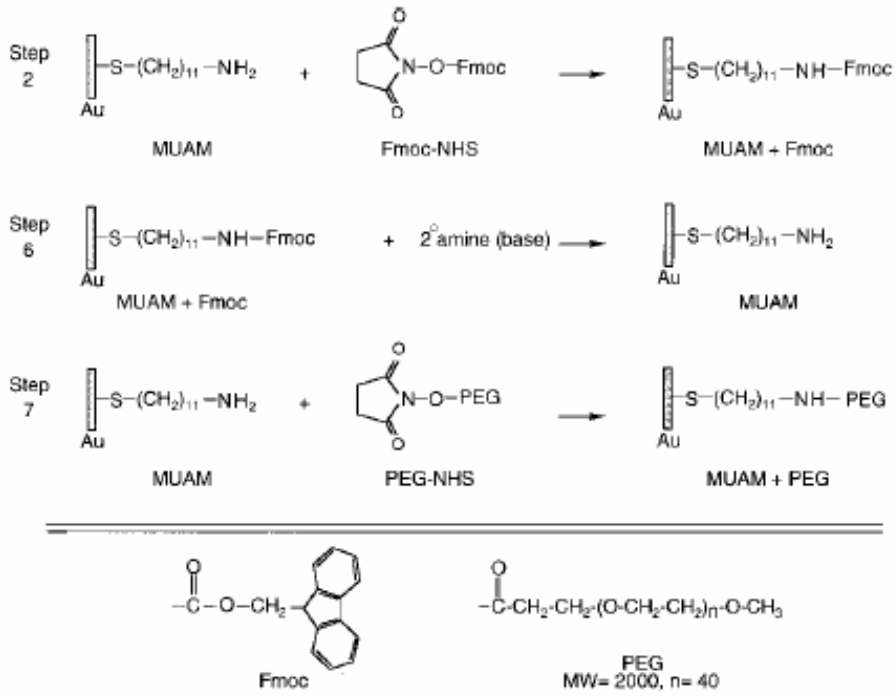

Figure 2. Surface reaction scheme showing the steps involved in the reversible modification of the array background. (Step 2) The starting amine-terminated alkanethiol surface (MUAM) is reacted with the Fmoc-NHS protecting group to form a carbamate linkage thus creating a hydrophobic Fmoc-terminated surface. (Step 6) After DNA immobilization (see Figure 3), the hydrophobic Fmoc group is removed from the surface with a basic secondary amine, resulting in the return of the original MUAM surface. (Step 7) In the final array fabrication step, the deprotected MUAM is reacted with PEG-NHS to form an amide bond that covalently attaches PEG to the array surface.

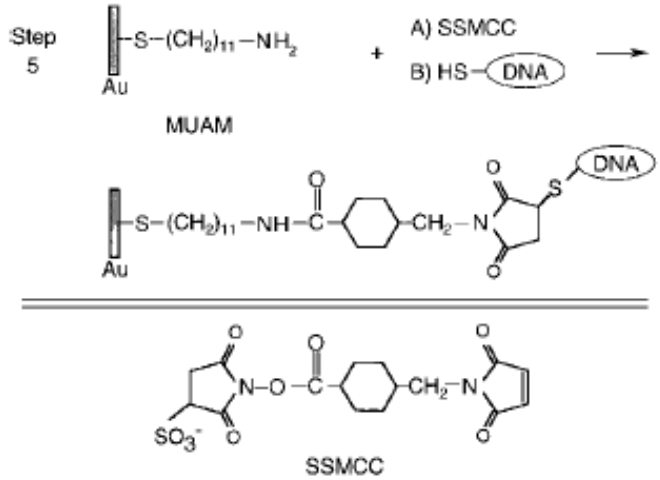

Figure 3. Surface reaction scheme showing the immobilization of thiol-terminated DNA to the array surface. In Step 5 of the DNA array fabrication, the heterobifunctional linker SSMCC is used to attach 5′-thiol modified oligonucleotide sequences to reactive pads of MUAM. This linker contains an NHSS ester functionality (reactive toward amines) and a maleimide functionality (reactive toward thiols). The surface is first exposed to a solution of the linker, whereby the NHSS ester end of the molecule reacts with the MUAM surface. Excess linker is rinsed away and the array surface is then spotted with 5′-thiol-modified DNA that reacts with the maleimide groups forming a covalent bond to the surface monolayer.

Surface Modification

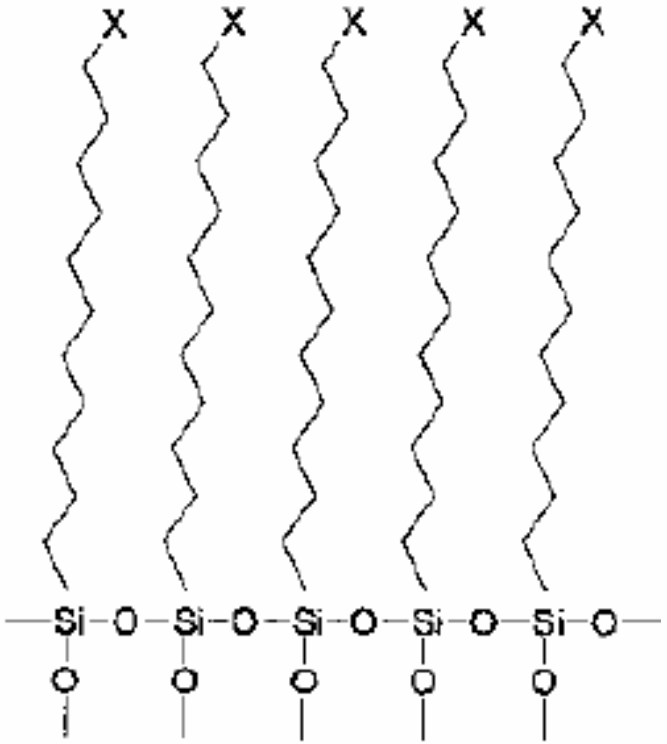

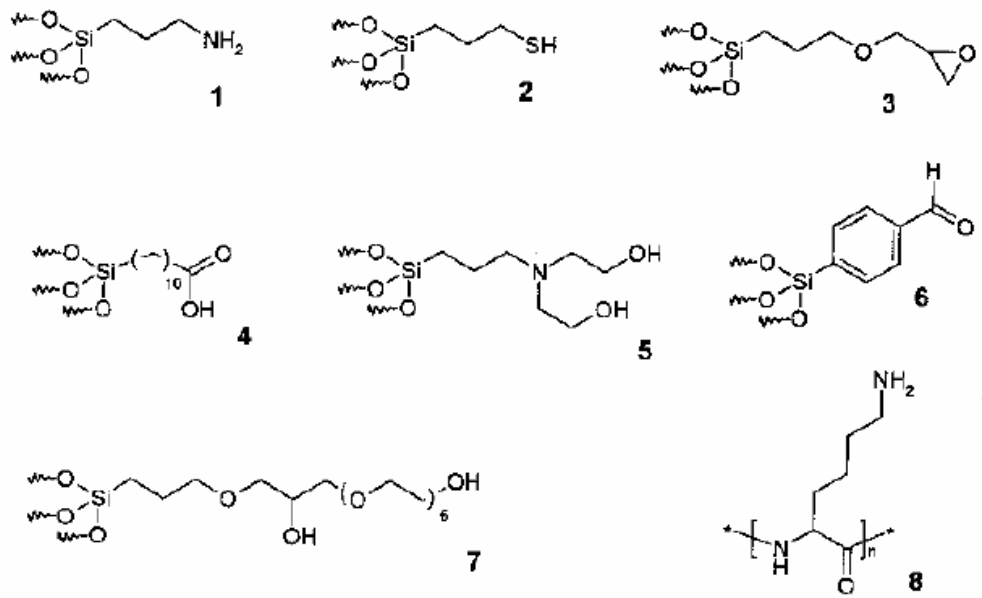

Scheme 2.2 Reagents for derivatization of glass surfaces. 1 APTES = aminopropyltriethoxysilane; **2** MPTS = 3-mercaptopropyltrimethoxysilane; **3** GPTS = glycidoxypropyltrimethoxysilane; **4** TETU = triethoxysilane undecanoic acid; **5** HE-APTS = bis(hydroxyethyl)aminopropyltriethoxysilane); **6** 4-trimethoxysilylbenzaldehyde; **7** GPTS/HEG = glycidoxypropyltrimethoxysilane-hexaethylene glycol; **8** poly(lysine).

Scheme 2.1 2D schematic description of a polysiloxane monolayer on a glass surface (X = terminal functional

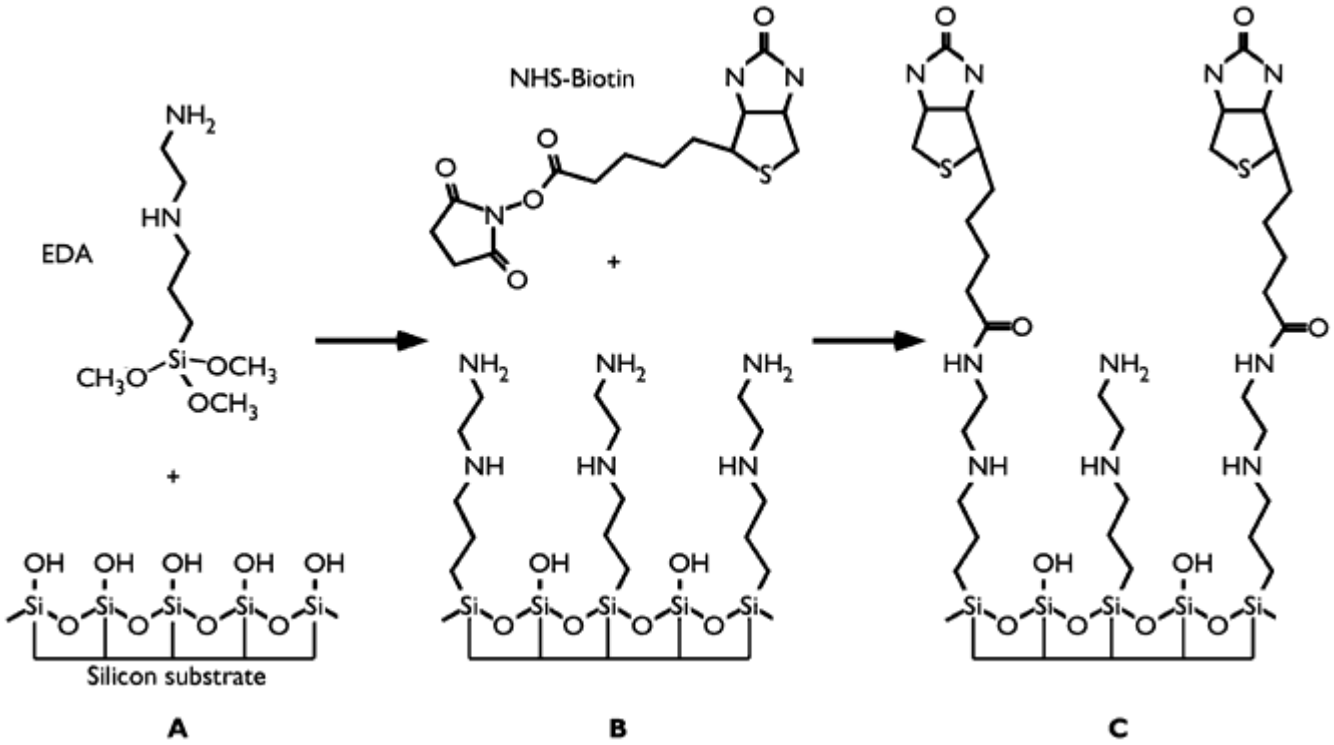
NHS-Biotin
EDA
Silicon substrate
A
B
C

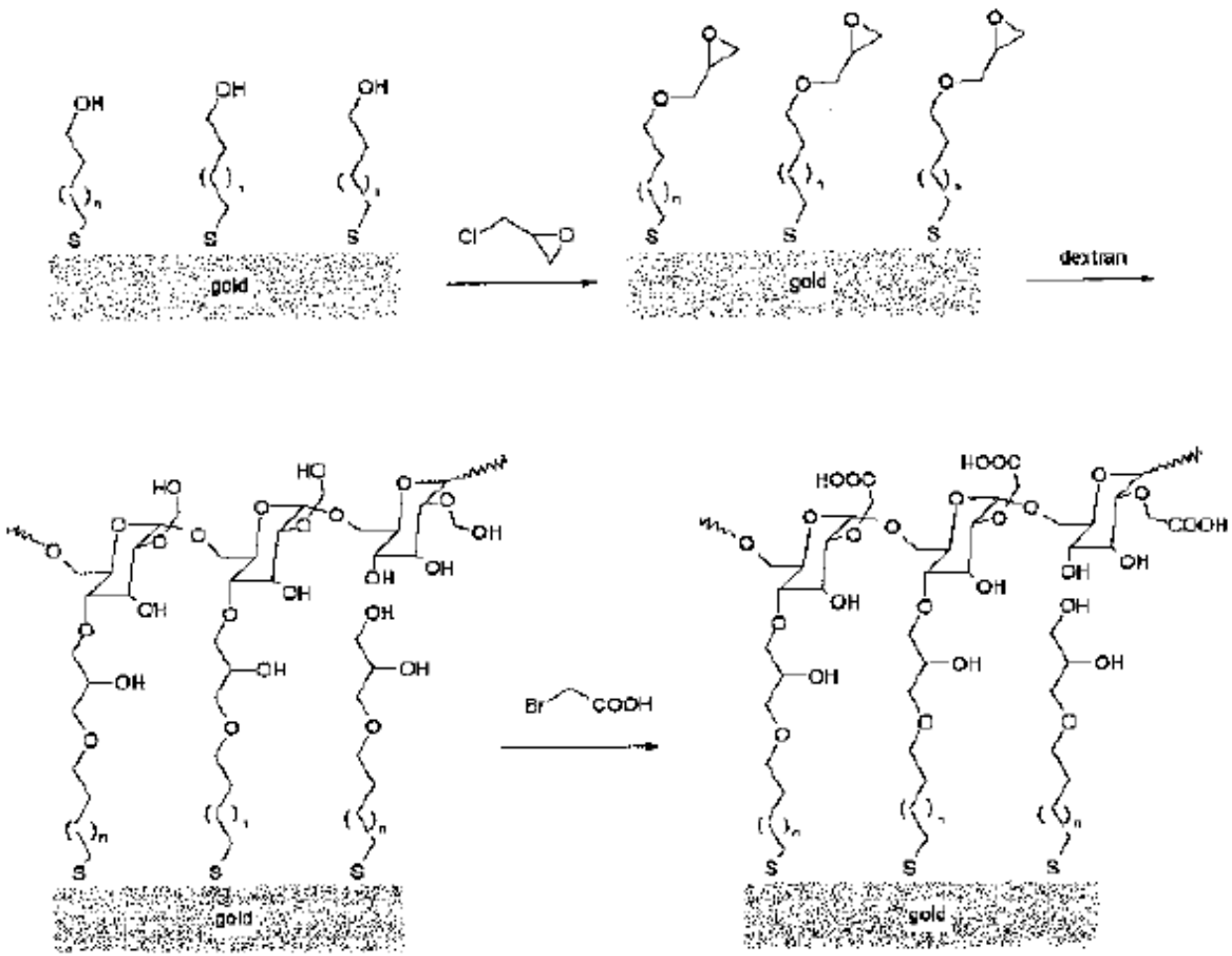

Scheme 2.4 Reaction schemes for preparing a hydrogel dextran matrix [41].

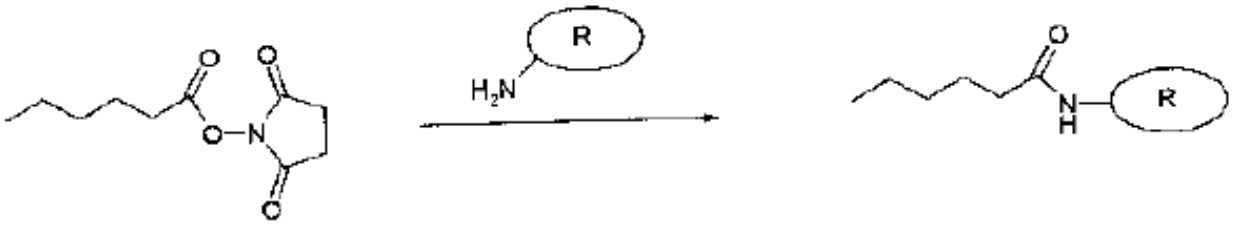

Scheme 2.6 Surface coupling reaction of NHS-esters with the amino residues of the side-chains of polypeptides (lysine units). R, protein.

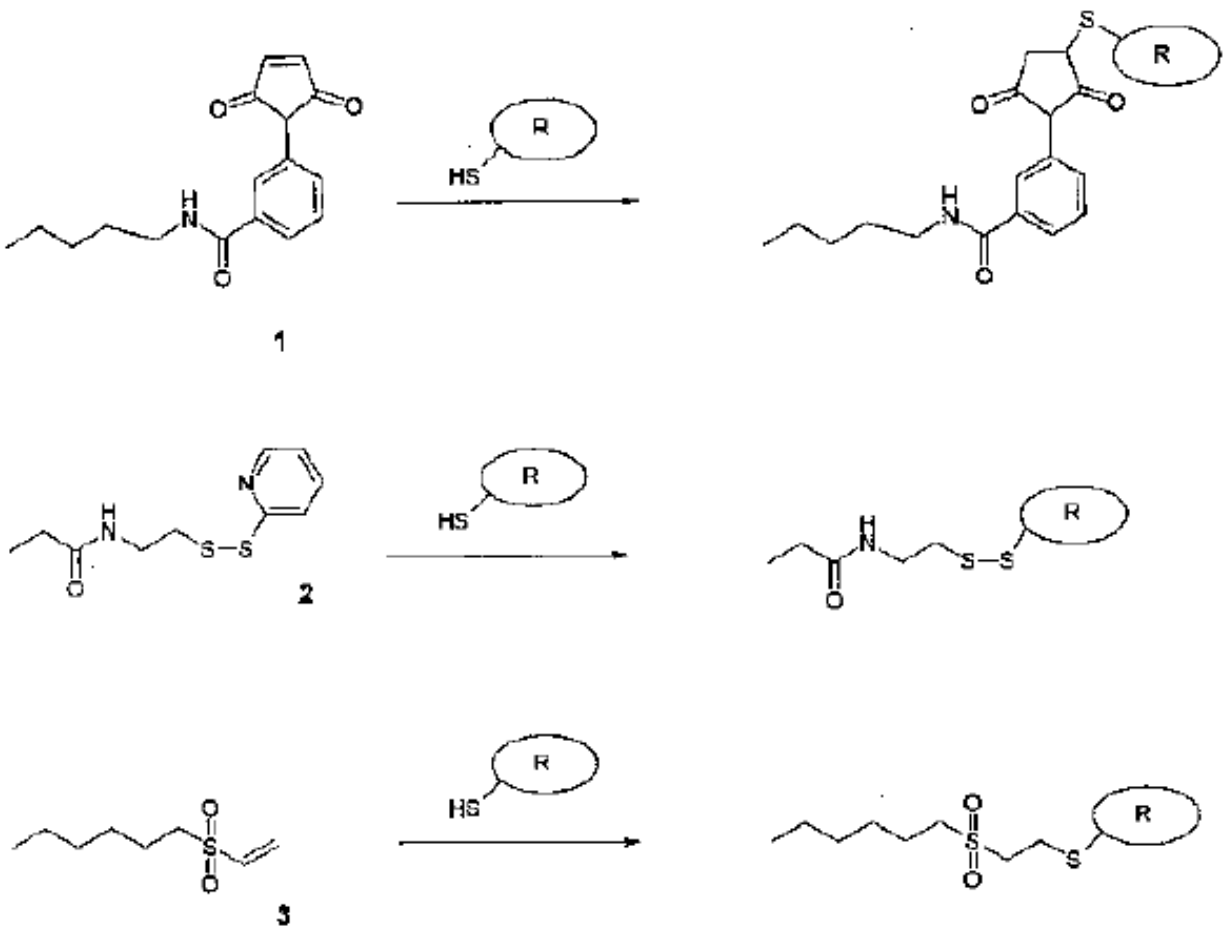

Scheme 2.7 Surface modifications for the attachment of thiol residues (which are present in the side chains) of polypeptides (cysteine units). R, protein, **1**, maleimide; **2**, disulfides; 3, vinyl sulfone.

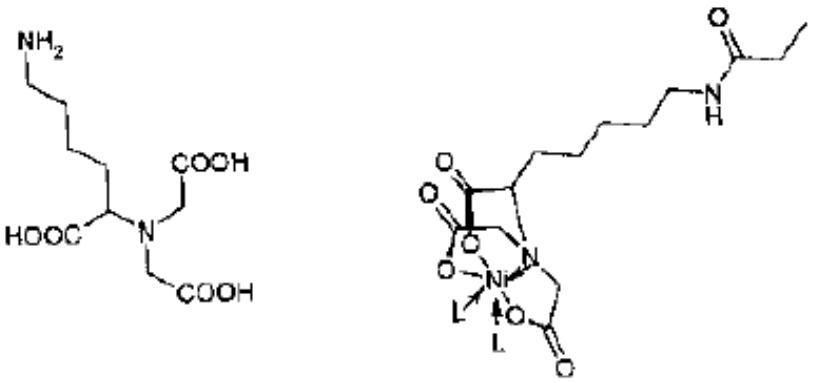

A B

Scheme 2.12 (A) Structure of N-(5-amino-1-carboxypentyl)iminodiacetic acid.
(B) The quadridentate nitrilotriacetic acid (NTA) ligand forms a complex with four binding sites on the nickel metal which is present in the center. The two remaining binding sites can be coordinated with histidine ligands (L).

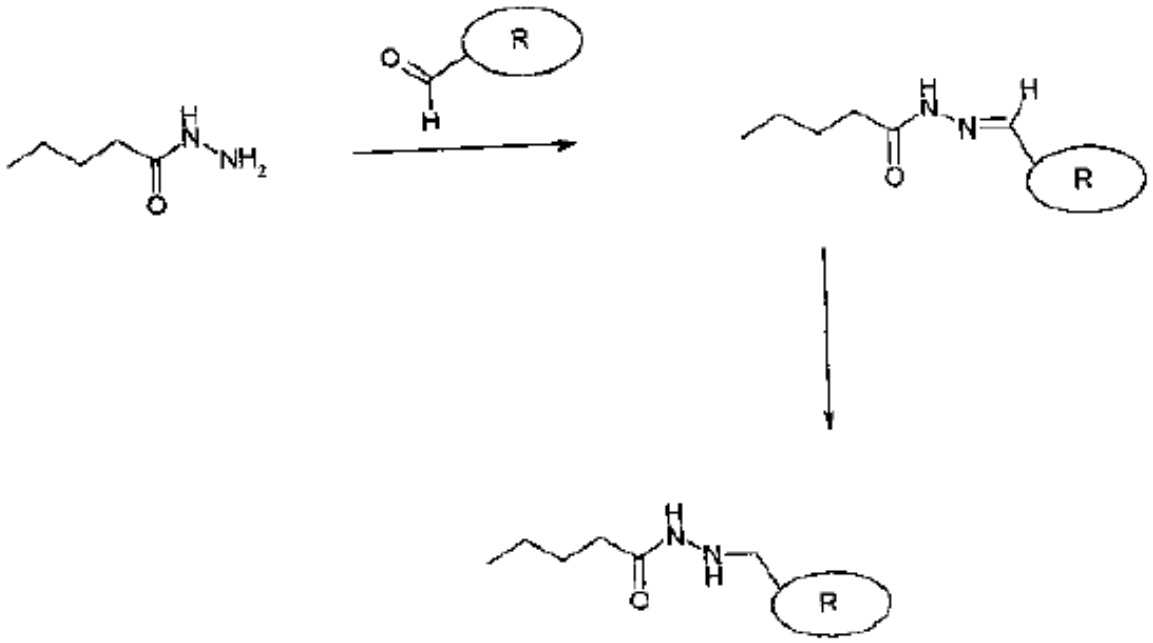

Scheme 2.13 Coupling of aldehyde residues of glycoproteins to hydrazide-terminated monolayers.

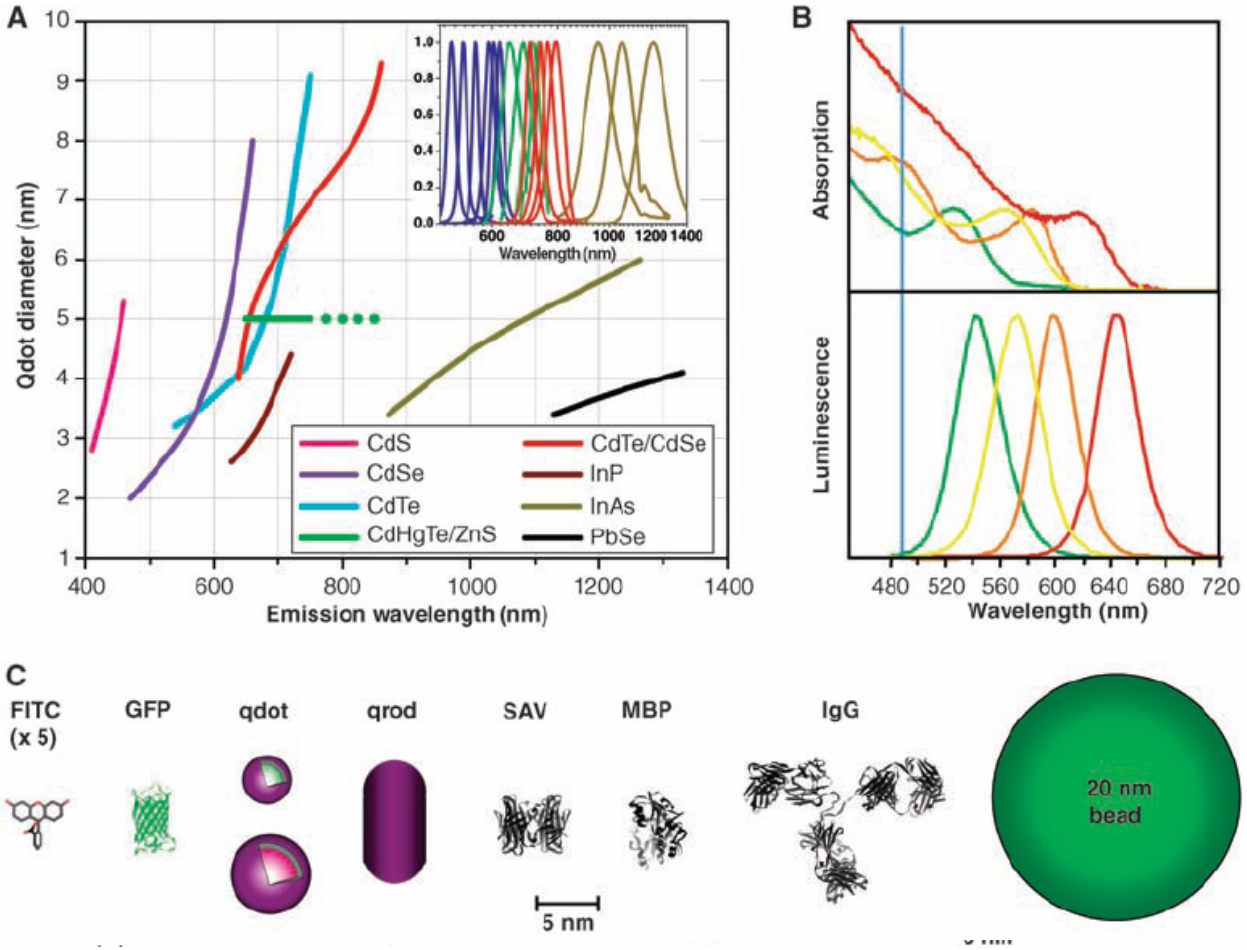

Fig. 1. (**A**) Emission maxima and sizes of quantum dots of different composition. Quantum dots can be synthesized from various types of semiconductor materials (II-VI: CdS, CdSe, CdTe…; III-V: InP, InAs…; IV-VI: PbSe…) characterized by different bulk band gap energies. The curves represent experimental data from the literature on the dependence of peak emission wavelength on qdot diameter. The range of emission wavelength is 400 to 1350 nm, with size varying from 2 to 9.5 nm (organic passivation/solubilization layer not included). All spectra are typically around 30 to 50 nm (full width at half maximum). Inset: Representative emission spectra for some materials. Data are from (*12*, *18*, *27*, *76*–*82*). Data for CdHgTe/ZnS have been extrapolated to the maximum emission wavelength obtained in our group. (**B**) Absorption (upper curves) and emission (lower curves) spectra of four CdSe/ZnS qdot samples. The blue vertical line indicates the 488-nm line of an argon-ion laser, which can be used to efficiently excite all four types of qdots simultaneously. [Adapted from (*28*)] (**C**) Size comparison of qdots and comparable objects. FITC, fluorescein isothiocyanate; GFP, green fluorescent protein; qdot, green (4 nm, top) and red (6.5 nm, bottom) CdSe/ZnS qdot; qrod, rod-shaped qdot (size from Quantum Dot Corp.'s Web site). Three proteins—streptavidin (SAV), maltose binding protein (MBP), and immunoglobulin G (IgG)—have been used for further functionalization of qdots (see text) and add to the final size of the qdot, in conjunction with the solubilization chemistry (Fig. 2).

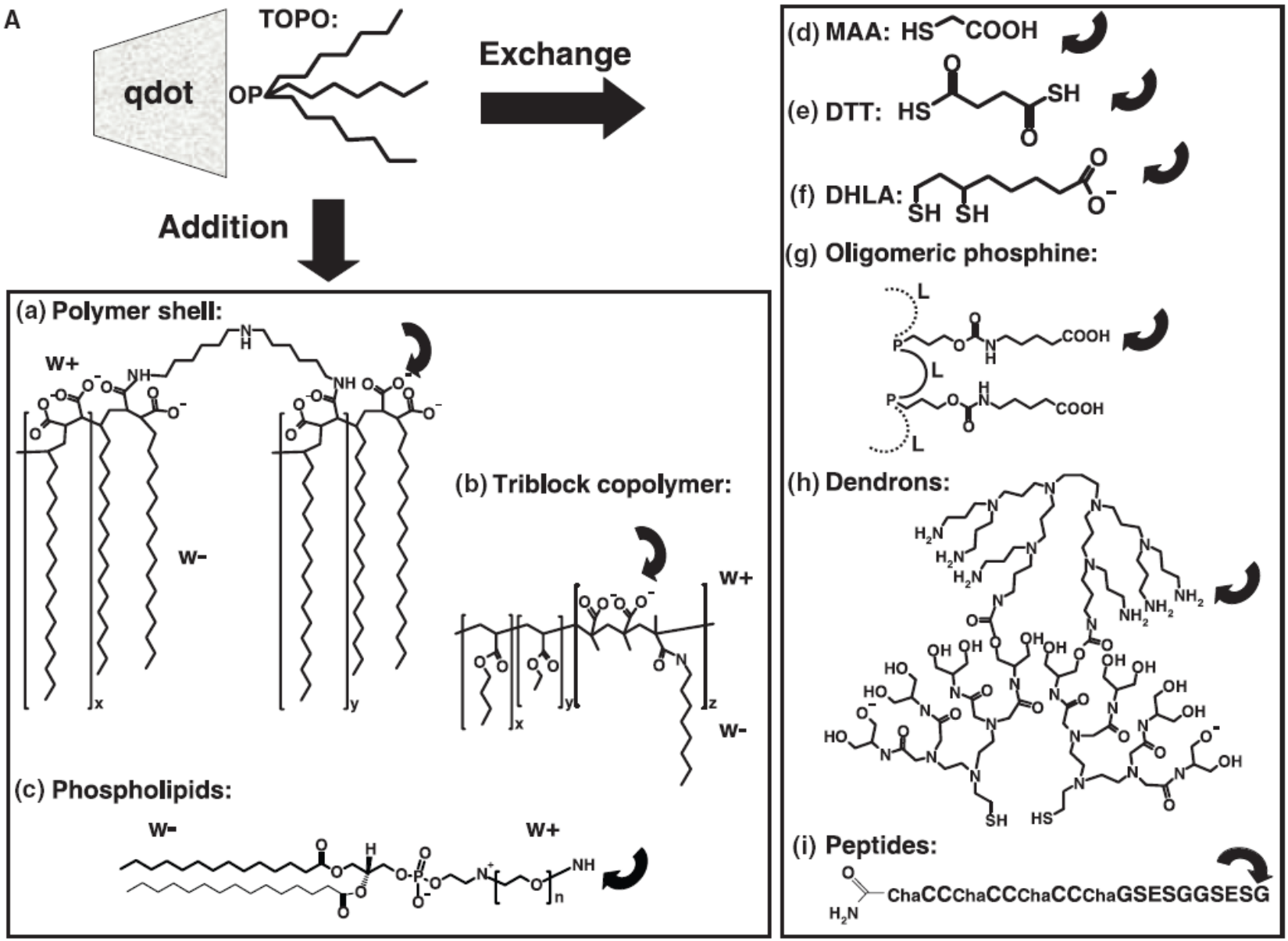
A
qdot
TOPO:
OP
Exchange
Addition
(a) Polymer shell:
W+
W-
(b) Triblock copolymer:
W+
W-
(c) Phospholipids:
W-
W+
(d) MAA: HS COOH
(e) DTT: HS SH
(f) DHLA: SH SH
(g) Oligomeric phosphine:
COOH
COOH
(h) Dendrons:
(i) Peptides:
ChaCCChaCCChaCCChaGSESGGSESG

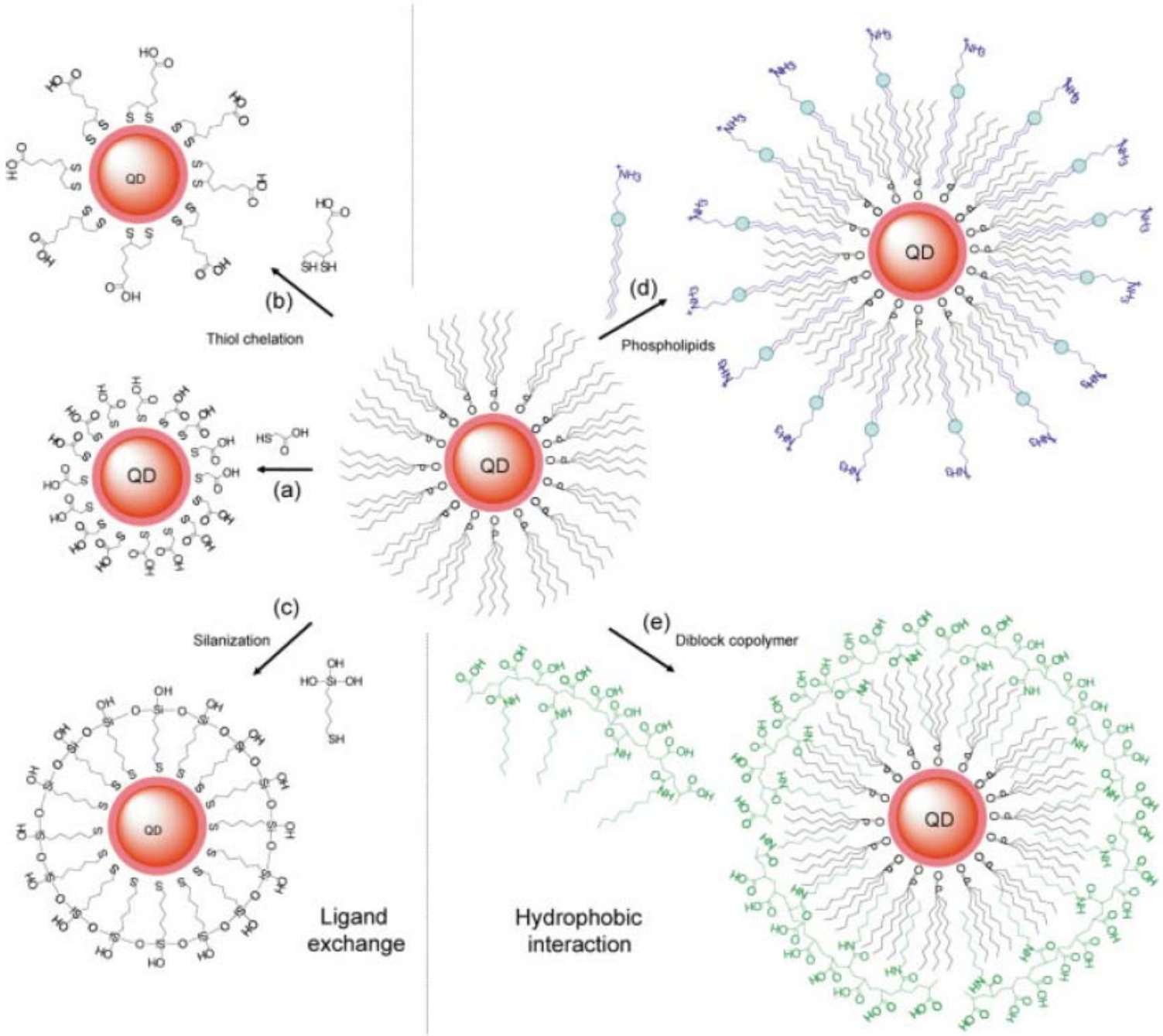
QD
(a)
(b)
Thiol chelation
(c)
Silanization
Ligand exchange
(d)
Phospholipids
(e)
Diblock copolymer
Hydrophobic interaction

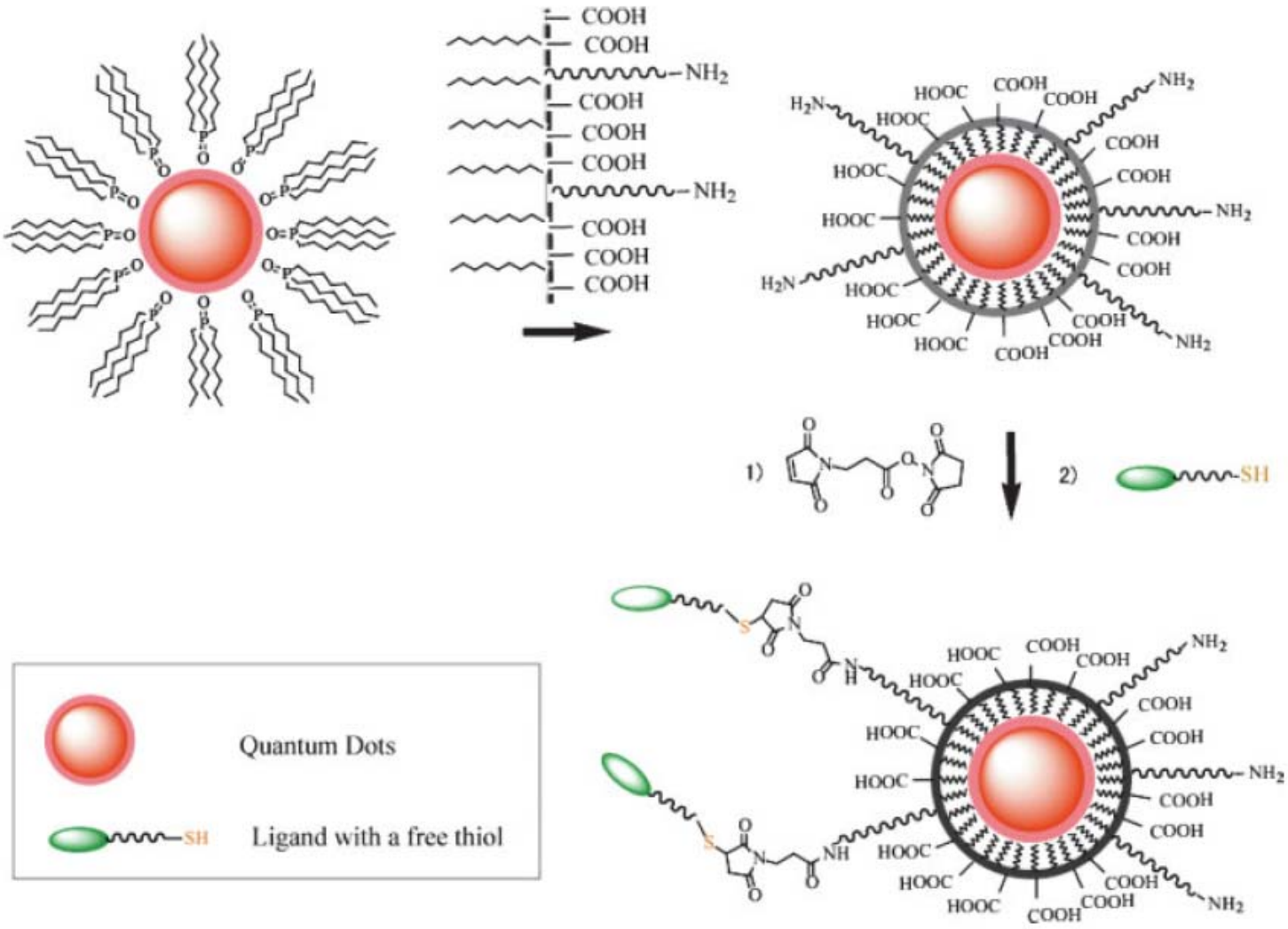

FIGURE 3 Maleimide functionalized QDs for conjugating thiol-containing ligands. TOPO stabilized QDs are coated with a primary amine functionalized tri-block amphiphilic copolymer for producing water-soluble QDs, which facilitate further conjugation to ligands with free thiols through bi-functional cross-linkers.

Cells incubated with tiopronin coated QDs

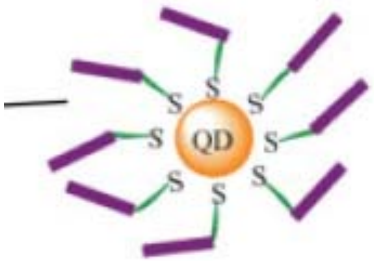

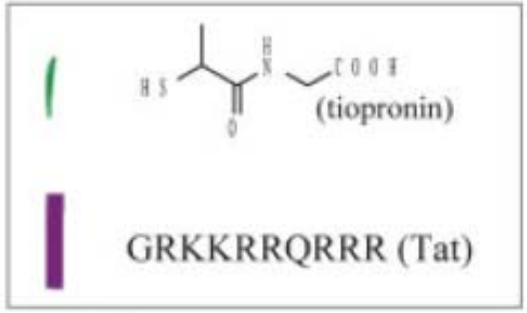

Cells incubated with Tat functionlized QDs

Scheme 1. Modular Design of Hydrophilic Ligands with Terminal Functional Groups Used in This Study

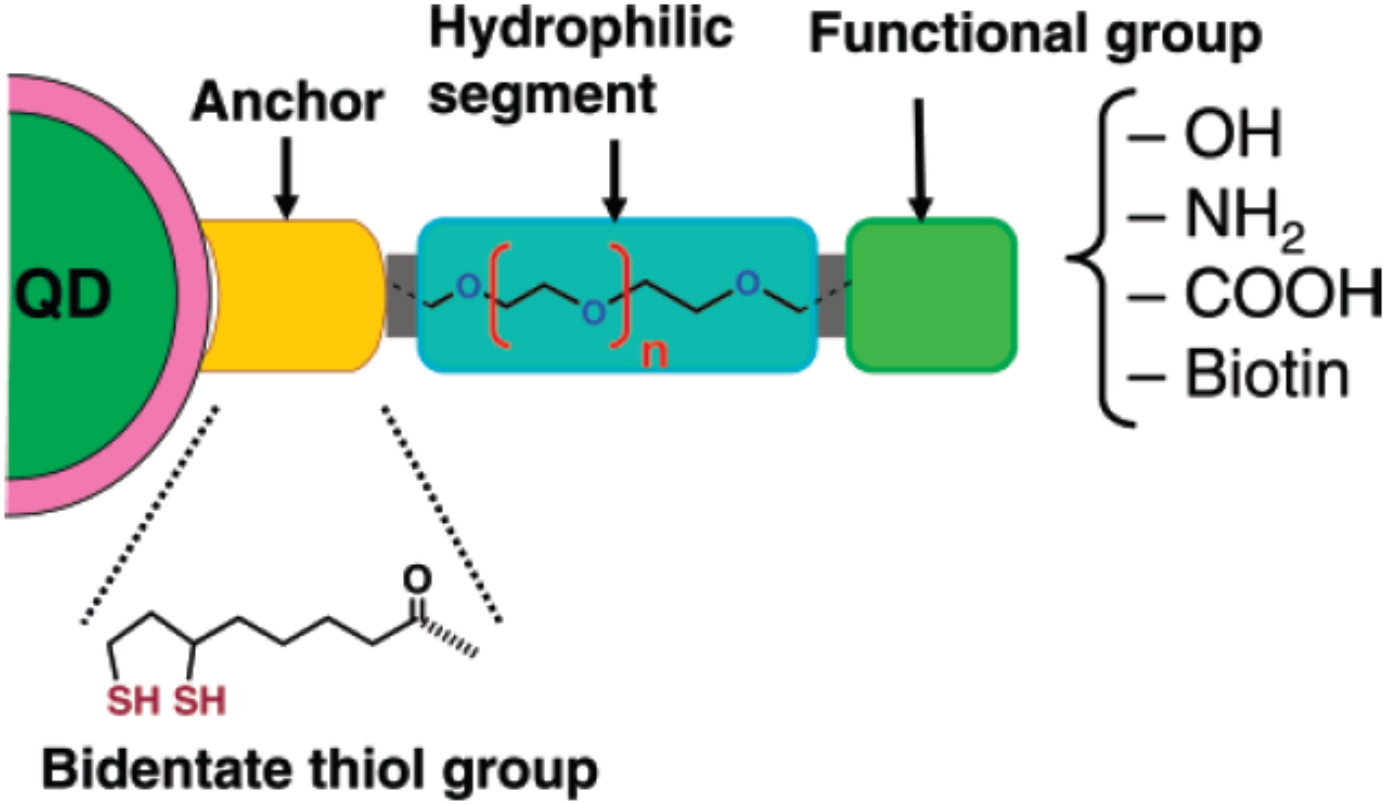

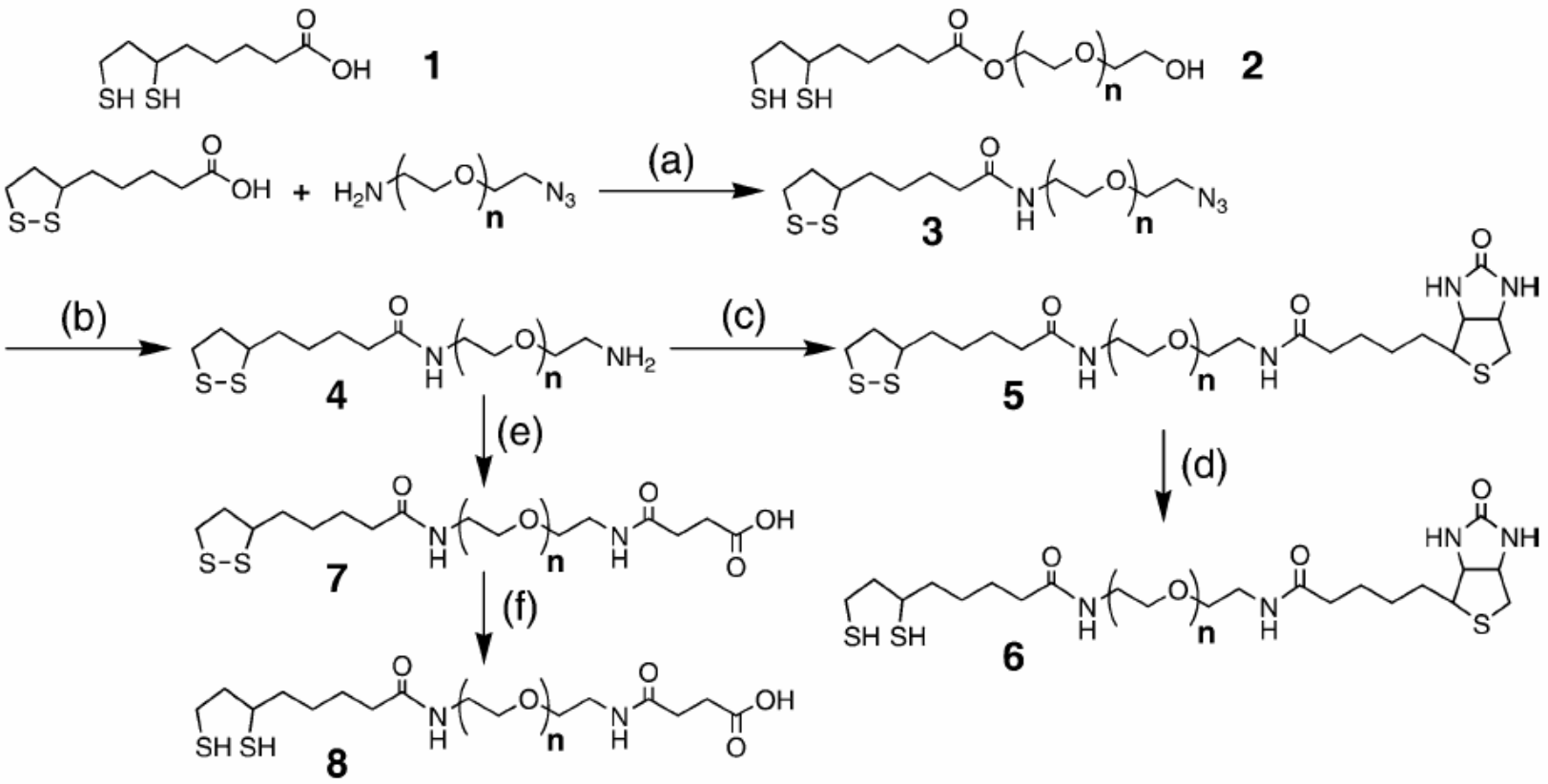

Figure 1. Chemical structures and synthetic routes of the surface ligands used in this study: (a) DCC, DMAP, CH_2Cl_2; (b) PPh_3, H_2O, THF; (c) biotin *N*-hydroxysuccinimide ester, Et_3N, DMF; (d) $NaBH_4$, EtOH, H_2O; (e) succinic anhydride, pyridine; (f) $NaBH_4$, EtOH, H_2O.

Fig. 2. Qdot solubilization and functionalization. (**A**) Surface chemistries. TOPO (trioctylphosphine oxide)–passivated qdots can be solubilized in aqueous buffer by addition of a layer of amphiphilic molecules containing hydrophilic (w+) and hydrophobic (w–) moieties, or by exchange of TOPO with molecules that have a Zn-coordinating end (usually a thiol group, SH) and a hydrophilic end. Examples of addition include (a) formation of a cross-linked polymer shell (*31*), (b) coating with a layer of amphiphilic triblock copolymer (*26*), and (c) encapsulation in phospholipid micelles (*29*). Examples of exchange include (d) mercaptoacetic acid (MAA) (*20*), (e) dithiothreitol (DTT) (*21*), (f) dihydrolipoic acid (DHLA) (*33*), (g) oligomeric phosphines (*22*), (h) cross-linked dendrons (*23*), and (i) peptides (*24*). The curved arrow indicates sites available for further functionalization. (**B**) Peptide toolkit. The light blue segment contains cysteines and hydrophobic amino acids ensuring binding to the qdot (*24*) and is common to all peptides. S, solubilization sequence; P, PEG; B, biotin; R, peptide recognition sequence; Q, quencher; D, DOTA; X, any unspecified peptide-encoded function. Qdot solubilization is obtained by a mixture of S and P. Qdots can be targeted with B, R, or other chemical moieties. Qdot fluorescence can be turned on or off by attaching a Q via a cleavable peptide link. In the presence of the appropriate enzyme, the quencher is separated from the qdot, restoring the photoluminescence and reporting on the enzyme activity. For simultaneous PET and fluorescence imaging, qdots can be rendered radioactive by D chelation of radionuclides; for simultaneous MRI and fluorescence imaging, qdots can be rendered radioactive by D chelation of nuclear spin labels.

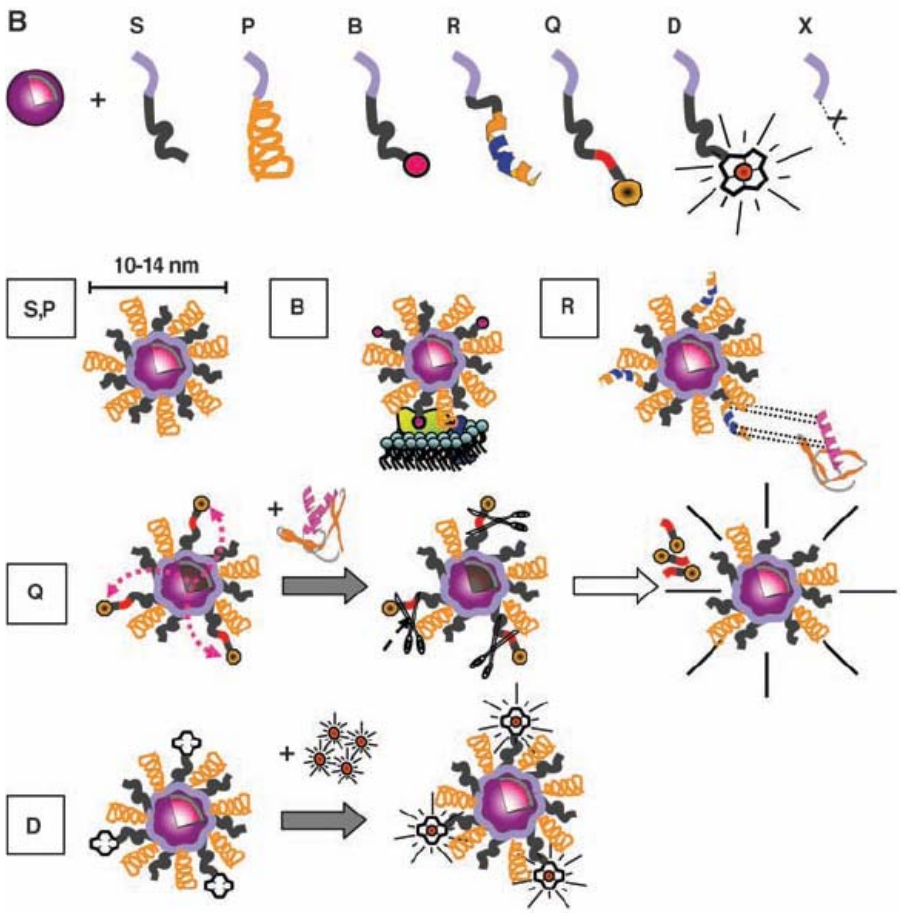

Synthesis of Nanoparticles and Surface Modifications

Synthesis of Silver Nanoparticles

1. ***A solution of $AgNO_3$ (1.0×10^{-3} M) in deionized water was heated until it began to boil.***
2. ***Sodium citrate solution was added dropwise to the silver nitrate solution as soon as the boiling commenced. The color of the solution slowly turned into grayish yellow, indicating the reduction of the Ag+ ions.***
3. ***Heating was continued for an additional 15 min, and then the solution was cooled to room temperature before employing for further experimentation.***

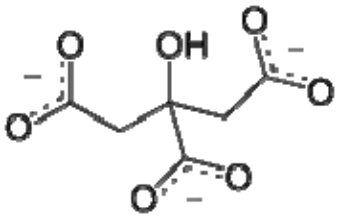

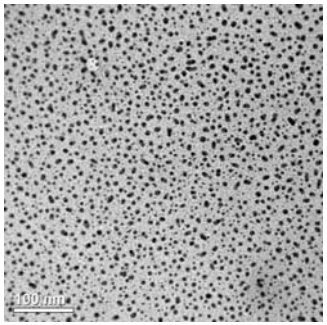

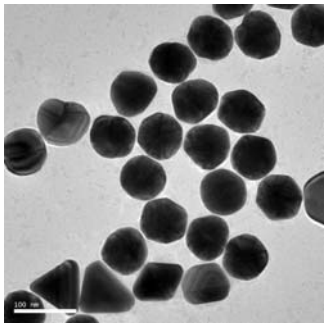

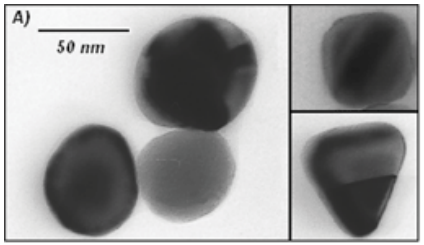

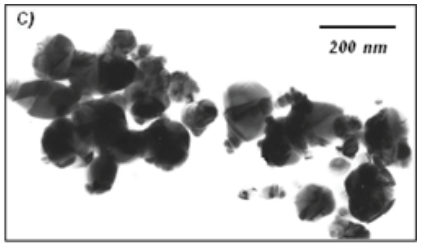

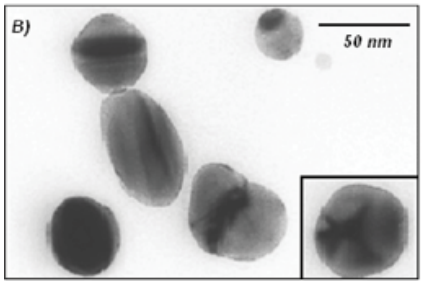

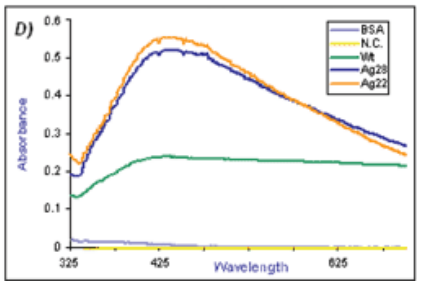

Synthesis of Gold Nanoparticles

1. ***Add 20 mL of 1.0 mM $HAuCl_4$ to a 50 mL round bottom flask on a stirring hot plate.***
2. ***Add a magnetic stir bar and bring the solution to a boil.***
3. ***To the boiling solution, add 2 mL of a 1% solution of trisodium citrate dihydrate***
4. ***The gold sol gradually forms as the citrate reduces the gold(III). Stop heating when a deep red color is obtained.***

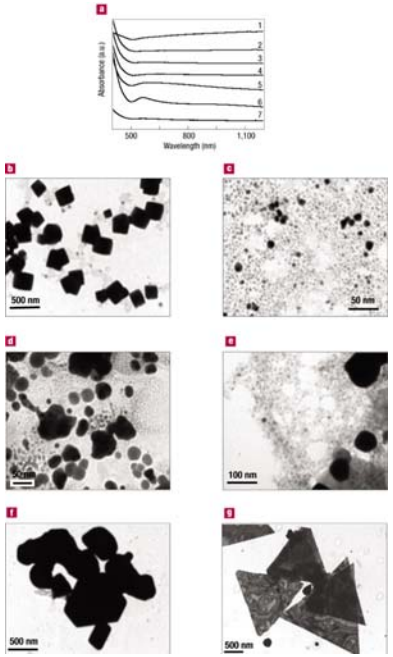

(1) $$M_xO_y \xrightarrow[(\text{medium})\ \Delta_T]{\text{Reducing Agent}} M_n + H_2O$$

(Reducing Agent = R - COH)

(2) $$M(L)_x \xrightarrow[(\text{medium})\ \Delta_T]{\text{Reducing Agent}} M_n + L^-$$

($L=NO_3^-, C_2H_5O^-$)

(Reducing Agent = R - COH)

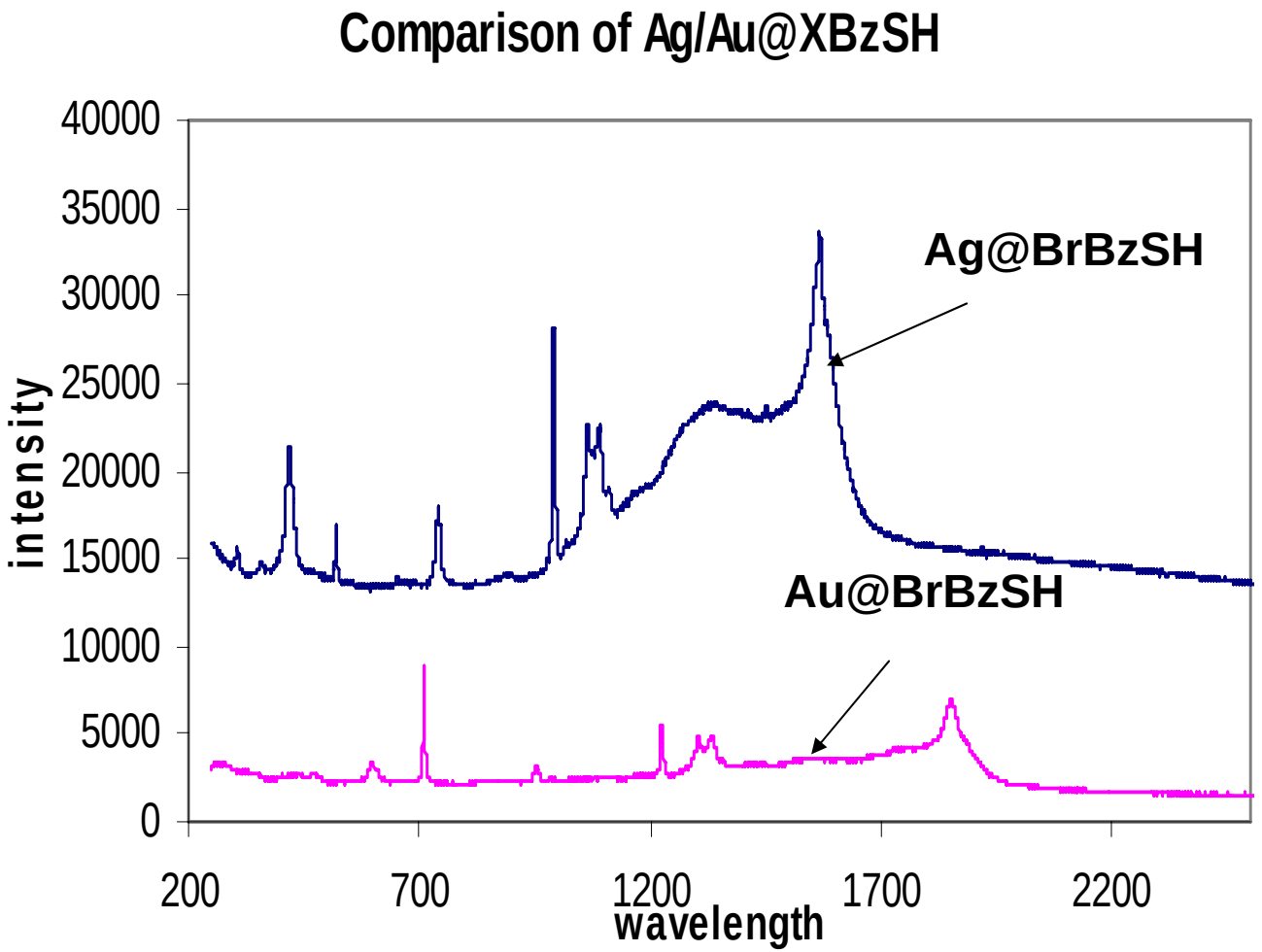
Comparison of Ag/Au@XBzSH
40000
35000
30000
25000
20000
15000
10000
5000
0
intensity
200
700
1200
1700
2200
wavelength
Ag@BrBzSH
Au@BrBzSH

Construction of Core Shell Ag/Au@SiO_2 Nanoparticles

1. *Under vigorous stirring, 1 ml of the silver/ gold colloids solution was mixed with 250 mL of isopropanol and 25 mL of deionized water.*
2. *Immediately after the addition of 4 mL of 30% ammonium hydroxide, different amounts of tetraethoxysilane (TEOS) were added to the reaction mixture.*
3. *To obtain different silica layer thicknesses, TEOS solutions with a concentration between 50% and 100% was added to the suspension. The reaction was stirred at room temperature for 30 minutes and then was allowed to age without agitation at 4 ℃ overnight.*
4. *Each suspension of silica-coated silver/gold nanoparticles was washed and centrifuged, followed by re-suspension in water. The thickness of the silica layers was determined from TEM images .*

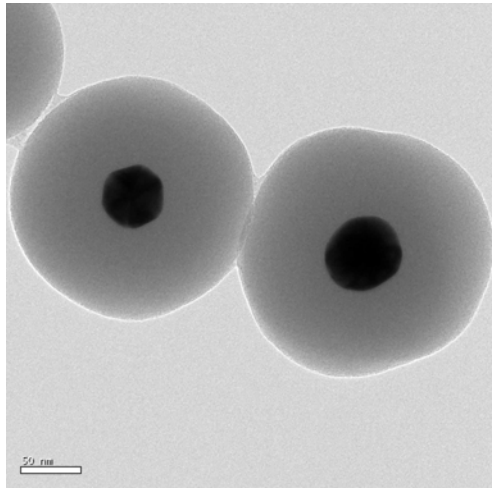

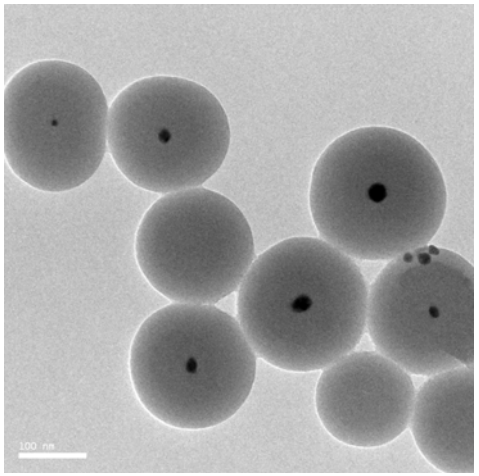

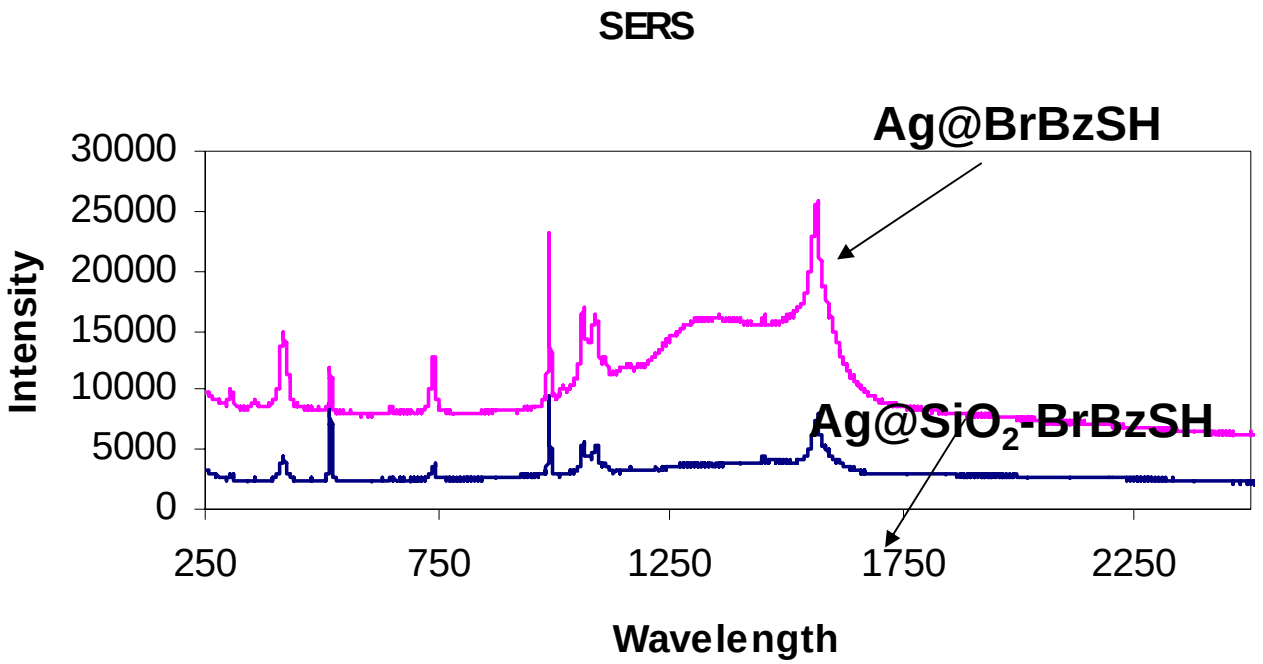
SERS
Ag@BrBzSH
Ag@SiO2-BrBzSH
Intensity
30000
25000
20000
15000
10000
5000
0
250
750
1250
1750
2250
Wavelength

Core-Shell Nanoparticles

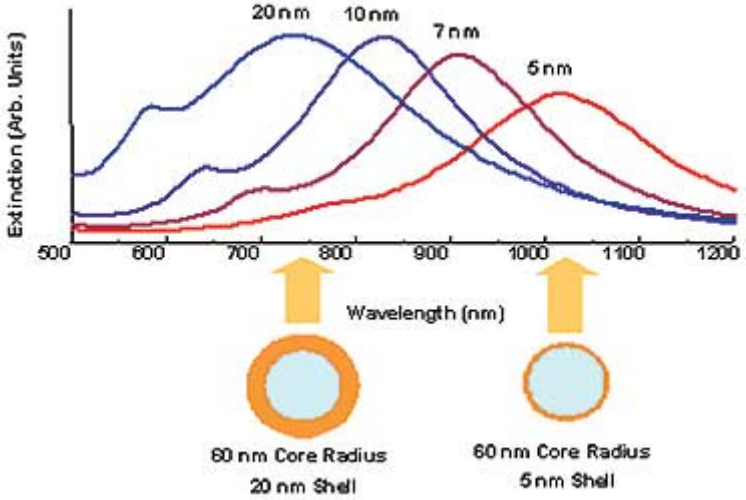

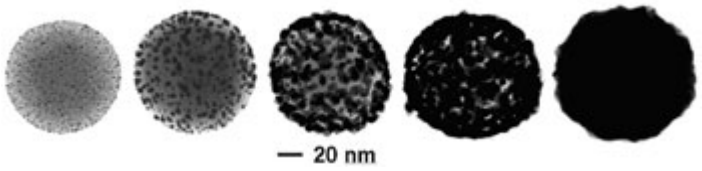

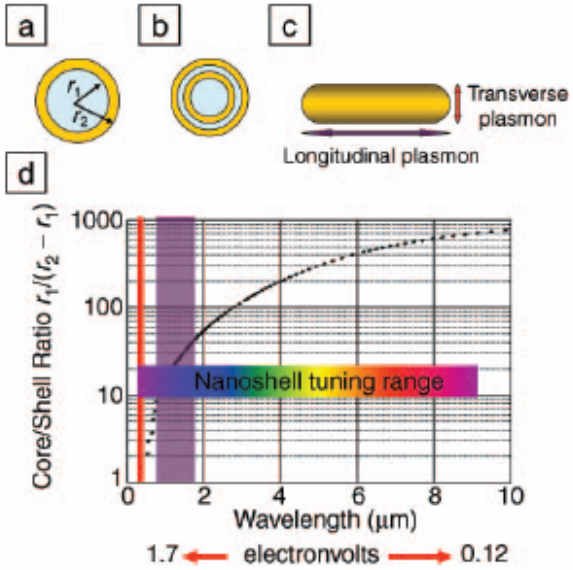

Figure 1. (a) Schematic illustration of a silica-core, gold-shell nanoshell, indicating inner (r_1) and outer (r_2) radii of the shell layers. (b) Depiction of a four-layer, concentric nanoshell. (c) Schematic illustration of a metallic nanorod. (d) Plot of nanoshell resonance as a function of core and shell dimensions, overlaid with reported spectral ranges of nanorod resonances (red, transverse plasmon; purple, longitudinal plasmon), and reported nanoshell and concentric nanoshell combined spectral range of plasmon response.

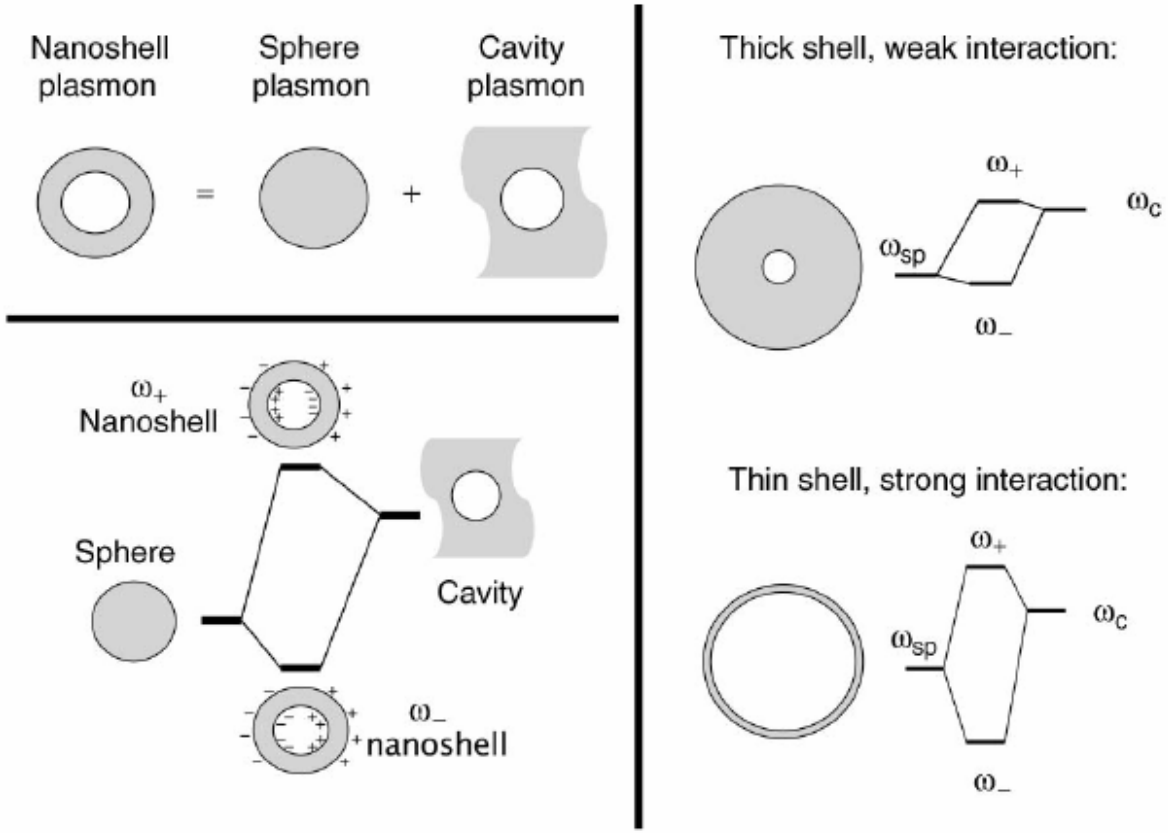

Figure 2. Plasmon hybridization and the sphere–cavity model for nanoshells: the interaction between a sphere (resonance frequency, ω_{sp}) and a cavity plasmon (resonance frequency, ω_c) is tuned by varying the thickness of the shell layer of the nanoparticle. Two hybrid plasmon resonances, the ω_- "bright," or "bonding," plasmon and the ω_+ "dark," or "anti-bonding," plasmon resonances are formed. The lower-energy plasmon couples most strongly to the optical field.

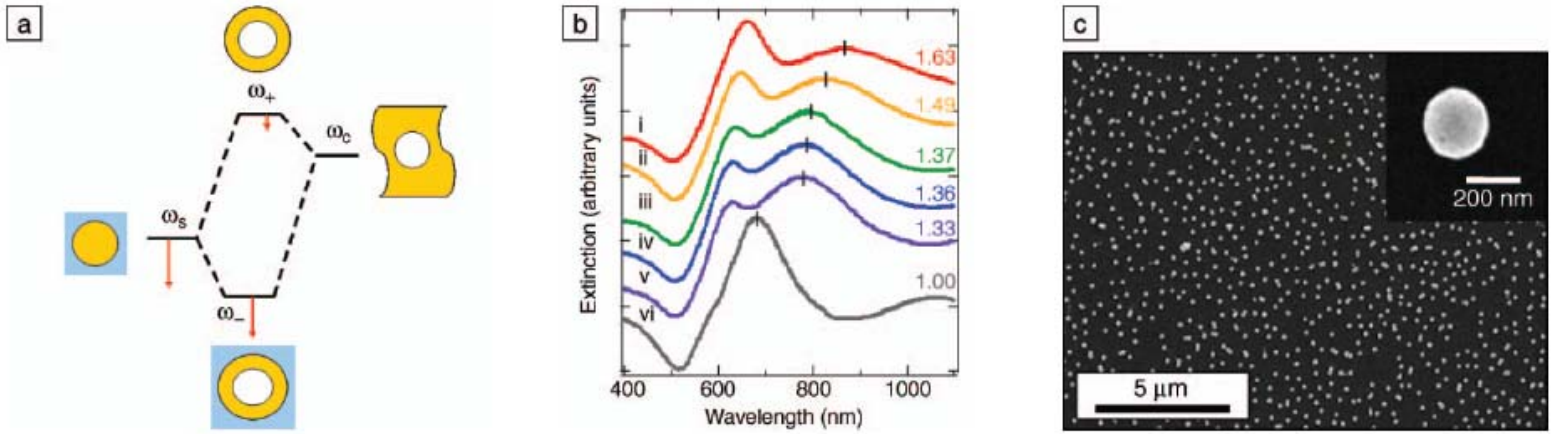

Figure 5. (a) Plasmon hybridization picture applied to surface plasmon resonance sensing with nanoshells: the low-energy "bonding" plasmon, ω_-, is sensitized to changes in its dielectric environment. The blue background schematically denotes the embedding medium for the nanoparticle. (b) Experimental curves showing plasmon resonance shifts for nanoshell-coated films in various media: (i) carbon disulfide, (ii) toluene, (iii) hexane, (iv) ethanol, (v) H_2O, and (vi) air. The index of refraction for each embedding medium is noted on the far right of the spectra. Spectra are offset for clarity. (c) Scanning electron micrograph of nanoshells deposited onto a poly(vinyl pyridine) functionalized glass surface, as used to acquire data in (b). Inset: individual nanoshell.

Preparation of Fe_3O_4@Ag/Au

1. *To the magnetic nanoparticle suspension obtained from commercial company, add 50 ml of a solution of Au (III) salt or Ag (I) salt at concentration of 0.01–1% mmol/L , shaking for 30 minutes, allowing Au (III) or Ag (I) ion to absorb on the surface of magnetic nanoparticle sufficiently,*
2. *Then adding 15–40 ml of reducing agent, such as hydroxylamine hydrochloride at concentration of 40 mmol/L, reacting for 5–40 minutes.*
3. *Further adding 1–10 ml of a solution of Au (III) salt or Ag (I) salt at concentration of 0.01–1%, shaking for 10 minutes, coating a reduced layer of gold or silver on the surface of the magnetic nanoparticle, forming super-paramagnetic composite particles having core/shell structure, separating magnetically, washing repeatedly with distilled water.*

.

Nanorods

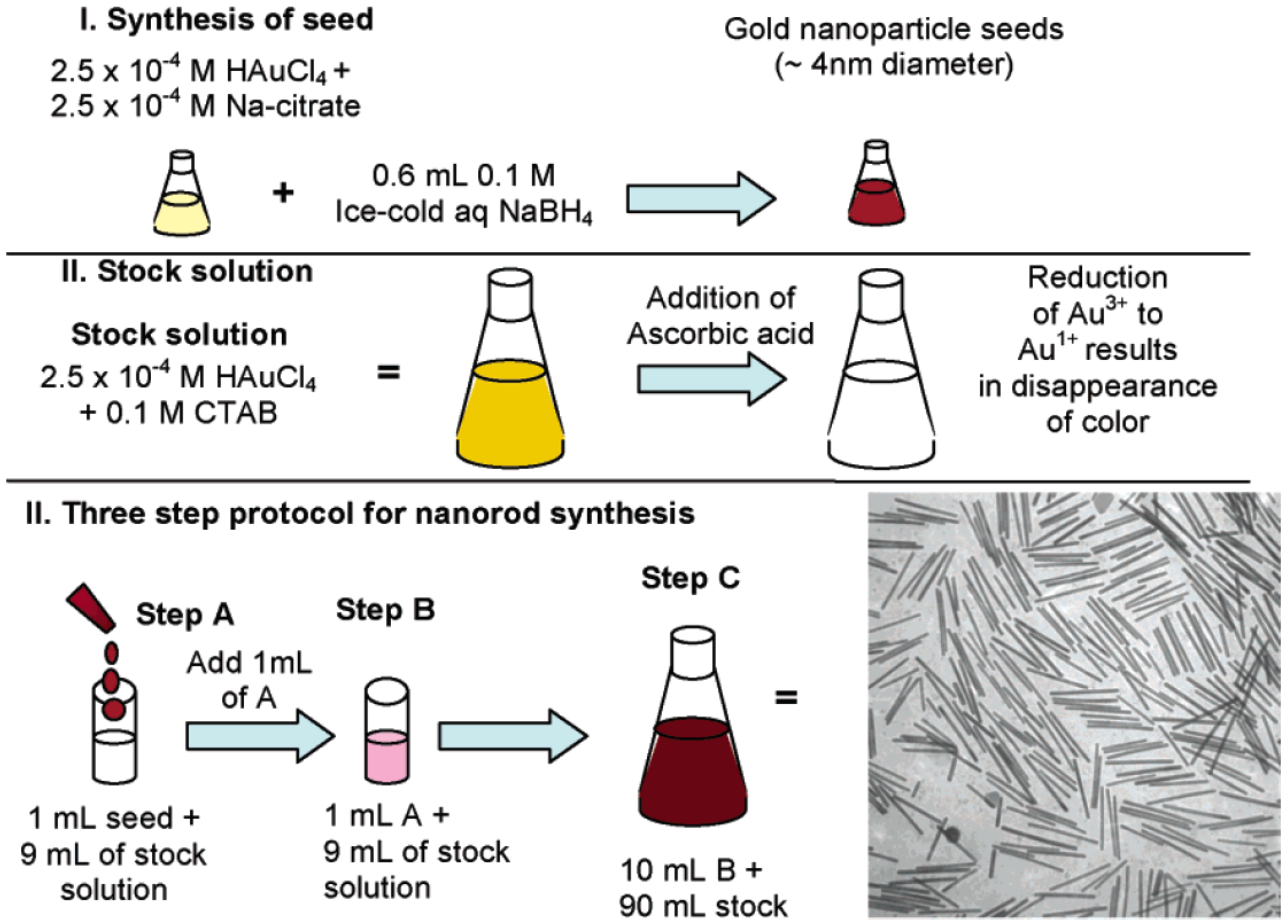

Figure 2. Seed-mediated growth approach to making gold and silver nanorods of controlled aspect ratio. The specific conditions shown here, for 20 mL volume of seed solution, lead to high-aspect ratio gold nanorods. (bottom right) Transmission electron micrograph of gold nanorods that are an average of 500 nm long.

J. Phys. Chem. B **2005,** *109,* 13857−13870

Directional Growth

Cetrimonium bromide ($(C_{16}H_{33})N(CH_3)_3Br$) (CTAB)

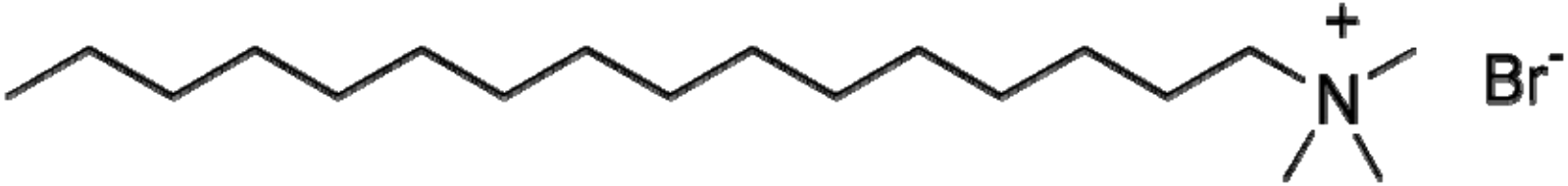

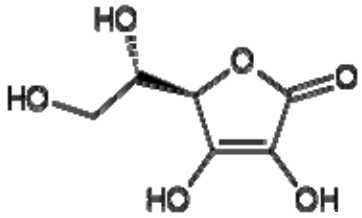

Ascorbic acid

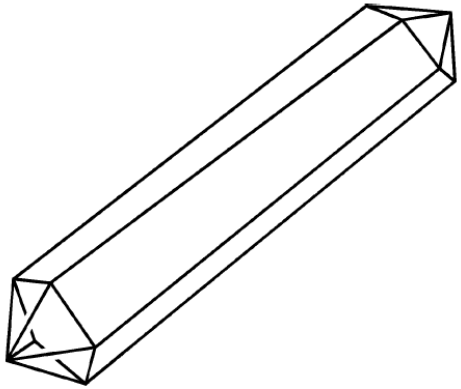

Figure 5. Cartoon of the crystallography of gold nanorods. The direction of elongation is [110]. The cross-sectional view is a pentagon; each end of the rod is capped with five triangular faces that are Au{111}. The sides of the rods are not as well-defined; either Au{100} or Au{110} faces, or both.

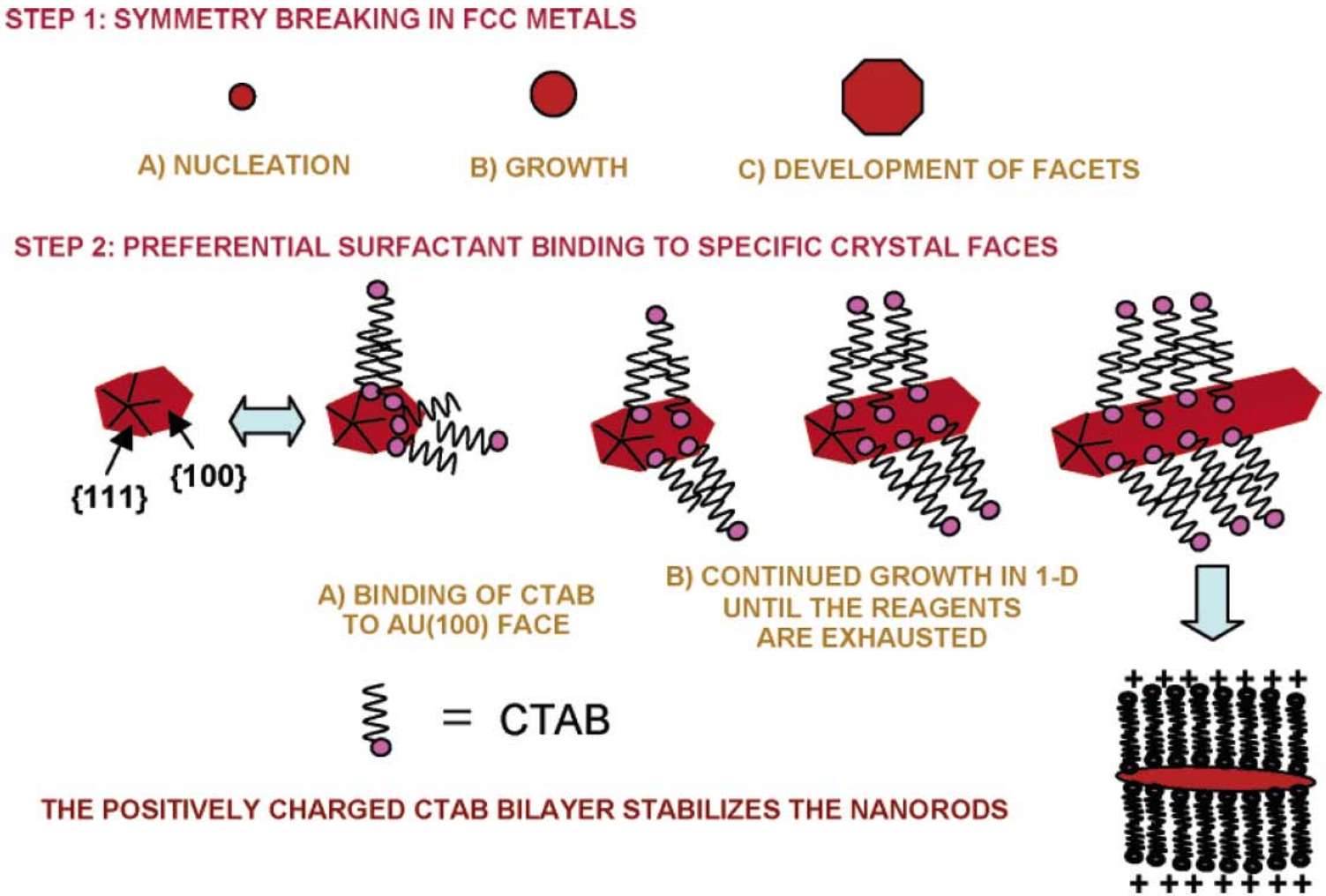

Figure 8. Proposed mechanism of surfactant-directed metal nanorod growth. The single crystalline seed particles have facets that are differentially blocked by surfactant (or an initial halide layer that then electrostatically attracts the cationic surfactant). Subsequent addition of metal ions and weak reducing agent lead to metallic growth at the exposed particle faces. In this example, the pentatetrahedral twin formation leads to Au {111} faces that are on the ends of the nanorods, leaving less stable faces of gold as the side faces, which are bound by the surfactant bilayer.

Nanorods

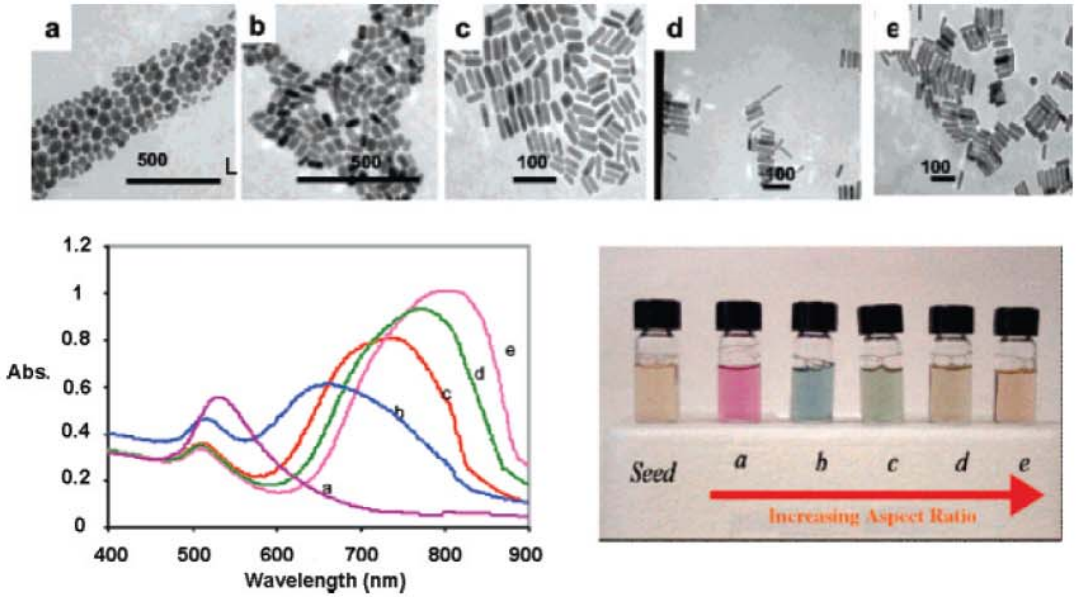

Figure 3. Transmission electron micrographs (top), optical spectra (left), and photographs (right) of aqueous solutions of Au nanorods of various aspect ratios. The seed sample has an aspect ratio of 1. Samples a, b, c, d, and e have aspect ratios of 1.35 ± 0.32, 1.95 ± 0.34, 3.06 ± 0.28, 3.50 ± 0.29, and 4.42 ± 0.23, respectively. Scale bars: 500 nm for a and b, 100 nm for c−e. Reprinted with permission from ref 16. Copyright 2005 American Chemical Society.

Nanocube and Nanorice

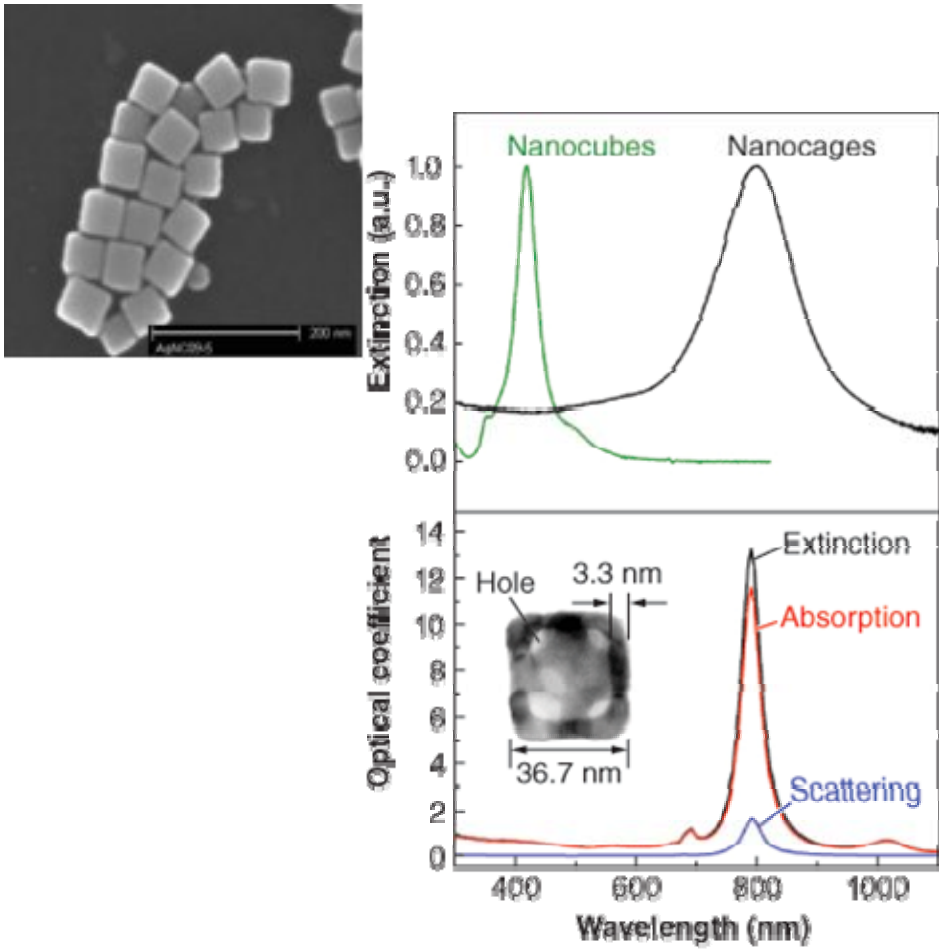

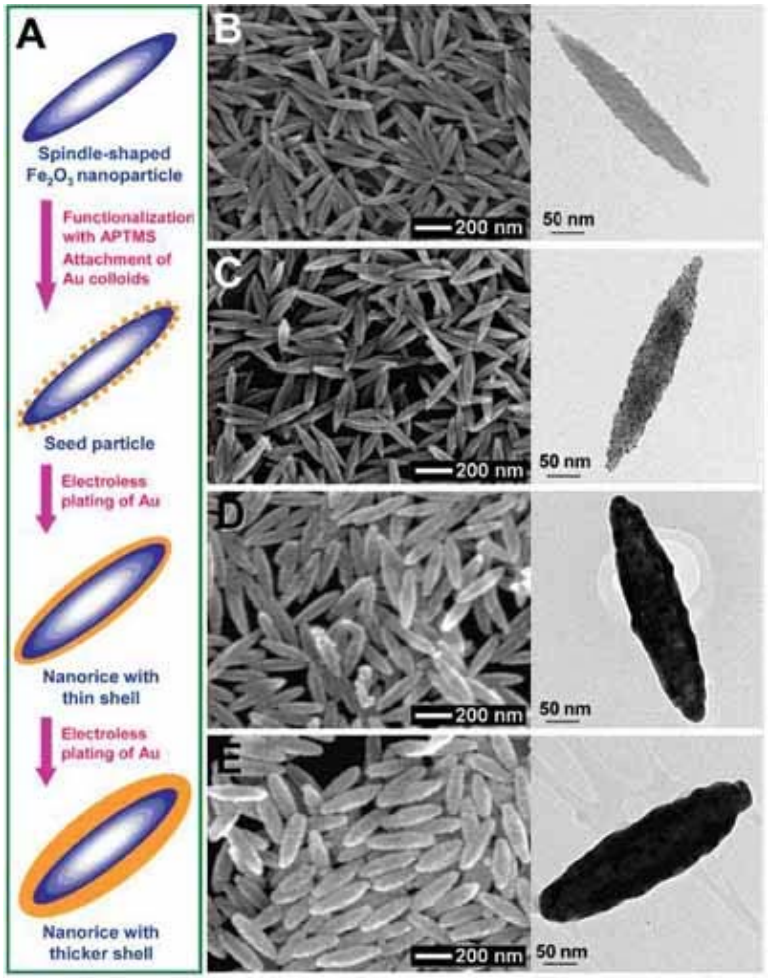

The graphic above depicts various magnitudes of nanorice, which is a rice-shaped nanoparticle with a non-conducting core made of iron oxide and covered by a metallic shell made of gold. Scientists plan to attach the nanorice to scanning probe microscopes to obtain very clear image quality that surpasses today's technology. For the Air Force, this technology could be used as a tool to develop new high-speed optoelectronic materials and to monitor chemical reactions. (Graphic provided by Prof. Naomi Halas)

Synthesis of CdSe Quantum Dots

Synthesis of TOPO/HDA capped quantum dots of CdSe

Cadmium acetate (0.107g, 0.4mmol) and oleic acid (0.27mL, 0.4mmol) in 1:2 ratio were placed in a two neck flask degassed and refilled with nitrogen, stirred at 120-130 ^{0}C under nitrogen atmosphere for 2-3 hours, obtained a clear light yellow solution. Then a mixture of capping reagent i.e. 6g of hexadecylamine (HDA) and 6g of tri-octylphosphine oxide (TOPO) prepared in separate flask was added at the same temperature and stirring was done for another 30min at temperature ~ 350 ^{0}C. The temperature was reduced and TOPSe was added at different temperatures at 250 ^{0}C through syringe immediately the color of reaction mixture became dark brown (TOPSe was prepared simultaneously in a separate vessel, appropriate quantity of Se (0.032g) powder was heated in 2mL tri-octyl phosphine (TOP) at 70-90 ^{0}C for about an hour to get a clear solution of TOPSe), stirring was continued for another 30min aliquots were taken from the reaction solution to monitor the reaction. The temperature of the reaction was reduced the stirring was done for another 1-2 hours. 50mL toluene was added before the cooling the reaction to prevent the solidification of TOPO and HDA. It was centrifuged at 3000rpm for 15min, a pallet was discarded, the supernatant solution was treated with the methanol for precipitation of CdSe nano-crystals, centrifuged at 7000rpm washed with methanol (3 x 6mL) to get product. A red residue was obtained which was re-dispersed in toluene.

Synthesis of CdSe Quantum dots

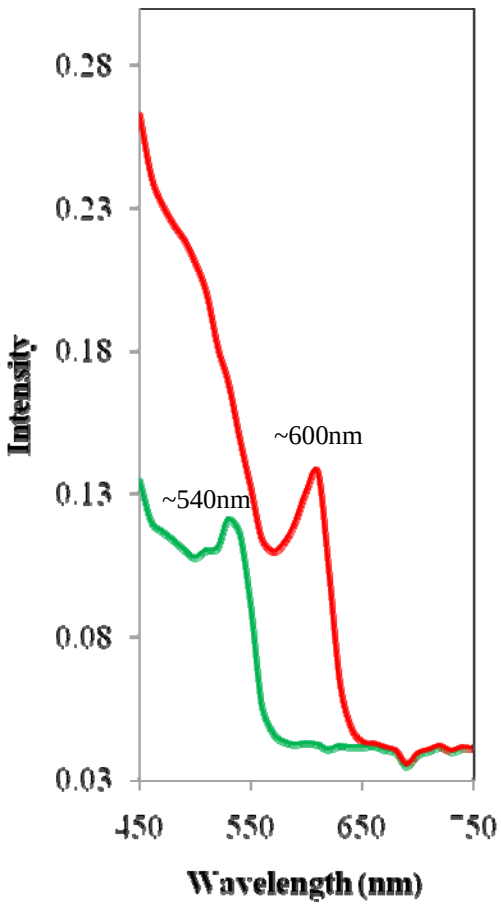

FWHM= ~28nm ± 2

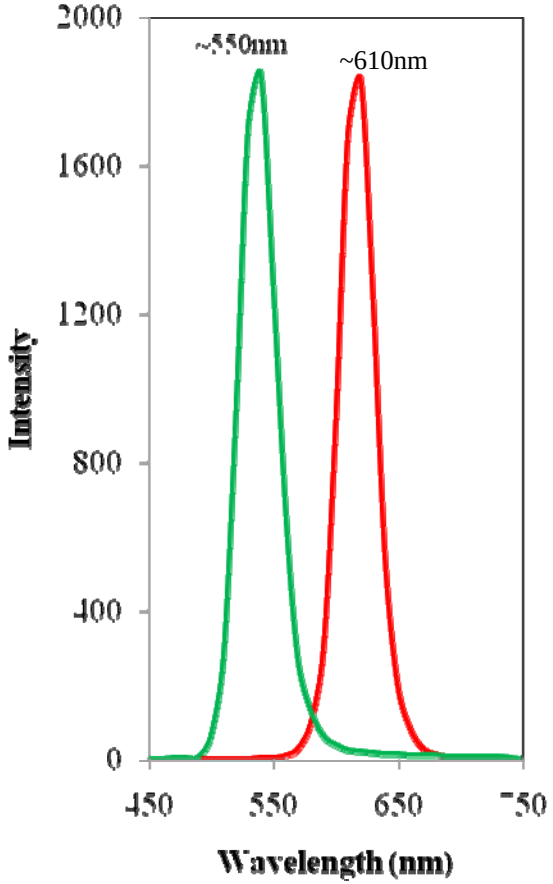

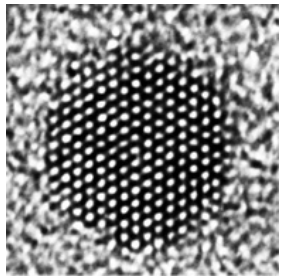

Cooperative UV and PL spectra of CdSe core

Synthesis of CdSe/ZnS Quantum Dots

20mL (31mg, 0.16 mmol) colloidal solution of CdSe QDs from stock solution (54mg dissolved in 35mL toluene) was placed in a two-neck flask. TOPO (6g) and HAD (6g) were added and then toluene was removed through vacuum, flask refilled with nitrogen. The reaction mixture was heated at 350 ^{0}C for two hours. In another flask zinc acetate in 1:3 ratio with respect of CdSe and was dissolved in 4mL of oleic acid stirred at 120 ^{0}C for 2 hours obtained a light yellow coloured solution and temperature reduced to 60-70 ^{0}C. After cooling to room temperature, TOPSe was mixed with Zn salt solution. And the mixture was injected slowly through syringe in to reaction solution of CdSe-TOPO at 180-200 ^{0}C. The stirring was done for another an hour. The similar procedure was followed for work up of reaction as avobe experiment. The final product was re-dispersed in toluene.

Light emission from CdSe/ZnSe Quantum dots

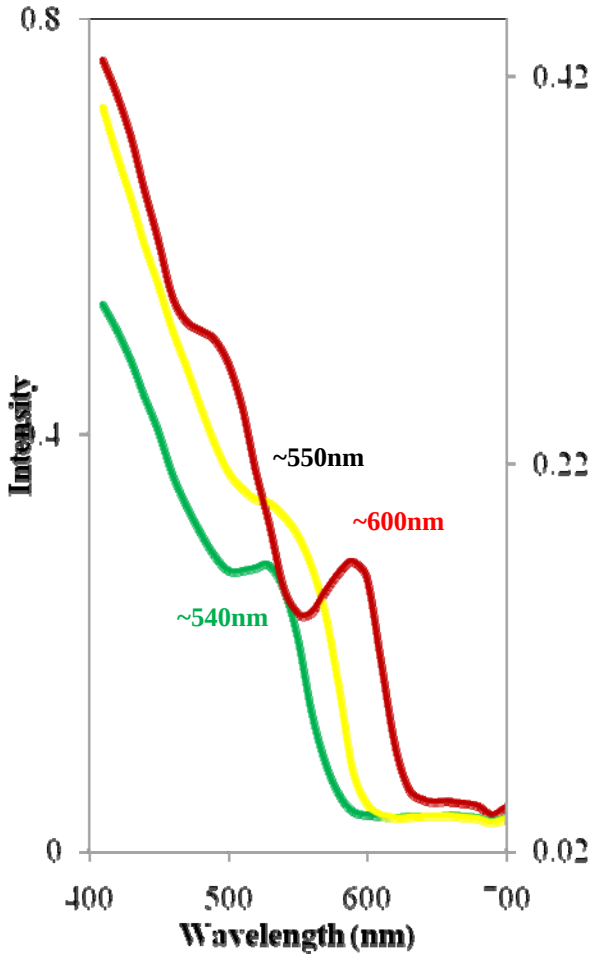

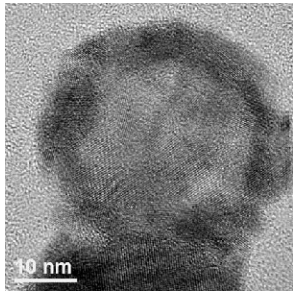

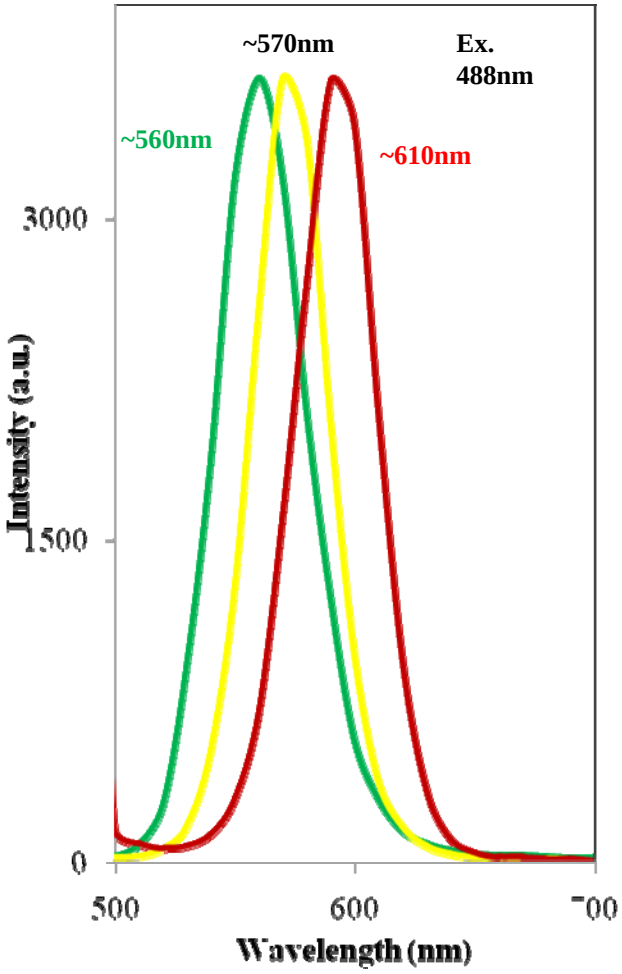

UV-Visible and PL spectra of CdSe/ZnSe re-dispersed in toluene

Carboxyl Presenting Surfaces

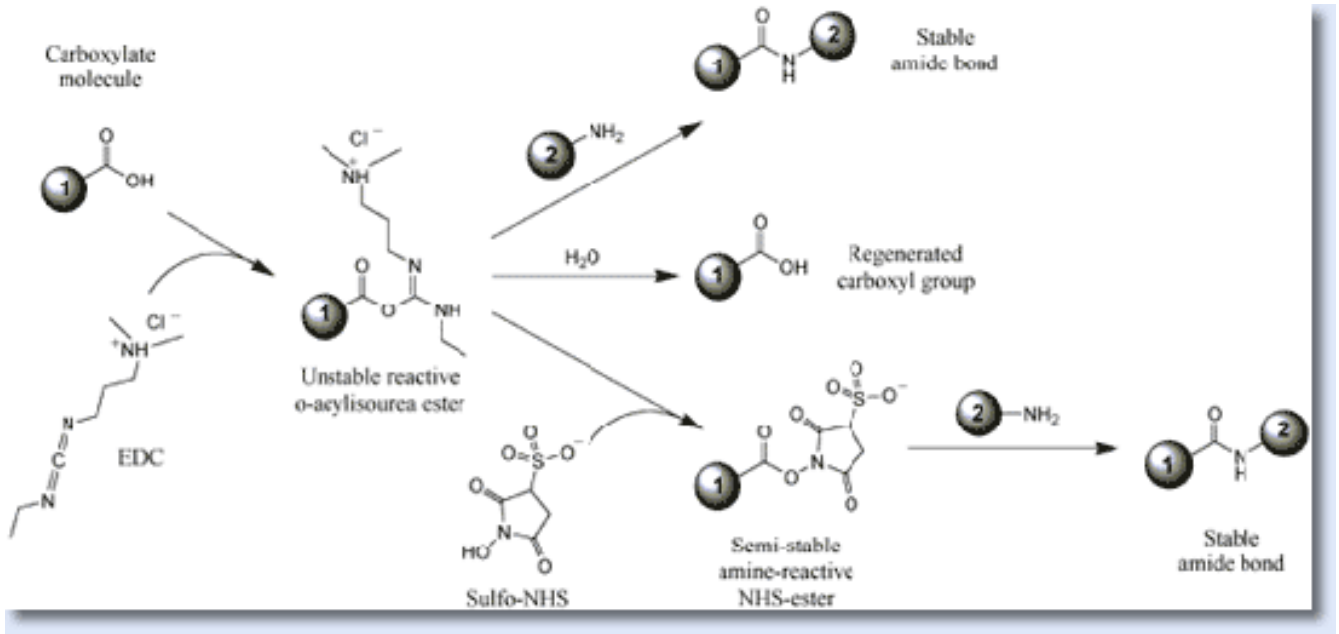

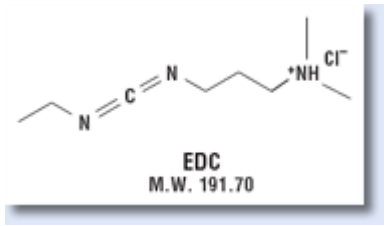

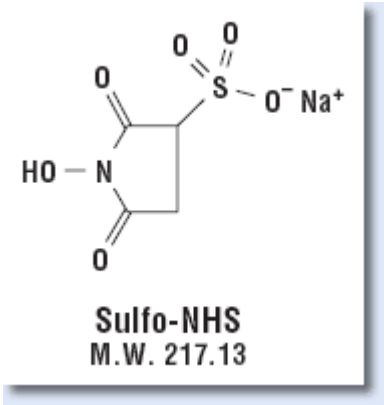

EDC (1-Ethyl-3-[3-dimethylaminopropyl]carbodiimide Hydrochloride)

Amine Presenting Surface

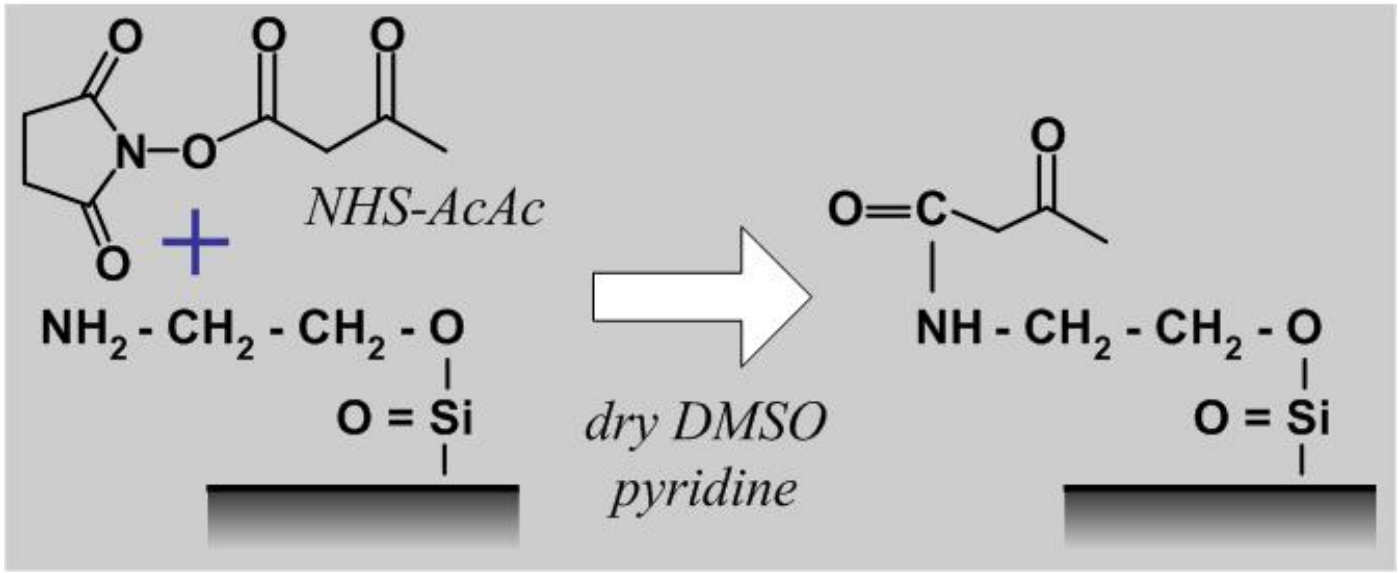

Sulfhydryl Labeling

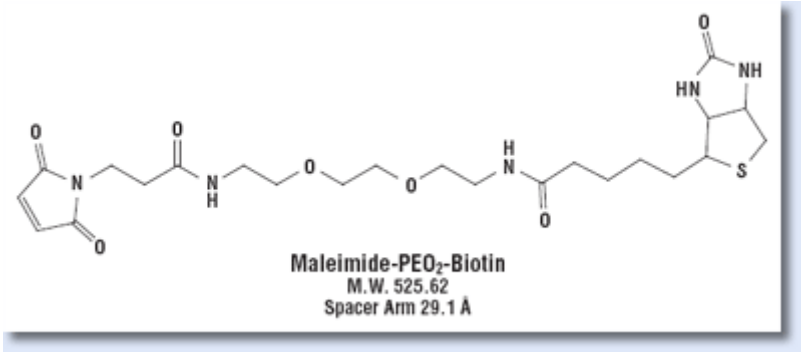

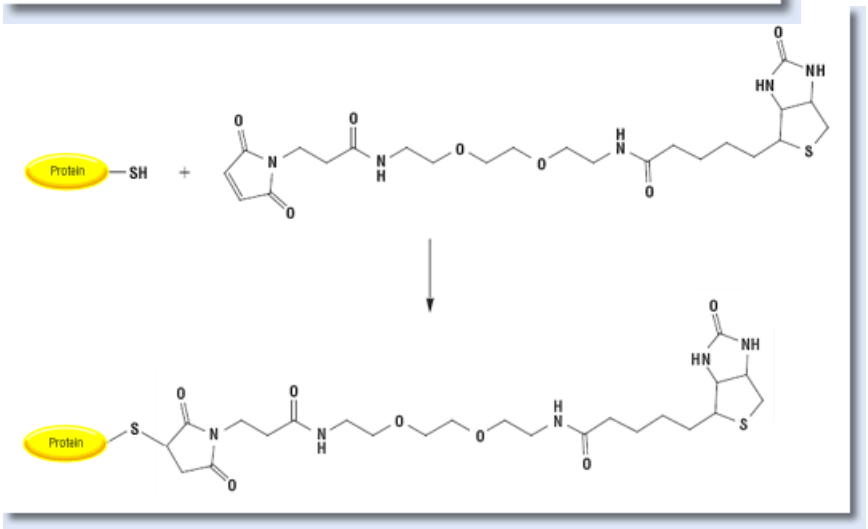

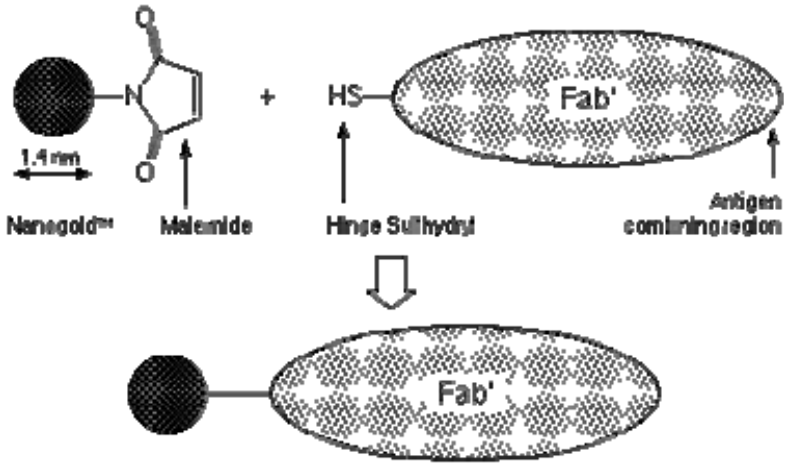

Silica Modification

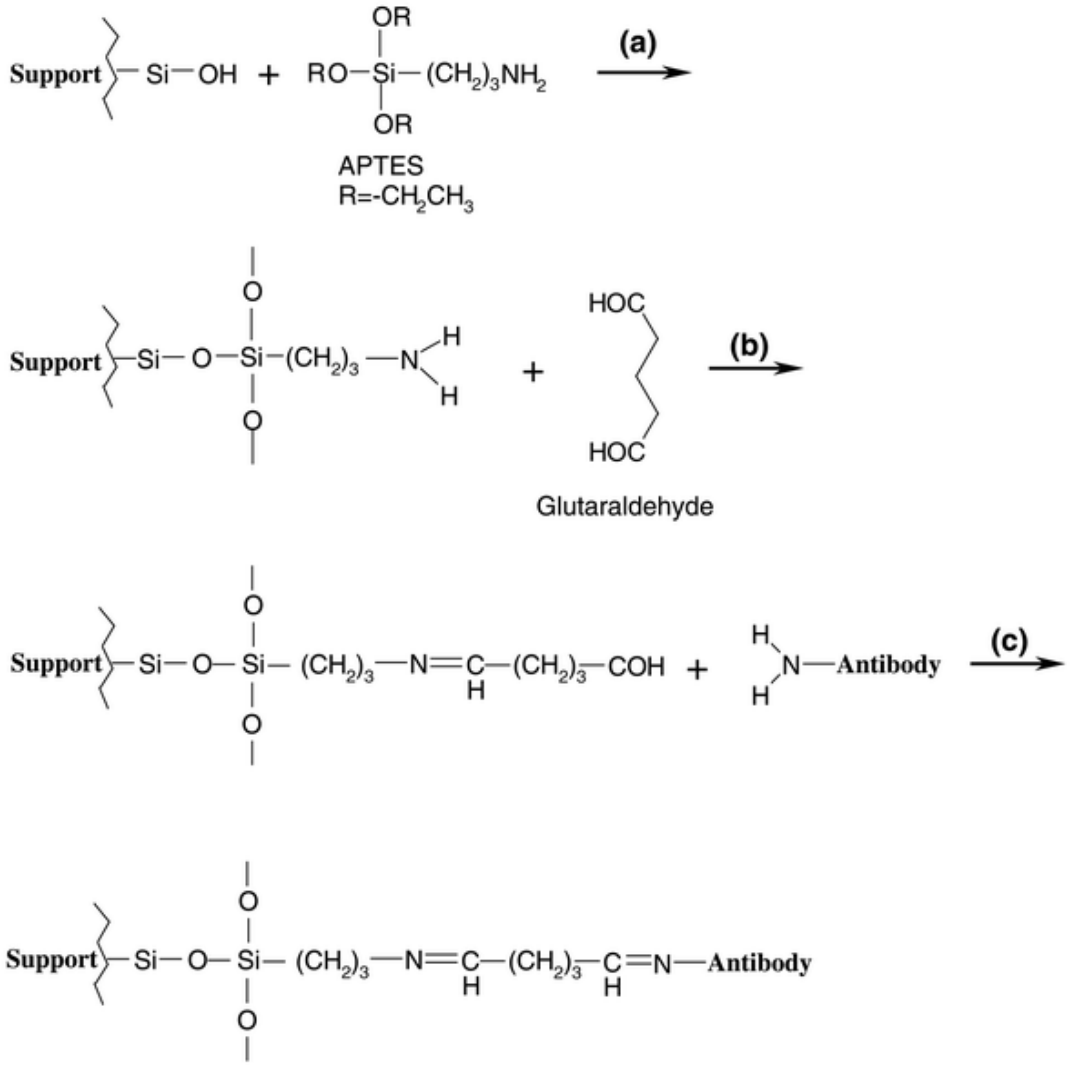

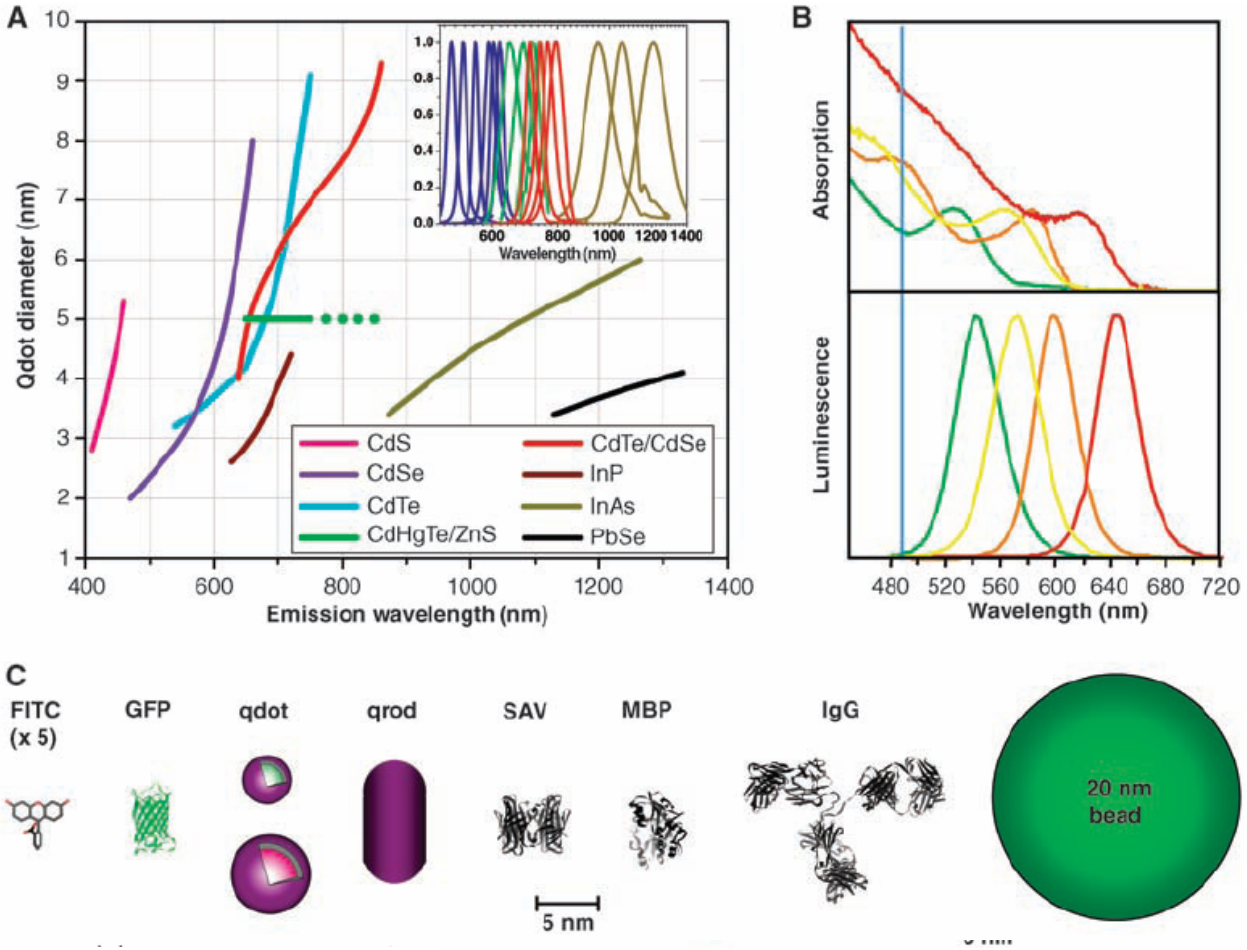

Fig. 1. (**A**) Emission maxima and sizes of quantum dots of different composition. Quantum dots can be synthesized from various types of semiconductor materials (II-VI: CdS, CdSe, CdTe…; III-V: InP, InAs…; IV-VI: PbSe…) characterized by different bulk band gap energies. The curves represent experimental data from the literature on the dependence of peak emission wavelength on qdot diameter. The range of emission wavelength is 400 to 1350 nm, with size varying from 2 to 9.5 nm (organic passivation/solubilization layer not included). All spectra are typically around 30 to 50 nm (full width at half maximum). Inset: Representative emission spectra for some materials. Data are from (*12*, *18*, *27*, *76*–*82*). Data for CdHgTe/ZnS have been extrapolated to the maximum emission wavelength obtained in our group. (**B**) Absorption (upper curves) and emission (lower curves) spectra of four CdSe/ZnS qdot samples. The blue vertical line indicates the 488-nm line of an argon-ion laser, which can be used to efficiently excite all four types of qdots simultaneously. [Adapted from (*28*)] (**C**) Size comparison of qdots and comparable objects. FITC, fluorescein isothiocyanate; GFP, green fluorescent protein; qdot, green (4 nm, top) and red (6.5 nm, bottom) CdSe/ZnS qdot; qrod, rod-shaped qdot (size from Quantum Dot Corp.'s Web site). Three proteins—streptavidin (SAV), maltose binding protein (MBP), and immunoglobulin G (IgG)—have been used for further functionalization of qdots (see text) and add to the final size of the qdot, in conjunction with the solubilization chemistry (Fig. 2).

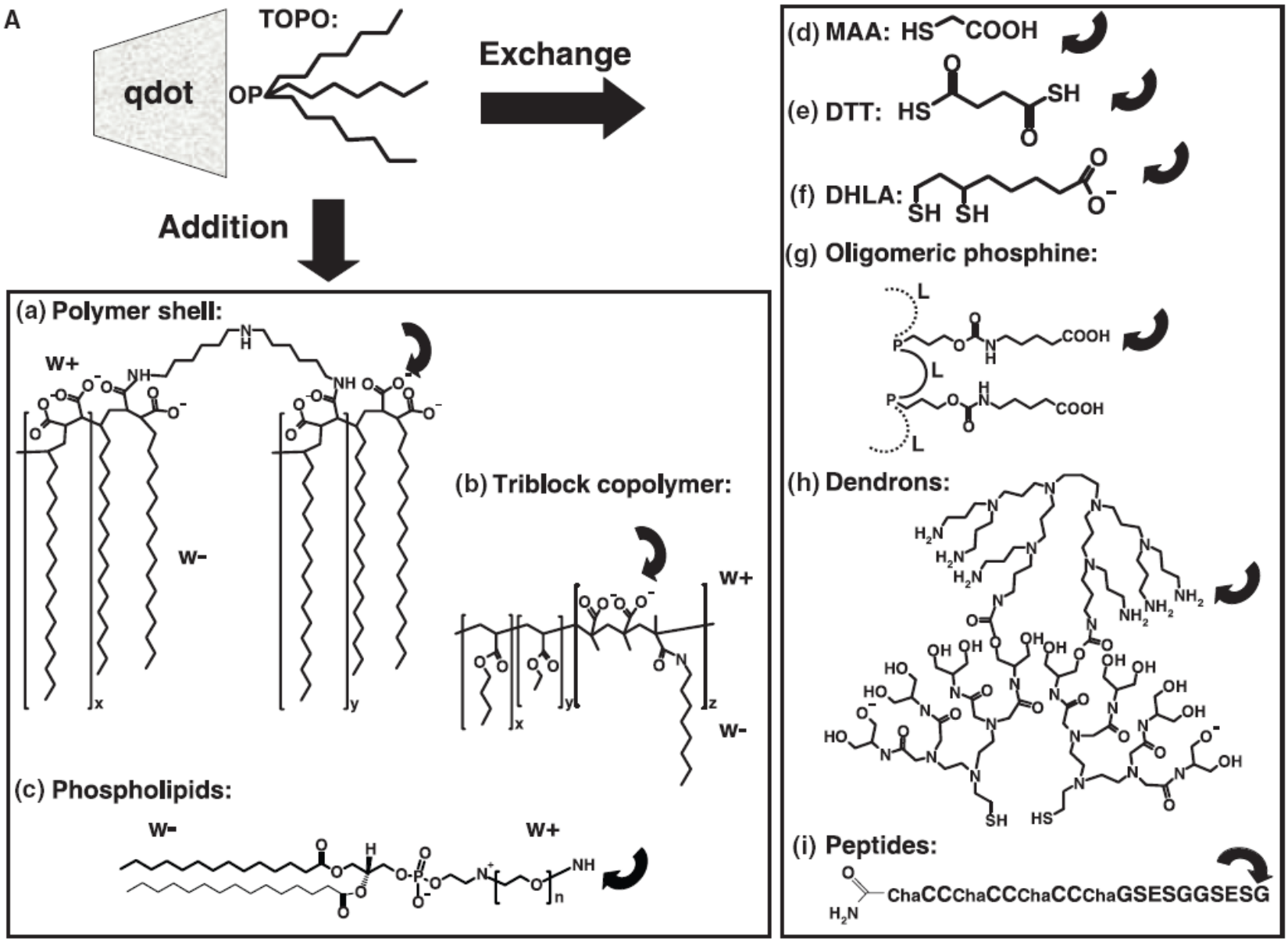
A
qdot
TOPO:
OP
Exchange
Addition
(a) Polymer shell:
W+
W-
(b) Triblock copolymer:
W+
W-
(c) Phospholipids:
W-
W+
(d) MAA: HS COOH
(e) DTT: HS SH
(f) DHLA: SH SH
(g) Oligomeric phosphine:
COOH
COOH
(h) Dendrons:
(i) Peptides:
ChaCCChaCCChaCCChaGSESGGSESG

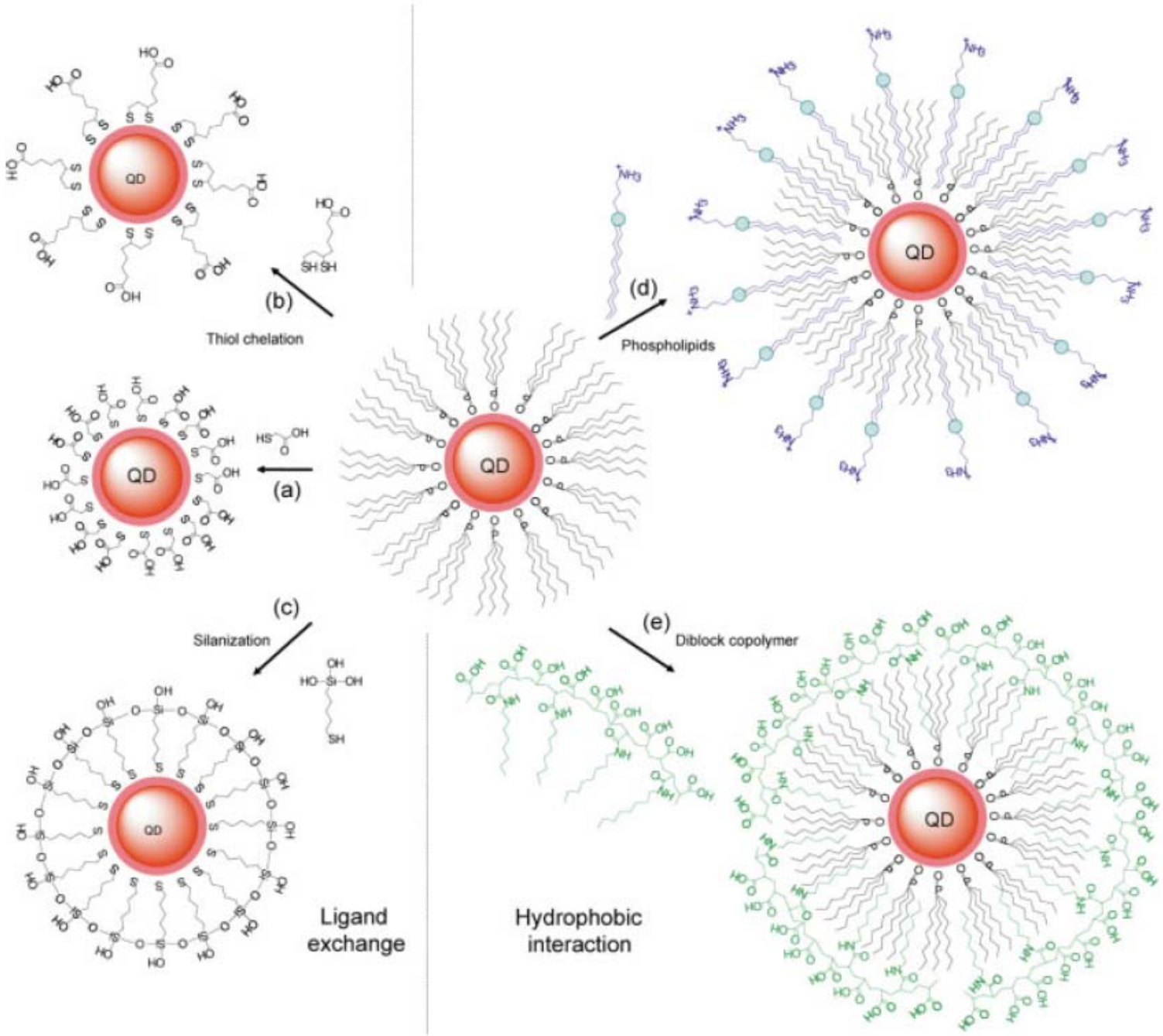
QD
(a)
(b)
Thiol chelation
(c)
Silanization
Ligand exchange
(d)
Phospholipids
(e)
Diblock copolymer
Hydrophobic interaction

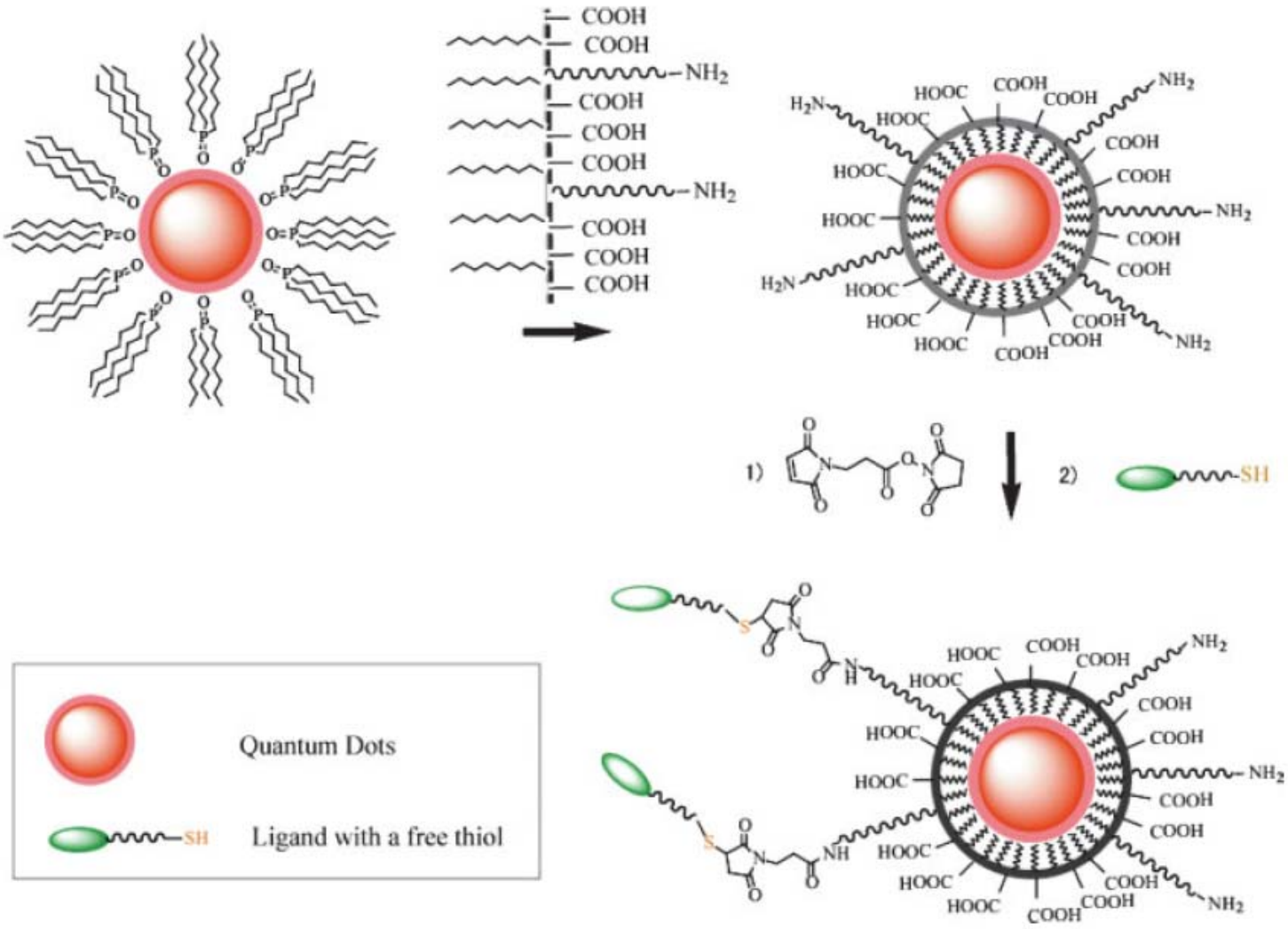

FIGURE 3 Maleimide functionalized QDs for conjugating thiol-containing ligands. TOPO stabilized QDs are coated with a primary amine functionalized tri-block amphiphilic copolymer for producing water-soluble QDs, which facilitate further conjugation to ligands with free thiols through bi-functional cross-linkers.

Cells incubated with tiopronin coated QDs

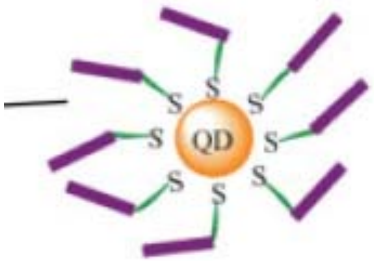

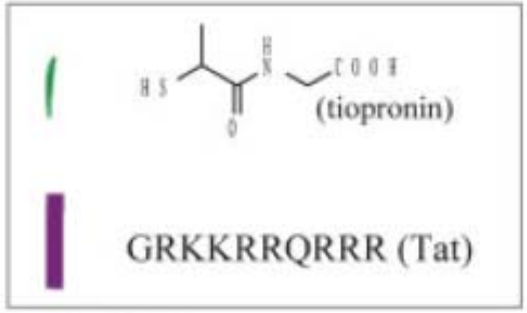

Cells incubated with Tat functionlized QDs

Scheme 1. Modular Design of Hydrophilic Ligands with Terminal Functional Groups Used in This Study

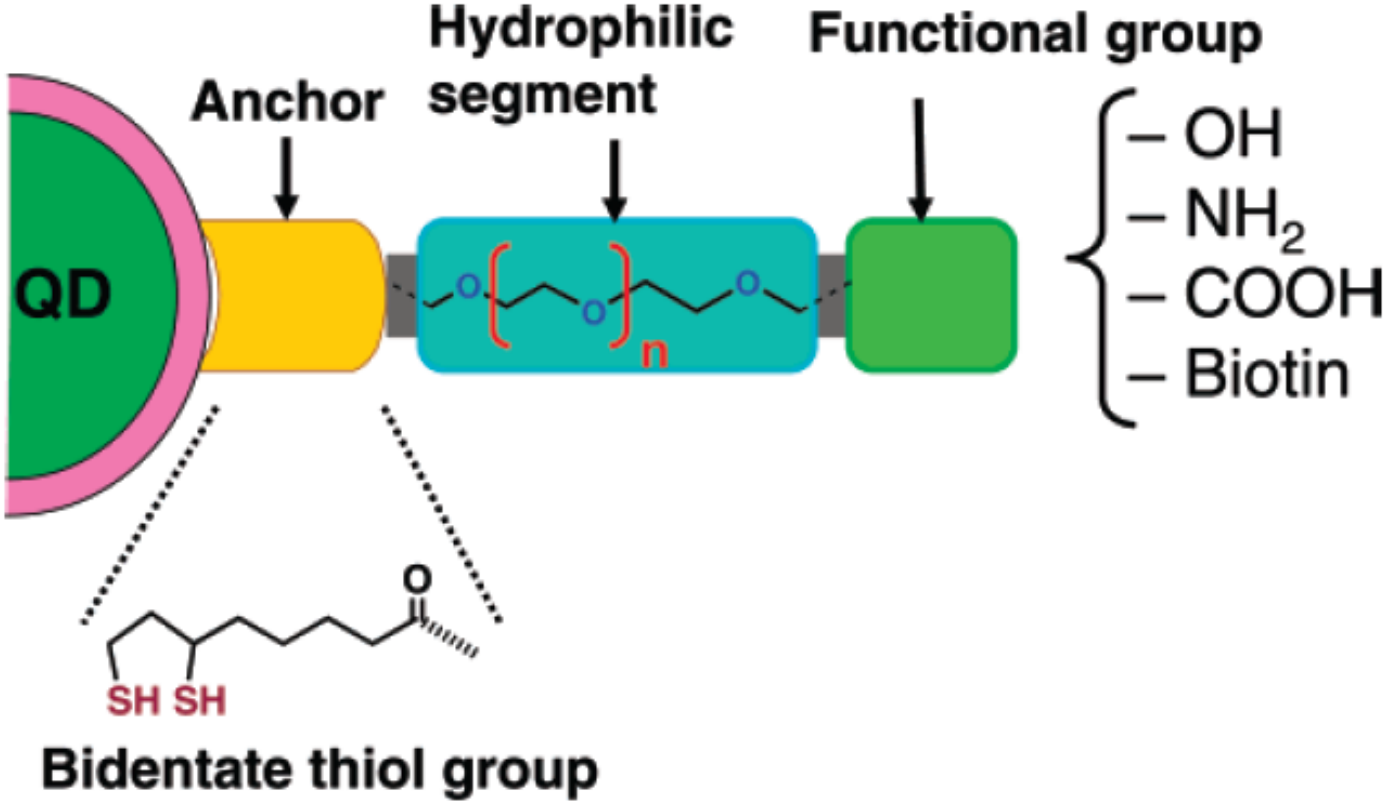

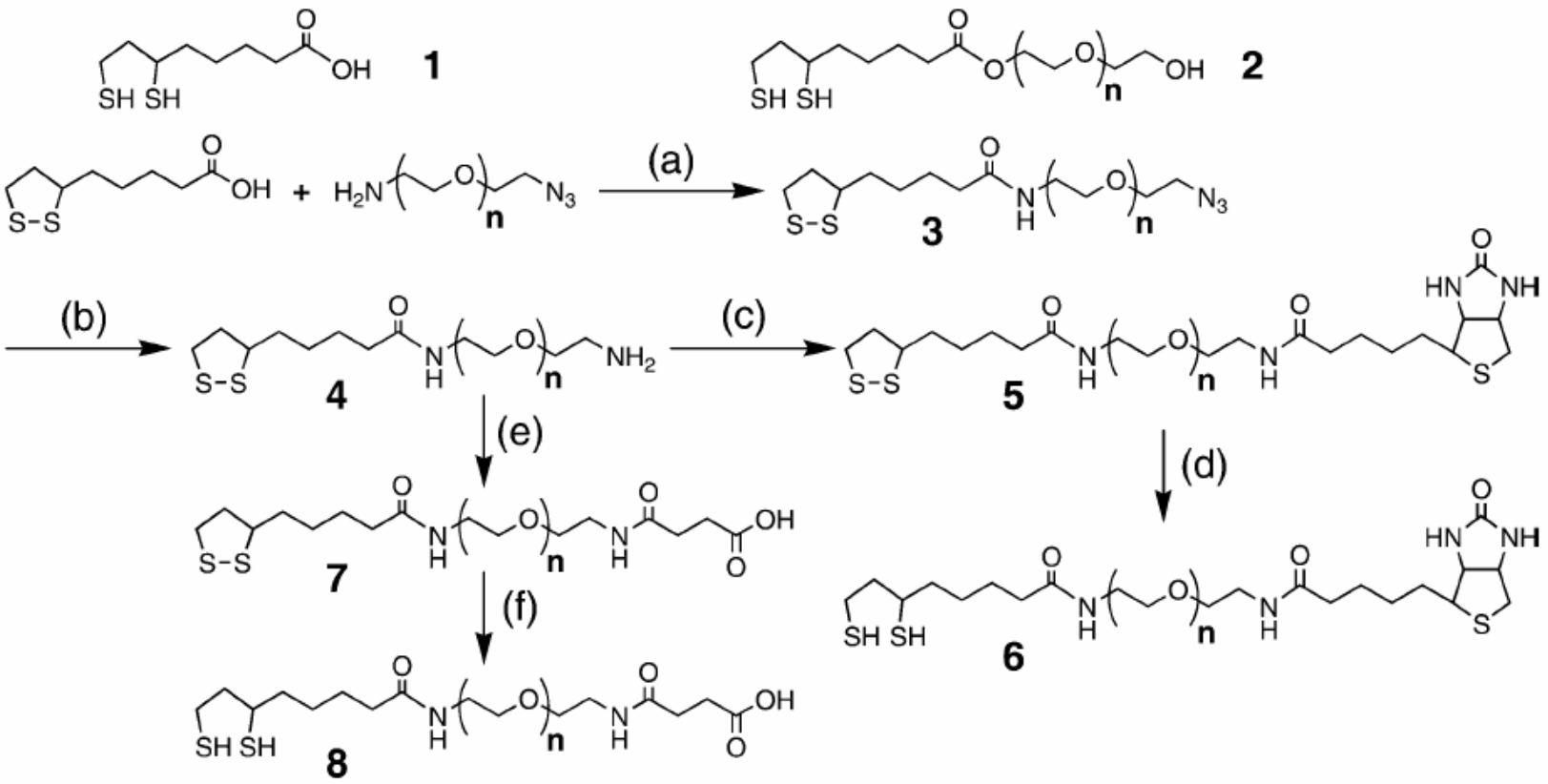

Figure 1. Chemical structures and synthetic routes of the surface ligands used in this study: (a) DCC, DMAP, CH_2Cl_2; (b) PPh_3, H_2O, THF; (c) biotin *N*-hydroxysuccinimide ester, Et_3N, DMF; (d) $NaBH_4$, EtOH, H_2O; (e) succinic anhydride, pyridine; (f) $NaBH_4$, EtOH, H_2O.

Plasmonics

Plasmonics in Biology and Plasmon-Controlled Fluorescence

Joseph R. Lakowicz

Plasmonics (2006) 1: 5–33

Chem. Rev. **2008,** *108,* 494–521

Nanostructured Plasmonic Sensors

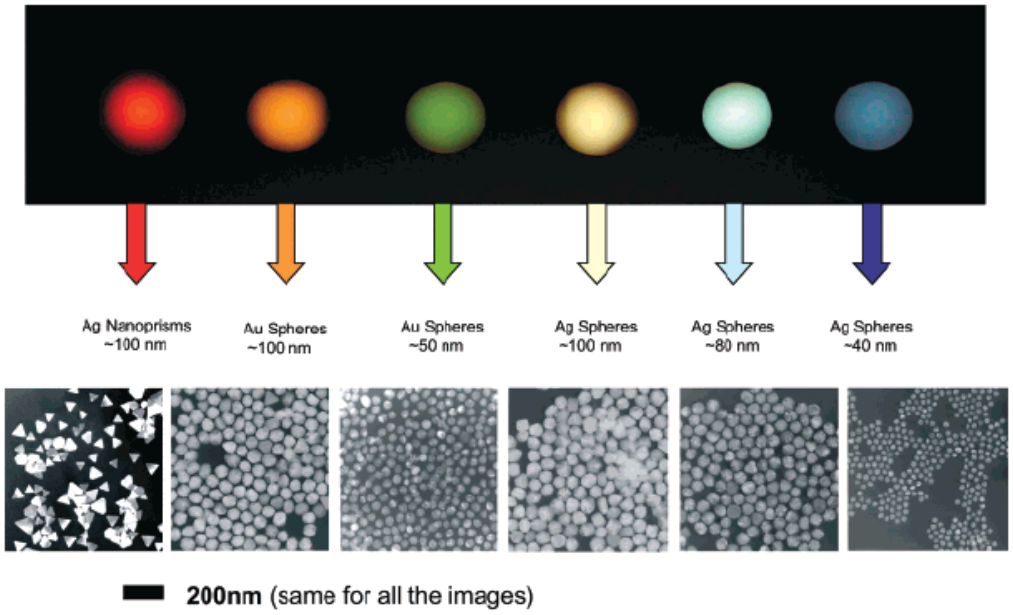

Surface Plasmon

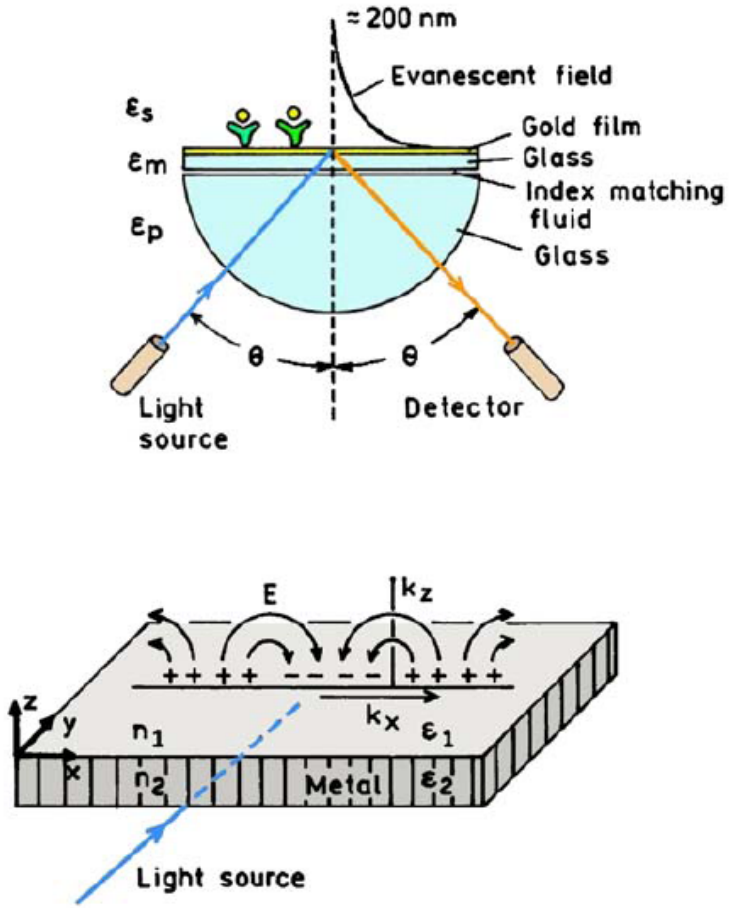

Figure 3. Schematics of an SPR experiment (top) and of the light-induced surface plasmons (bottom).

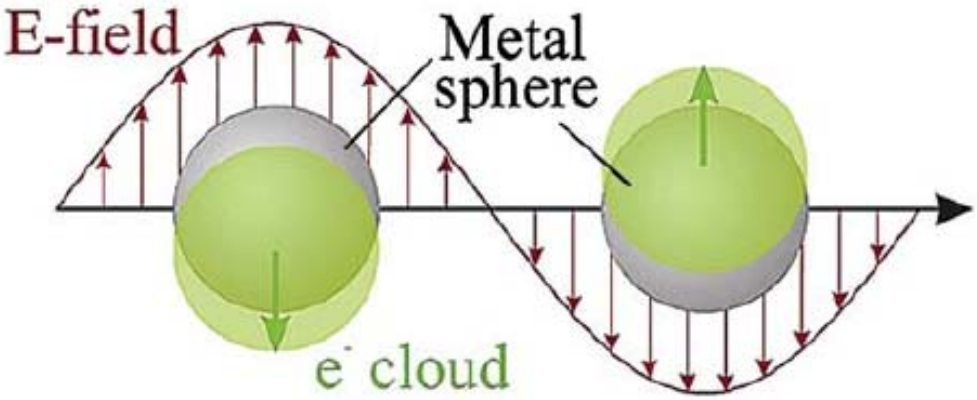

Figure 6. Schematic of plasmon oscillation for a sphere. From [39].

Drift: Drude model

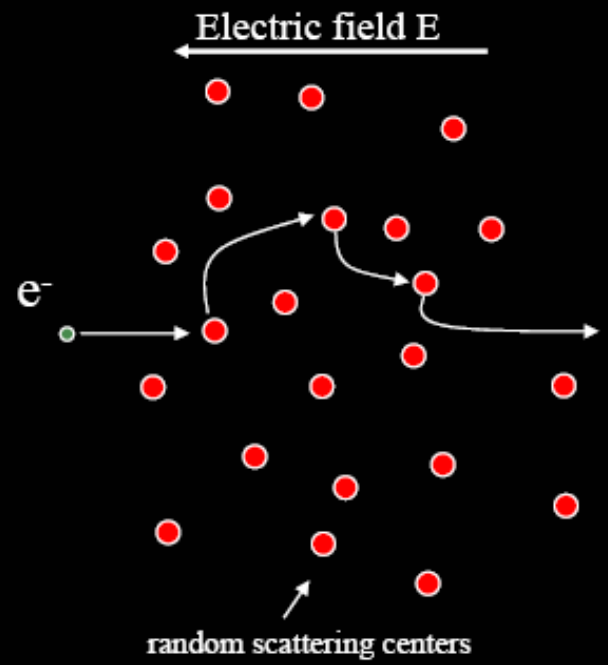

$$F = ma$$

$$eE = m\frac{\partial v}{\partial t}$$

$$v_{avg} = \underbrace{\frac{e\tau}{m}}_{\mu} E$$

$$j = nev_{avg} = \underbrace{\frac{ne^2\tau}{m}}_{\sigma} E$$

$$m\frac{\partial}{\partial t}\langle\vec{v}\rangle = q\vec{E} - \gamma\langle\vec{v}\rangle$$

$$\sigma(\omega) = \frac{\sigma_0}{1 + i\omega\tau}$$

Far-Field Optical Microscopy of Single Metal Nanoparticles

Acc. Chem. Res. **2005**, *38*, 594–601

The optical properties of metals are, to a large extent, determined by conduction electrons. The response of these free electrons follows the Drude model. They collectively react to perturbation by an external electric field. The Coulomb restoring force between the electrons and the lattice leads to harmonic oscillations with the plasma frequency $\omega_p^2 = Ne^2/(m_e\epsilon_0)$ where N is the electron density and m_e the electron mass. The damping of the oscillation is described by a phenomenological damping constant, γ. In this model, the dielectric function, $\epsilon(\omega)$, equals

$$\epsilon(\omega) = 1 - \frac{\omega_p^2}{\omega(\omega + i\gamma)}$$

For noble metals, the contribution of the bound d-electrons to the optical properties cannot be neglected.[9]

Maxwell Equations

$$\nabla \cdot \vec{H} = 0, \tag{4.}$$

$$\nabla \cdot \vec{E} = 0, \tag{5.}$$

$$\nabla \times \vec{E} + \frac{1}{c}\frac{\partial \vec{H}}{\partial t} = 0, \tag{6.}$$

$$\nabla \times \vec{H} - \frac{\varepsilon}{c}\frac{\partial \vec{E}}{\partial t} = 0, \tag{7.}$$

Surface Plasmon Polaritons (SPP)

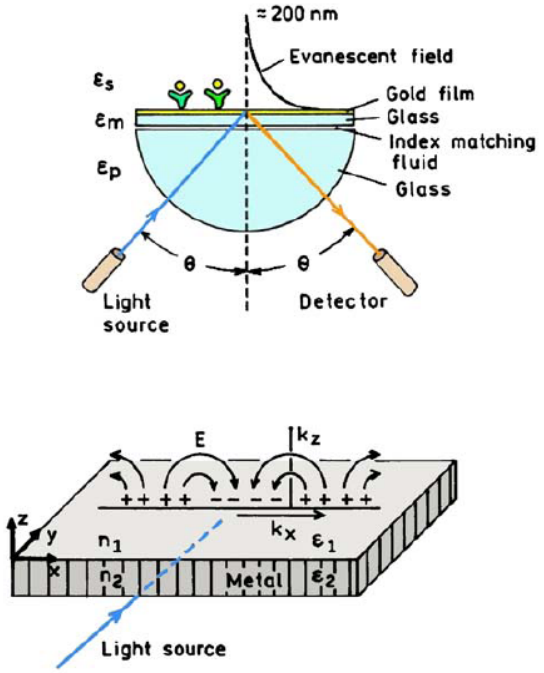

Figure 3. Schematics of an SPR experiment (top) and of the light-induced surface plasmons (bottom).

$$k_{sp} = \frac{\omega}{c}\left(\frac{\varepsilon_m \varepsilon_s}{\varepsilon_m + \varepsilon_s}\right)^{1/2} = k_0\left(\frac{\varepsilon_m \varepsilon_s}{\varepsilon_m + \varepsilon_s}\right)^{1/2} \quad (1)$$

$$\varepsilon_m = \varepsilon_r + i\varepsilon_{im} \quad (2)$$

$$k_{sp} = k_0\left(\frac{\varepsilon_r \varepsilon_s}{\varepsilon_r + \varepsilon_s}\right)^{1/2} \quad (3)$$

$$k_p = k_0 n_p \quad (4)$$

$$k_{sp} = k_x = k_0\, n_p \sin\theta_{sp} \quad (5)$$

Dielectric Constant

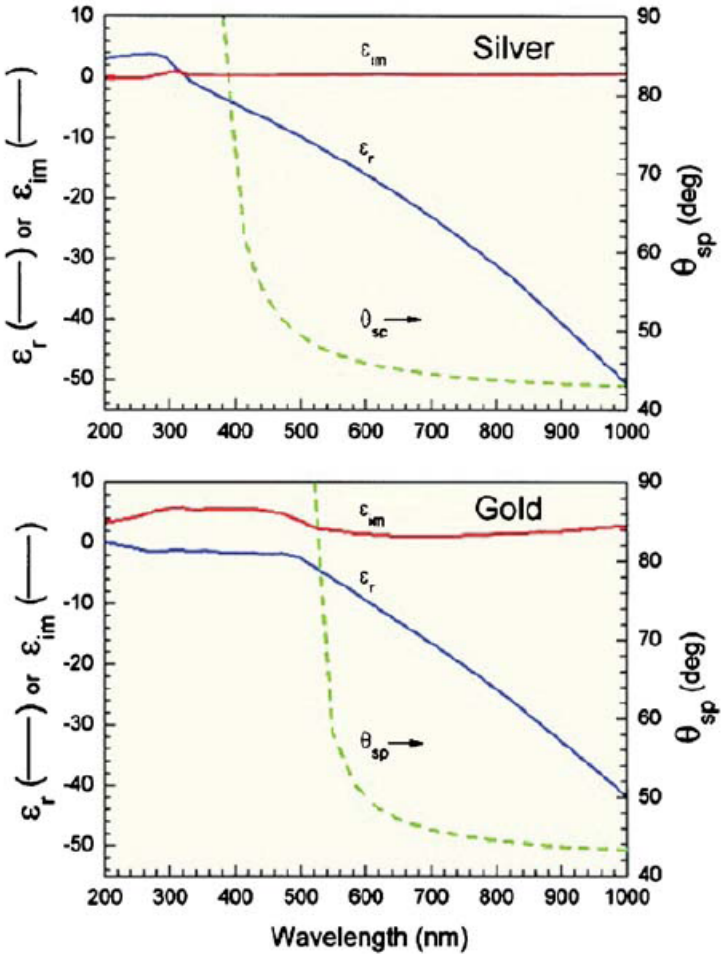

Figure 4. Dielectric constants for silver and gold.

$$\epsilon(\lambda) = \epsilon_r(\lambda) + i\epsilon_i(\lambda)$$

$$\epsilon = m^2 \text{ and } m = n + ik$$

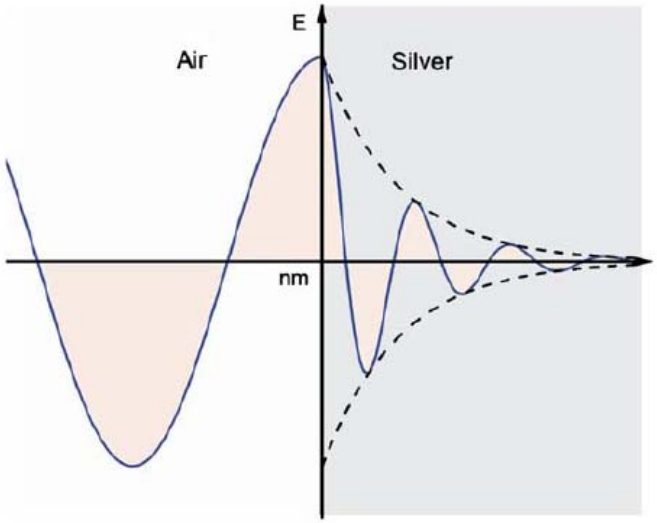

Figure 5. Schematic of attenuation of 600 nm light on a metal surface.

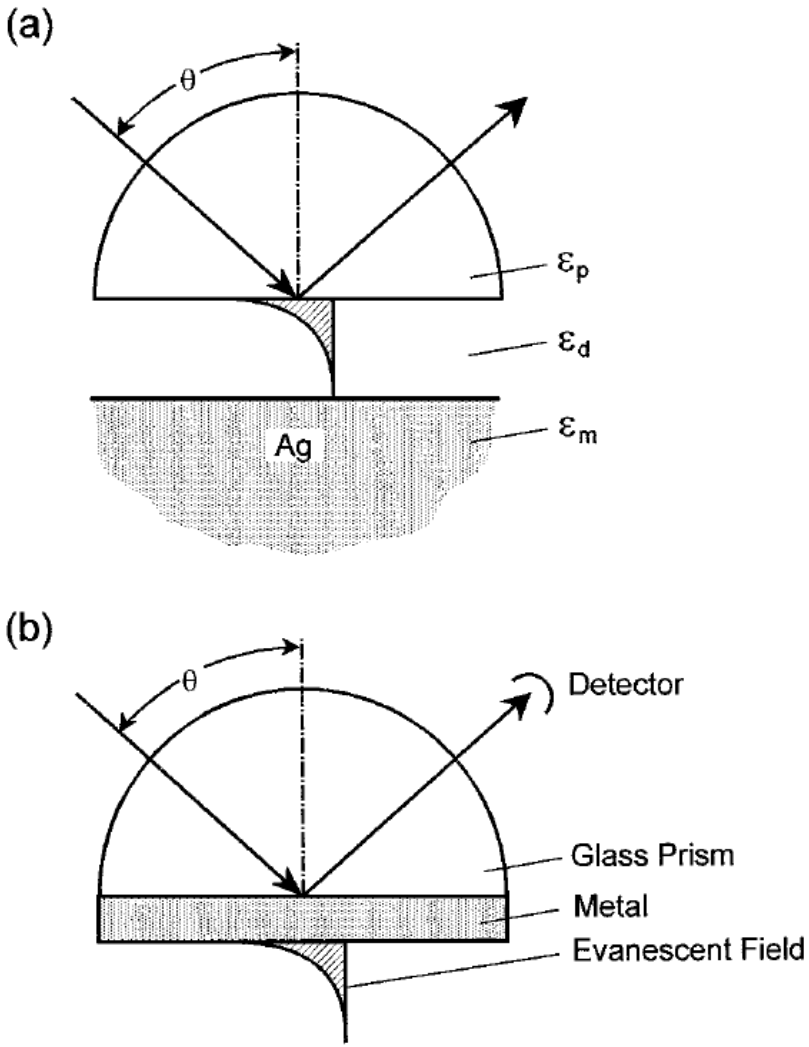

Figure 4 (*a*) The Otto configuration is based on the total internal reflection of a plane wave incident at an angle θ at the base of a prism. The evanescent tail of this inhomogeneous wave can excite PSP states at an Ag-dielectric interface, provided the coupling gap is sufficiently narrow. (*b*) Attenuated total internal reflection (ATR) construct for PSP excitation in the Kretschmann geometry. A thin metal film ($d \sim 50$ nm) is evaporated onto the base of the prism and acts as a resonator driven by the photon field incident at an angle θ.

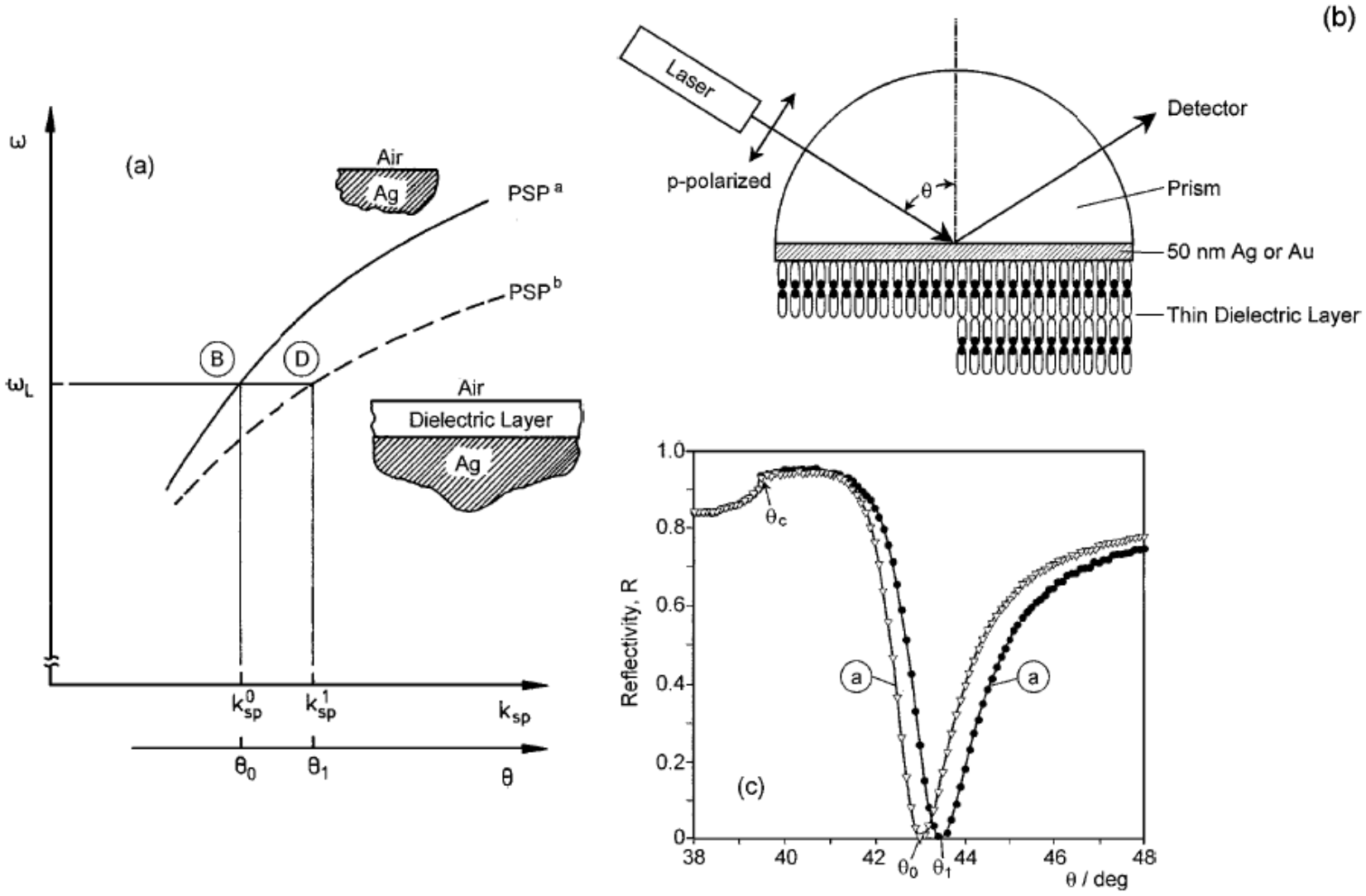

after self-assembling a monomolecular layer of HS-$(CH_2)_{21}$-OH. The symbols are experimental data points; the full curves are Fresnel fits with $\varepsilon_{BK7} = 2.29$, $\tilde{\varepsilon}_{Au} = -12.45 + i \cdot 1.3$, $d_{Au} = 46.9$ nm, $\varepsilon_{layer} = 2.1025$, $d_{layer} = 2.65$ nm. Data were taken at $\lambda = 633$ nm in air.

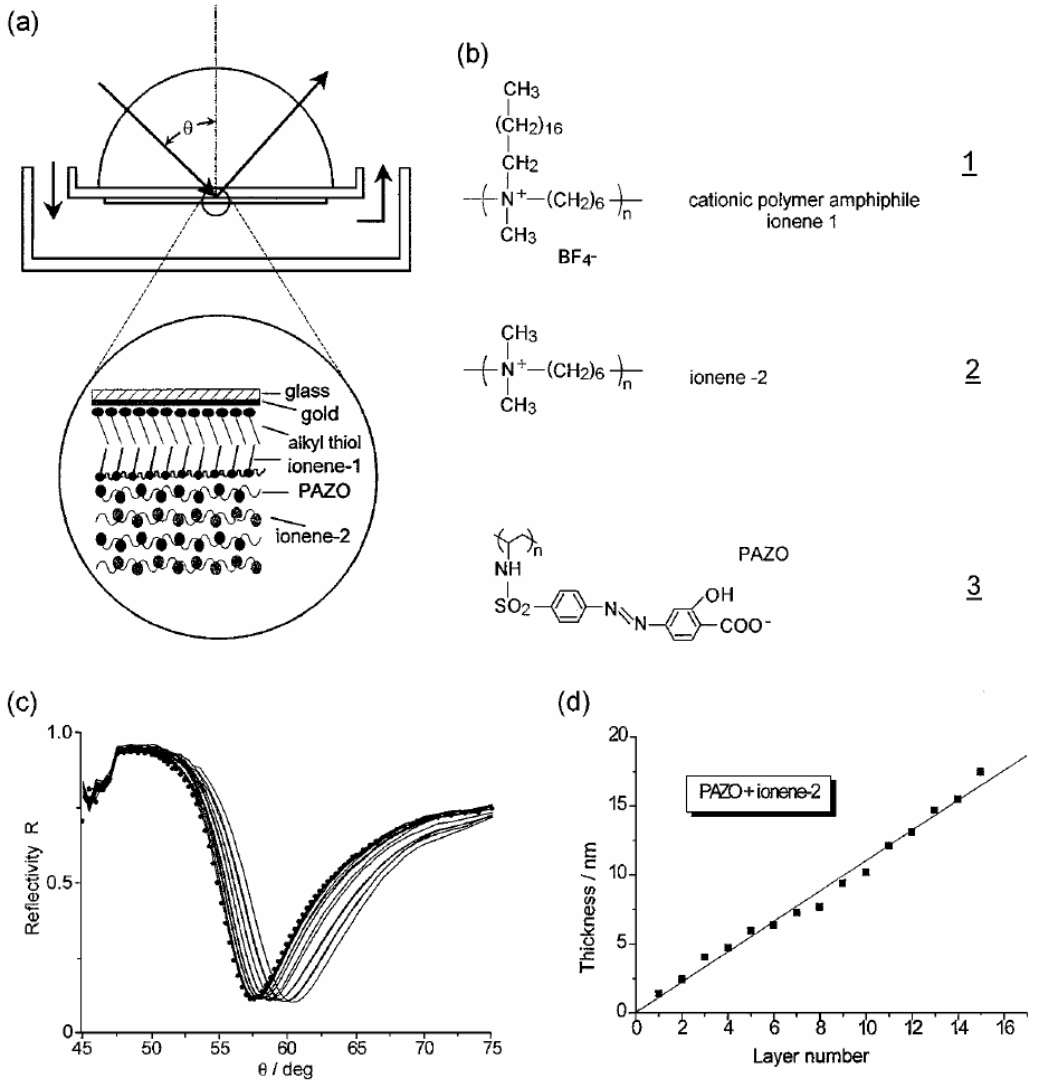

Figure 14 (*a*) Experimental construct for on-line surface plasmon optical observation of the alternating deposition of cationic and anionic polymers from solution to an Au substrate precoated by an alkyl thiol and an ionene-1 monolayer [refer to (*b*)]. The build-up architecture is given in the enlargement. (*b*) Structural formulas of the employed materials. (*c*) Series of ATR scans taken after each polyelectrolyte monolayer deposition. (*d*) Thickness increase as obtained from the ATR scans given in (*c*).

Nanoparticle Enhancement

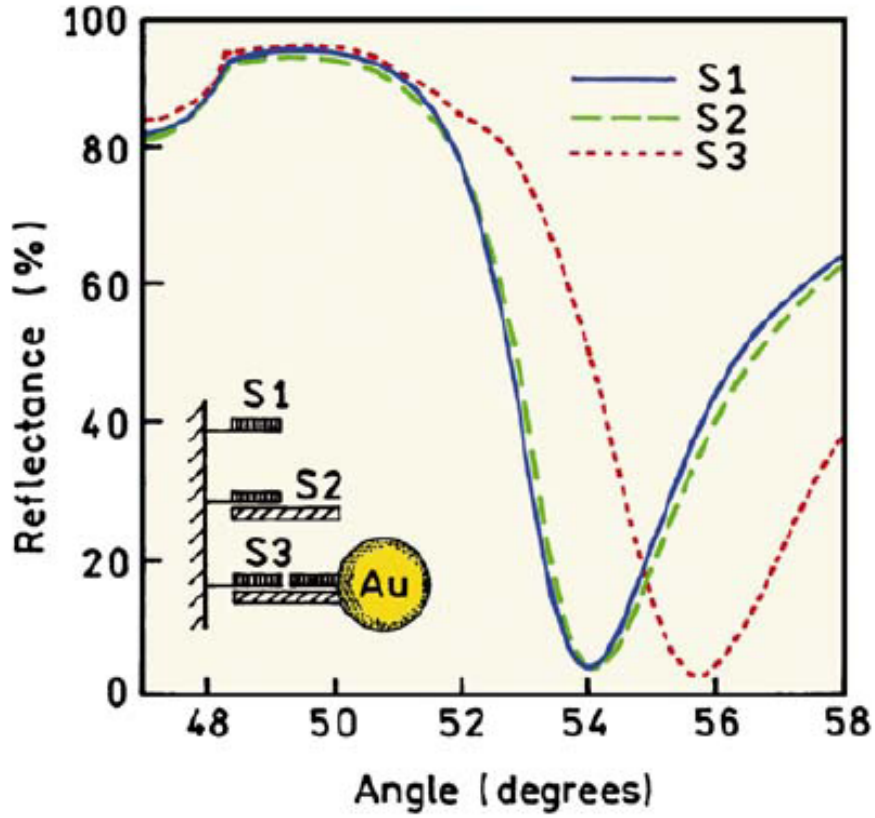

Figure 12. SPR measurements of DNA hybridization without (S2) and with Au particle amplification (S3). Revised from [51].

Localized Surface Plasmon

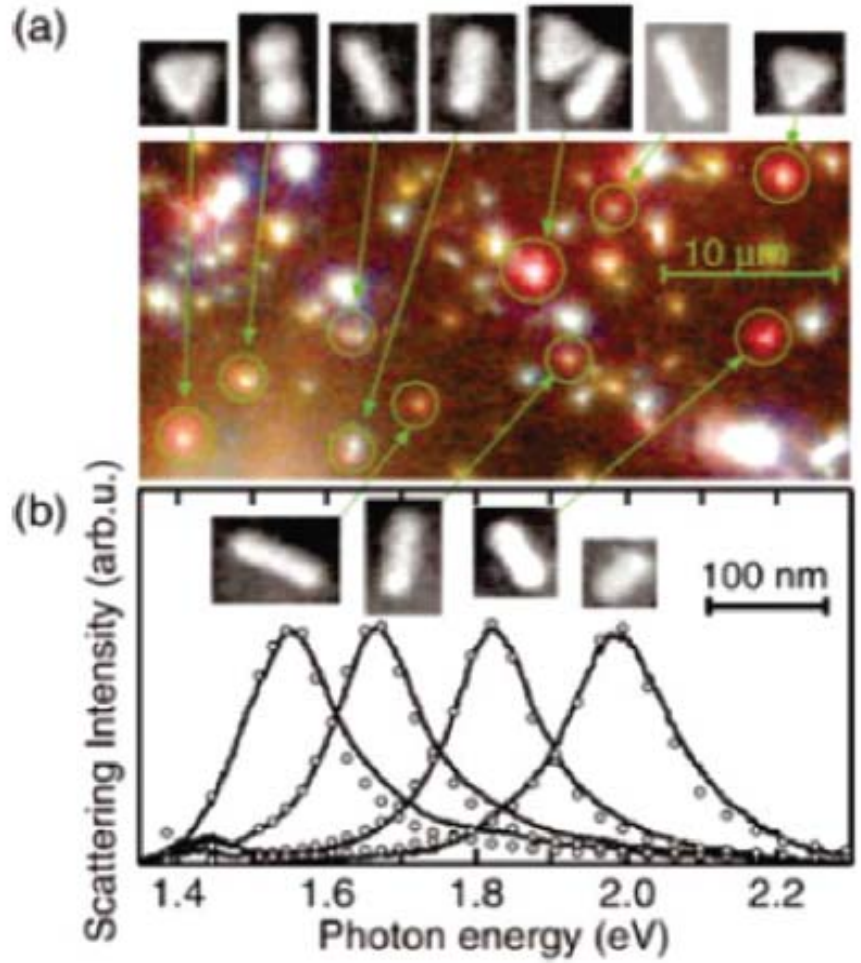

Figure 2. (a) Dark-field microscopy image and corresponding SEM images and (b) light scattering spectra of Au nanocrystals of different shapes. Reprinted with permission from ref 54. Copyright 2003 American Institute of Physics.

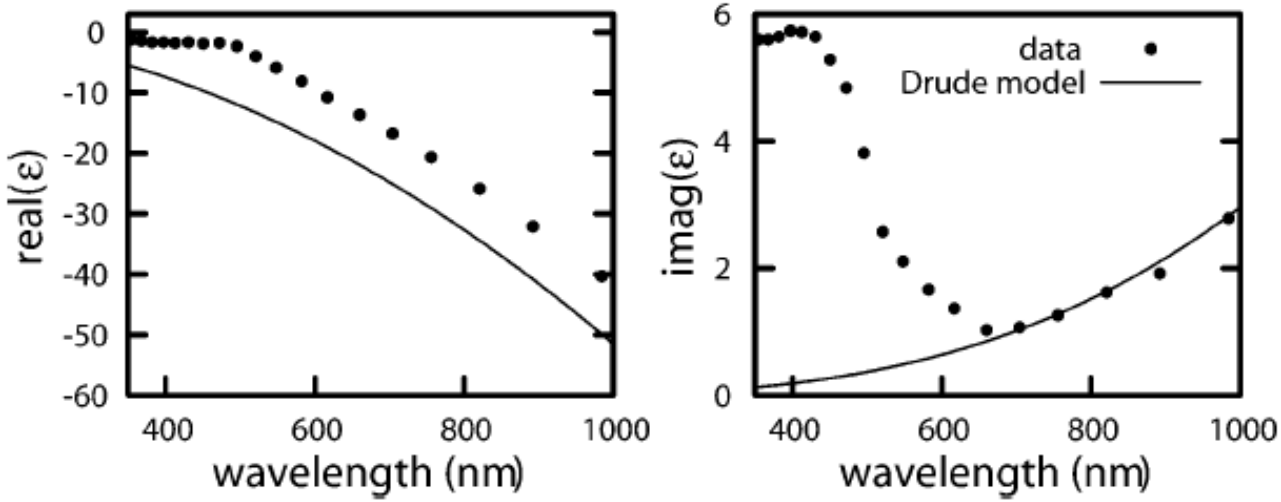

FIGURE 1. Dielectric function of gold[8] compared with the free electron model of Drude. The deviations are due to the interband contribution.

$$\sigma_{\text{ext}} = \sigma_{\text{abs}} + \sigma_{\text{sca}}.$$

$$m^2 = \frac{\epsilon_{\text{metal}}}{\epsilon_{\text{medium}}} \qquad -2$$

Mie's theory

$$\sigma_{\text{ext}} = 2\frac{2\pi}{k^2}x^3\ \text{Im}\left(\frac{m^2-1}{m^2+2}\right)$$

$$\sigma_{\text{sca}} = \frac{4}{3}\frac{2\pi}{k^2}x^6\left|\frac{m^2-1}{m^2+2}\right|^2$$

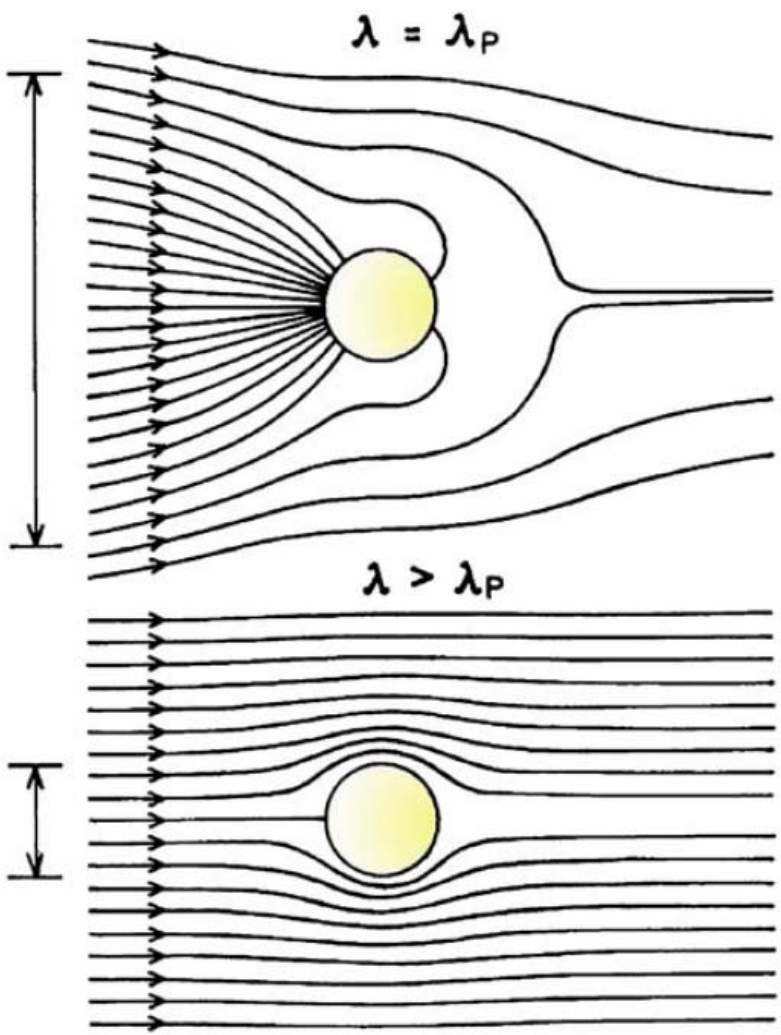

Figure 7. Poynting vector or energy flow (lines) around a subwavelength metallic colloid illuminated at the plasmon wavelength (top) and at a wavelength longer than the plasmon wavelength (bottom). The vertical lines on the left indicate the diameter of the cross sections for absorption. This diagram does not show the energy flow due to scattered light. From [40].

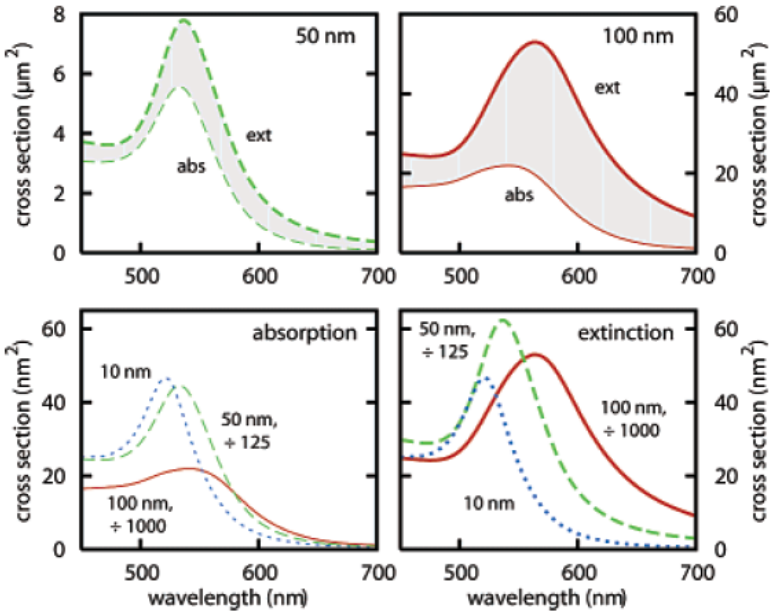

FIGURE 2. Extinction (thick lines) and absorption (thin lines) spectra of gold particles with a diameter of 10 nm (blue, dotted), 50 nm (green, dashed), and 100 nm (red, solid) plotted in different combinations of the same curves. The surrounding medium is water ($n = 1.3$). In the top panels, with increasing colloid size the additional scattering contribution to the extinction becomes more important; the gap between absorption and scattering spectra gets larger. In the bottom panels to compare colloids of different sizes the spectra are scaled with d^3 to the 10-nm particle. Both absorption and scattering spectra show a red shift and broadening of the plasmon resonance with particle size.

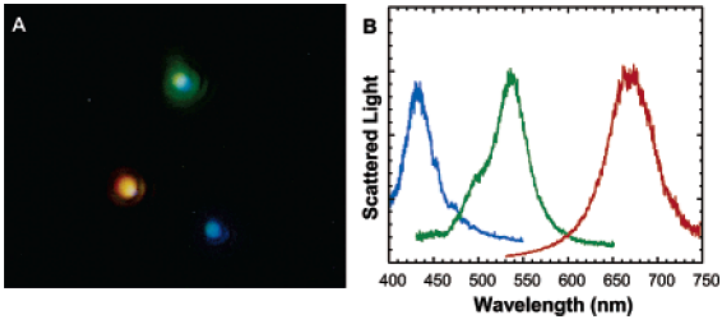

FIGURE 3. Dark-field image of silver particles of different sizes leading to different colors in the scattered white light.[15] The spot size is about 400 nm, and the height of the image is about 9 μm. The corresponding spectra are shown in the right panel. Reprinted with permission from ref 15. Copyright 2000 National Academy of Sciences, U.S.A.

Plasmonic Sensors

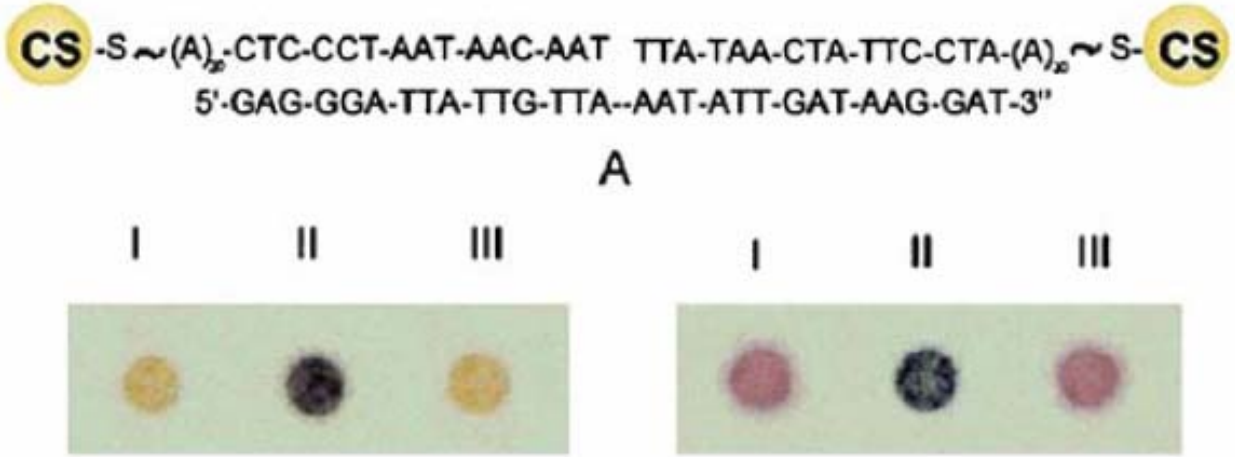

Figure 8. Top, structure of metal particle-labeled DNA with a complementary oligomer. Bottom, photographs of the labeled DNA without target (I), with target (II), and with target at $T > T_m$. On the left are Ag/Au core shell particles. On the right are Au particles. From [43].

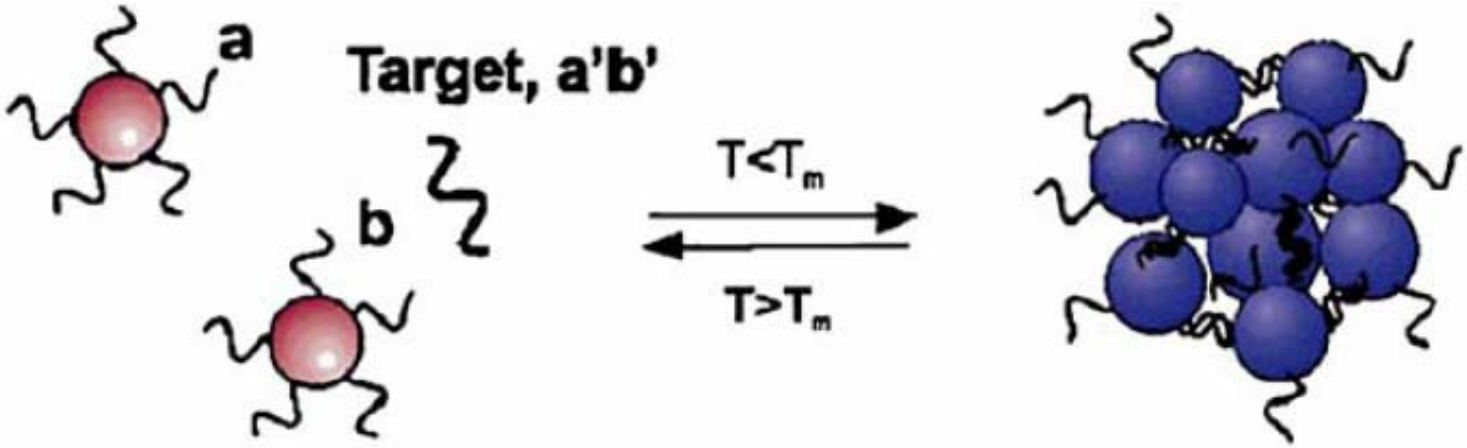
a
Target, a'b'
b
T<T_m
T>T_m

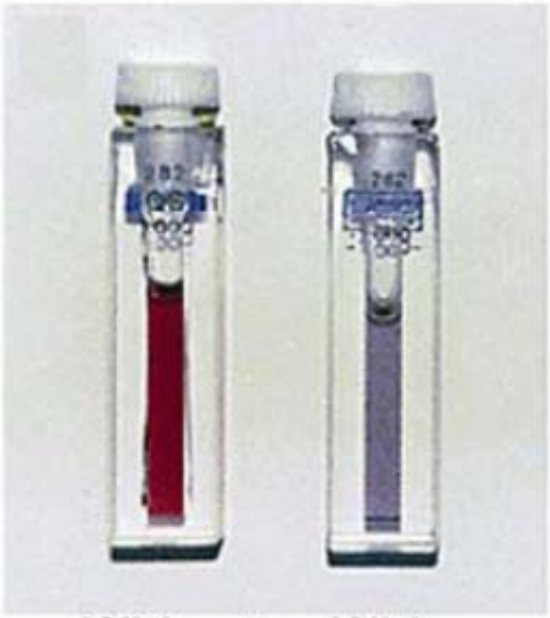
Without target
With target

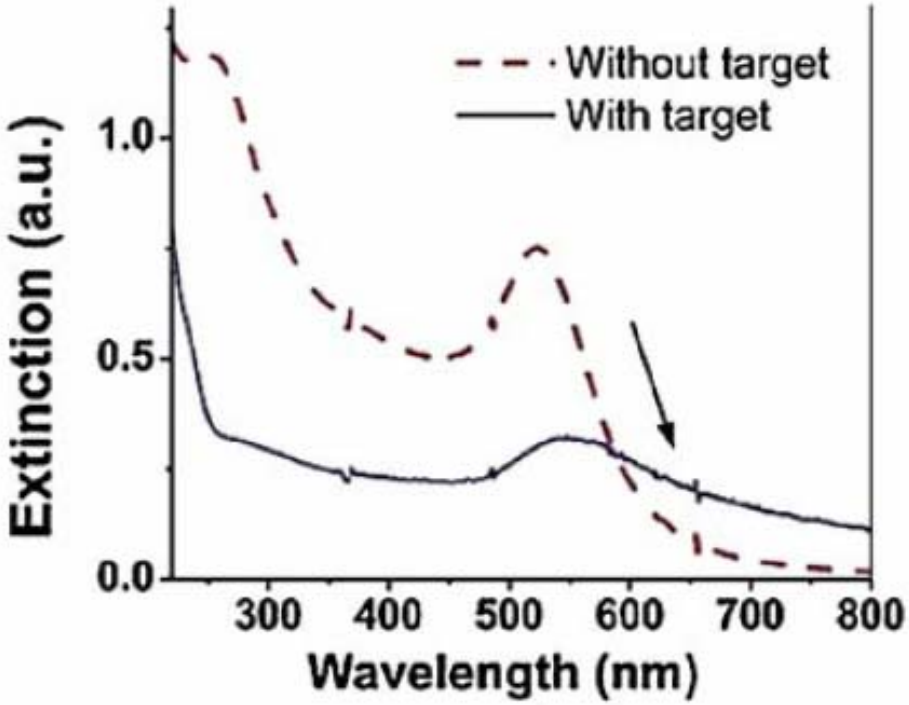
Without target
With target
Extinction (a.u.)
1.0
0.5
0.0
300
400
500
600
700
800
Wavelength (nm)

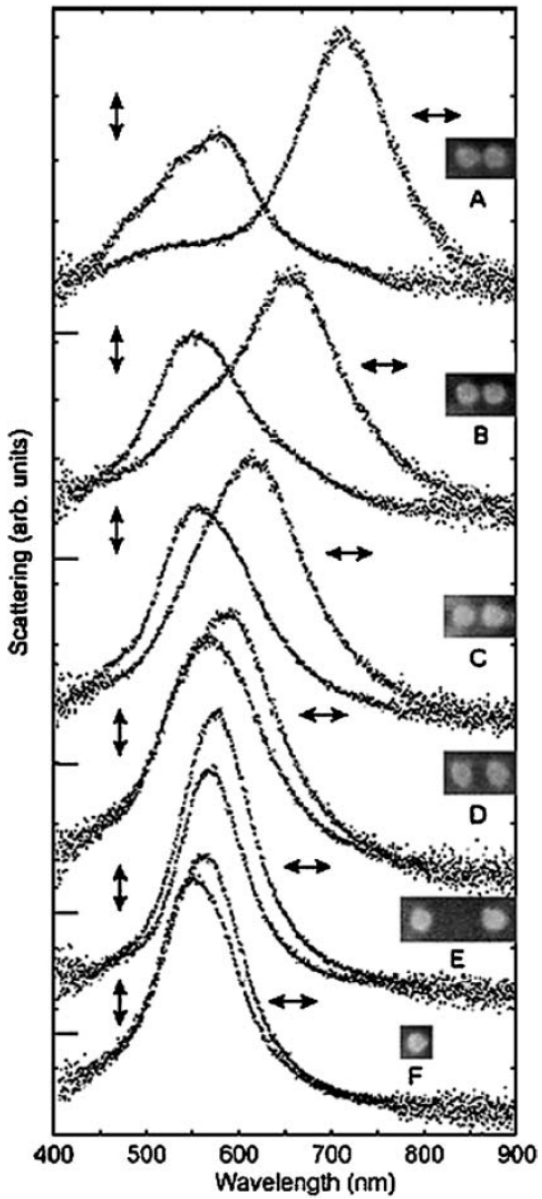

Figure 17. Dark-field scattering spectra and scanning electron micrography of isolated disk-shaped particle pairs. The arrows indicate the polarization of the incident light. The gaps between the particles are approximately 10, 15, 25, 50, and 250 nm, for A through E. F is an isolated particle. The disks are about 95 nm in diameter and 25 nm high. From [72].

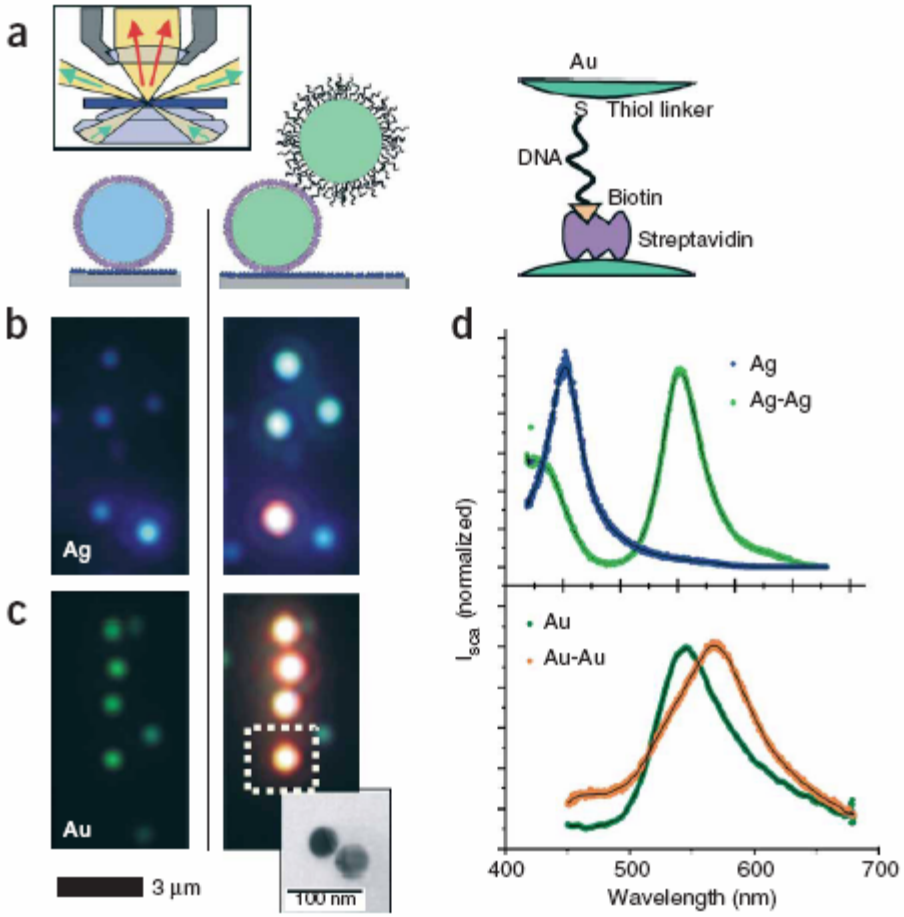

Figure 1 Color effect on directed assembly of DNA-functionalized gold and silver nanoparticles. (**a**) First, nanoparticles functionalized with streptavidin are attached to the glass surface coated with BSA-biotin (left). Then, a second particle is attached to the first particle (center), again via biotin-streptavidin binding (right). The biotin on the second particle is covalently linked to the 3′ end of a 33 base pair long ssDNA strand bound to the particle via a thiol group at the 5′ end. Inset: principle of transmission darkfield microscopy. (**b**) Single silver particles appear blue (left) and particle pairs blue-green (right). The orange dot in the bottom comes from an aggregate of more than two particles. (**c**) Single gold particles appear green (left), gold particle pairs, orange (right). Inset: representative transmission electron microscopy image of a particle pair to show that each colored dot comes from light scatted from two closely lying particles, which cannot be separated optically. (**d**) Representative scattering spectra of single particles and particle pairs for silver (top) and gold (bottom). Silver particles show a larger spectral shift (102 nm) than gold particles (23 nm), stronger light scattering and a smaller plasmon line width. Gold, however, is chemically more stable and is more easily conjugated to biomolecules via –SH, –NH2 or –CN functional groups.

should increase the electrostatic repulsion between the charged gold particles[26]. Consistent with this model, a blue-shift in the spectrum of individual nanoparticle pairs occurred when we decreased the salt concentration of our buffer (normally 0.1 M NaCl) to 0.005 M NaCl (Fig. 2a). When we restored the ionic concentration to the original

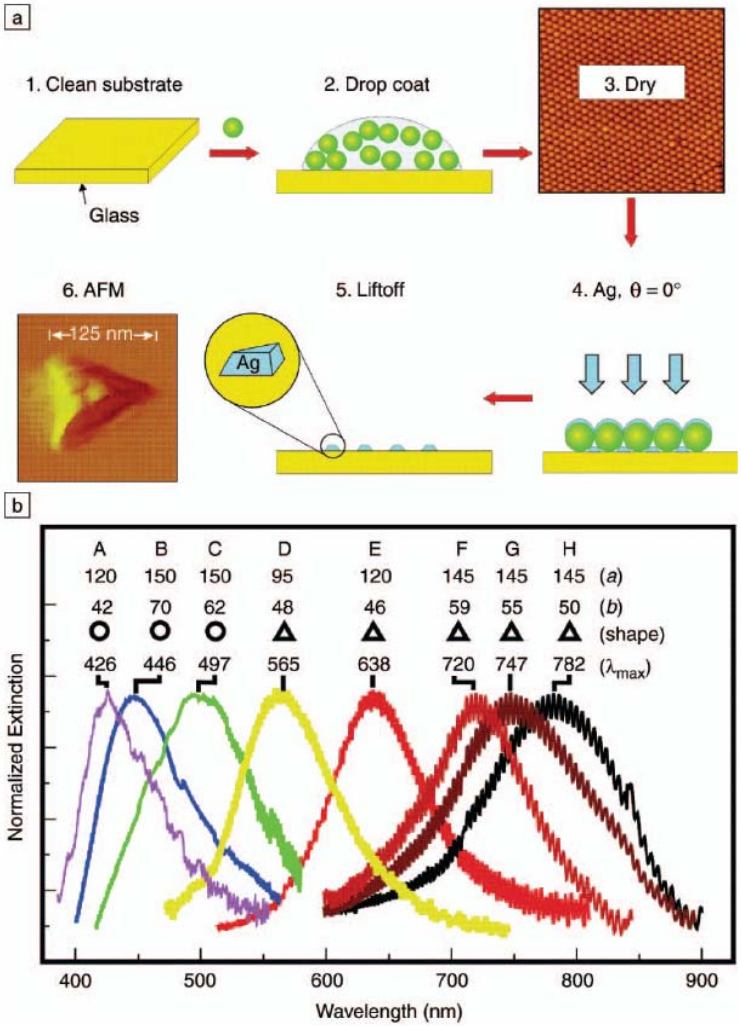

Figure 1. (a) Schematic representation of the nanosphere lithography (NSL) fabrication process. The AFM image in step 3 is 5 μm × 5 μm. (b) Size- and shape-tunable localized surface plasmon resonance spectra of various Ag nanoparticles (labeled A–H) fabricated by NSL. The wavelength of maximum extinction, λ_{max}, is changed by varying the in-plane width a *and out-of-plane height* b *of the nanoparticles.*

The simplest theoretical approach available for modeling the optical properties of nanoparticles is classical electrodynamics (i.e., solving Maxwell's equations with the metal dielectric constant taken from bulk measurements). For spherical particles, this leads to the following (Mie theory) expression for the extinction coefficient $E(\lambda)$ in the long-wavelength limit:[23]

$$E(\lambda) = \frac{24\pi N_A a^3 \varepsilon_m^{3/2}}{\lambda \ln(10)} \times \left[\frac{\varepsilon_i}{(\varepsilon_r + 2\varepsilon_m)^2 + \varepsilon_i^2} \right]. \quad (1)$$

Here, N_A is the areal density of the nanoparticles, a is the radius of the metallic nanosphere, ε_m is the dielectric constant of the medium surrounding the nanosphere (assumed to be a positive, real number), λ is the wavelength, and ε_r and ε_i are the real and imaginary parts of the metal dielectric function. This formula predicts a resonant peak when $\varepsilon_r = -2\varepsilon_m$, which for silver and gold occurs in the visible portion of the spectrum. In addition, any change in the dielectric constant of the medium (e.g., when molecules adsorb on the particle) leads to a change in the resonance wavelength.

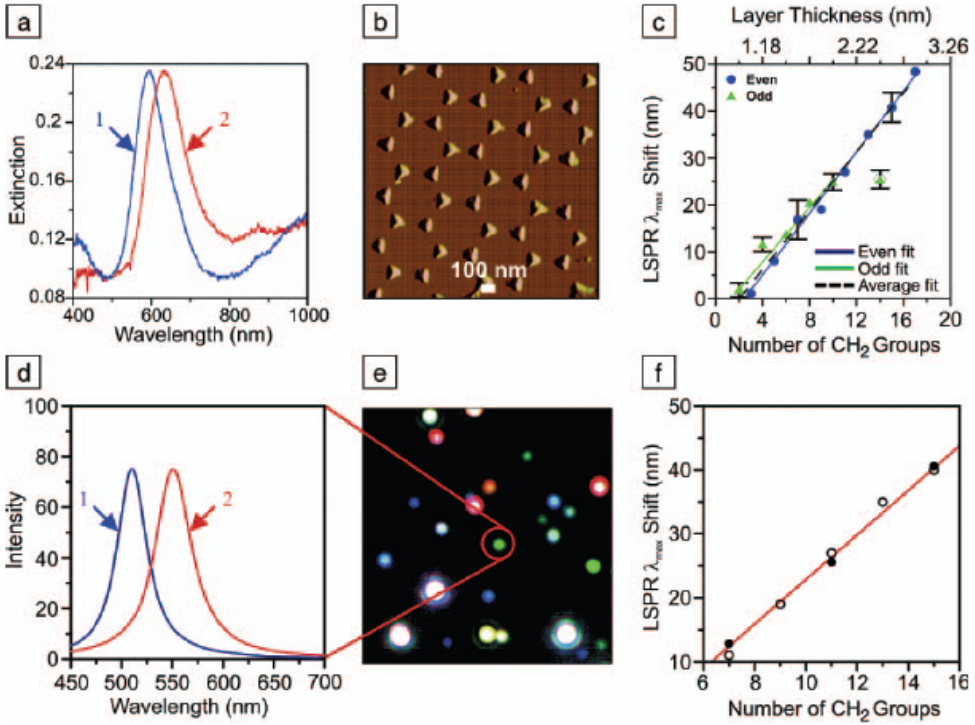

Figure 3. (top row) Localized surface plasmon resonance (LSPR) spectroscopy of a Ag nanoparticle array fabricated by nanosphere lithography in a N_2 environment: (a) Extinction spectrum of the array (curve 1) before chemical modification, wavelength of extinction maximum λ_{max} = 594.8 nm, and (curve 2) after modification with 1 mM hexadecanethiol, λ_{max} = 634.8 nm. (b) Tapping-mode atomic force microscopy (AFM) image of the array in (a); nanosphere diameter D = 390 nm, deposited mass thickness d_m = 50 nm; Ag on mica substrate; scan area, 3.0 μm^2. After solvent annealing, nanoparticle in-plane width is 100 nm and out-of-plane height is 51 nm. (c) Alkanethiol chain length dependence on the LSPR spectral peak shifts for the array. Even and odd carbon chain lengths are depicted with different symbols to emphasize the difference in the terminal bond orientation with respect to the substrate, which leads to different observed trends for the two cases. (bottom row) LSPR spectroscopy of single Ag nanoparticles produced by chemical synthesis: (d) scattering spectrum of a single Ag nanoparticle (curve 1) before chemical modification, λ_{max} = 510.2 nm, and (curve 2) after modification with 1 mM hexadecanethiol, λ_{max} = 550.9 nm. The circled nanoparticle in (e) produced the signal for these curves. (e) Dark-field resonant Rayleigh scattering image of a random array of chemically synthesized Ag nanoparticles (image dimensions, 130 $\mu m \times 130 \mu m$). (f) Alkanethiol chain length dependence on the LSPR spectral peak shifts for a single Ag nanoparticle. The open circles represent an overlay of the array data from (c). The solid circles are single nanoparticle measurements.

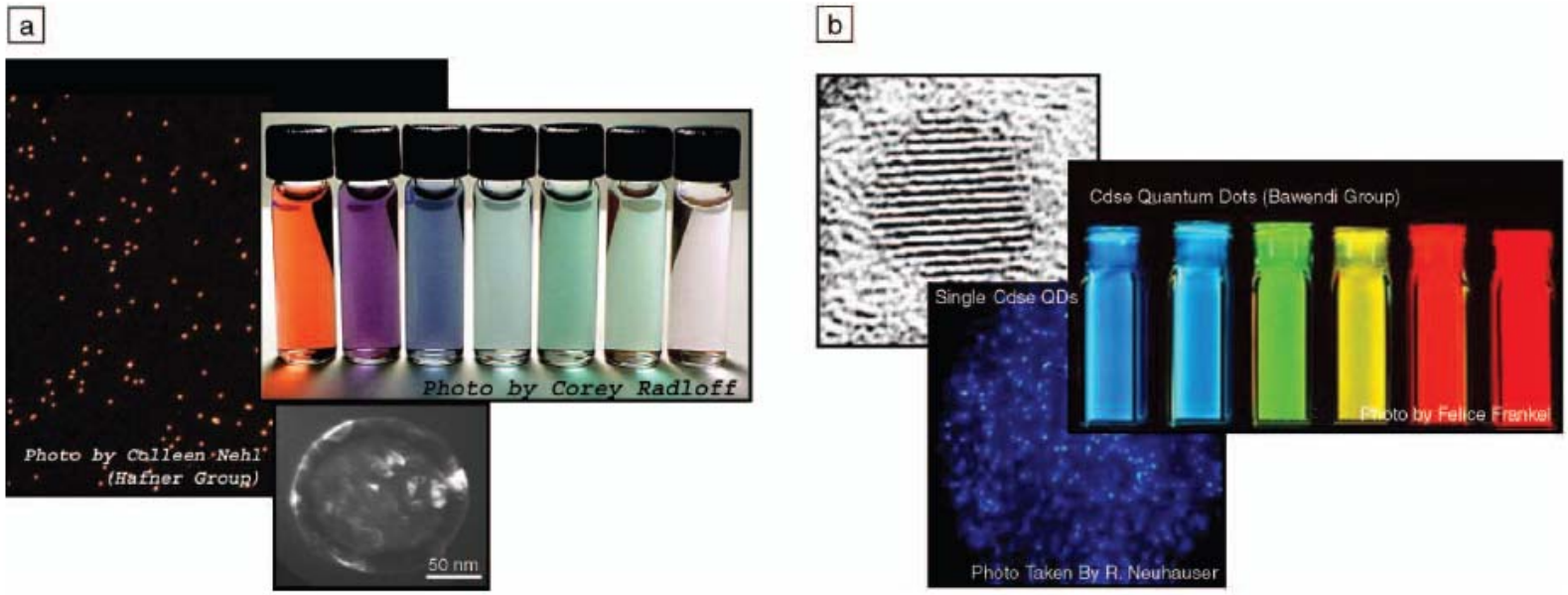

Figure 3. (a) Nanoshells are tunable plasmonic nanoparticles. Micrographs show a field of many nanoshells (large micrograph) and one nanoshell (small micrograph). Vials show nanoshells in solution. (b) Semiconductor quantum dots are tunable excitonic nanoparticles (courtesy of the Bawendi group). A field of quantum dots is displayed in the bottom image; an individual quantum dot is shown in the upper-left micrograph. Vials of quantum dots are also shown. Comparing single nanoshells to single quantum dots, nanoshells typically have a 10^6 larger absorption cross section, nominally five times the physical cross section of the nanoparticle.